

Universidade de São Paulo  
Instituto de Física

Estudo de aceleração de partículas por reconexão  
magnética em jatos relativísticos

Tania Elizabeth Medina Torrejón

Orientadora:

Prof.<sup>a</sup> Dr.<sup>a</sup> Elisabete Maria de Gouveia Dal Pino

Tese de doutorado apresentada ao Instituto de Física da  
Universidade de São Paulo, como requisito parcial para  
a obtenção do título de Doutora em Ciências.

Banca Examinadora:

Prof.<sup>a</sup> Dr.<sup>a</sup> Elisabete Maria de Gouveia Dal Pino - Orientadora (IAG-USP)

Prof. Dr. Edivaldo Moura Santos (IFUSP)

Prof. Dr. Reinaldo Santos de Lima (IAG-USP)

Prof. Dr. Alexandre Lazarian (University of Wisconsin)

Prof. Dr. Luca Comisso (Columbia University)

São Paulo

2021

**FICHA CATALOGRÁFICA**  
**Preparada pelo Serviço de Biblioteca e Informação**  
**do Instituto de Física da Universidade de São Paulo**

Medina Torrejón, Tania Elizabeth

Estudo de aceleração de partículas por reconexão magnética em jatos relativísticos. São Paulo, 2021.

Tese (Doutorado) – Universidade de São Paulo. Instituto de Física.

Orientador: Profa. Dra. Elisabete Maria de Gouveia Dal Pino

Área de Concentração: Física.

Unitermos: 1. Magnetohidrodinâmica; 2. Métodos numéricos; 3. Aceleração de partículas; 4. Jatos (Astronomia).

USP/IF/SBI-009/2021

University of São Paulo  
Physics Institute

Study of particle acceleration by magnetic  
reconnection in relativistic jets

Tania Elizabeth Medina Torrejón

Supervisor:

Prof. Dr. Elisabete Maria de Gouveia Dal Pino

Thesis submitted to the Physics Institute of the University of São Paulo in partial fulfillment of the requirements for the degree of Doctor of Science.

Examining Committee:

Prof. Dr. Elisabete Maria de Gouveia Dal Pino - Supervisor (IAG-USP)

Prof. Dr. Edivaldo Moura Santos (IF-USP)

Prof. Dr. Reinaldo Santos de Lima (IAG-USP)

Prof. Dr. Alexandre Lazarian (University of Wisconsin)

Prof. Dr. Luca Comisso (Columbia University)

São Paulo

2021

To my parents Alfredo & Elizabeth.

*Lift up your eyes and look to the heavens: Who created all these? He who brings out the starry host one by one and calls forth each of them by name. Because of His great power and mighty strength, not one of them is missing.*

**Isaiah 40:26**

# Acknowledgments

First of all, I want to thank my parents, Alfredo & Elizabeth, for their love and constant unconditional support that they have always given me, respecting my decisions and supporting me in my dreams.

To my advisor, Profa. Dra. Elisabete M. de Gouveia Dal Pino, who was always willing to advise me with dedication, patience, strength, optimism and care. I am very grateful to her for all her support.

To the Physics institute for giving me the opportunity to do the PhD.

To the department of Astronomy from IAG, for giving me the opportunity to use their facilities as the office and the cluster for the development of this research work and the simulations.

To my colleagues from office 310 of bloco F from the department of Astronomy, William Clavijo, Pankaj Kushwaha, Lucas Barreto, Svetlana Kocheleva and Luis Kadowaki for their friendship, friendly coexistence, patience and constant discussions about science.

To Luis Kadowaki for sharing his algorithms, used to develop part of the research for this thesis and also thanks to the academic advice, the constant discussions about our research, for the patience in explaining to me about science.

To the whole group GAPAE from IAG, of which I was a part during the development of this PhD, for the conversations and debates of a high level of knowledge, their incentive and friendship.

Thanks to Yosuke Mizuno for sharing his numerical code, which was used in part of the numerical simulations of this thesis.

Thanks to Grzegorz Kowal also for sharing his numerical code, used in part of the research for this thesis and to the discussions about this work.

Thanks to Chandra Singh for the collaboration to develop this work.

To my brothers and sisters from the CONVICTVS group, for always being willing to help me spiritually in the middle of hard academic life.

To FAPESP and CAPES for the financial support which made possible the development of this work.

This study was financed in part by the Coordenação de Aperfeiçoamento de Pessoal de Nível Superior - Brasil (CAPES) - Finance Code 001 and by the Fundação de Amparo à Pesquisa do Estado de São Paulo (FAPESP) (grant 2013/10559-5).

# Abstract

The ubiquitous relativistic jet phenomena associated with black holes play a major role in high and very-high-energy (VHE) astrophysics. In particular, observations indicate that blazars (active galactic nuclei with highly beamed relativistic jets pointing to the line of sight) show highly variable VHE emission, implying extremely compact emission regions. The real mechanism able to explain the particle acceleration process responsible for this emission is still debated, but magnetic reconnection has been lately discussed as a strong potential candidate. In this thesis, by means of three-dimensional special relativistic magnetohydrodynamical (3D-SRMHD) numerical simulations, we investigate the acceleration of test particles injected in a magnetized relativistic jet subject to current-driven kink instability (CDKI), which drives turbulence and fast magnetic reconnection. We find that once the turbulence is fully developed in the jet, achieving a nearly stationary state, the amplitude of the excited wiggles along the jet spine also attains a maximum growth, causing the disruption of the magnetic field lines and the formation of several sites of fast reconnection. This occurs after the CDKI achieves a plateau in its non-linear growth. We performed a systematic search of magnetic reconnection sites in the evolved jet and obtained average magnetic reconnection rates of  $\sim 0.05$  (in units of the Alfvén speed) which are comparable to the predictions of the theory of turbulence-induced fast reconnection. Hundreds to thousands of protons injected in the nearly stationary snapshots of the jet, experience an exponential acceleration up to maximum energy. For a background magnetic field of  $B \sim 0.1$  G, this saturation energy is  $\sim 10^{16}$  eV, while for  $B \sim 10$  G it is  $\sim 10^{18}$  eV. The Larmor radius of the particles attaining the saturation energy corresponds to the size of the acceleration region, being of the order of the diameter of the perturbed jet. During this exponential acceleration, the velocity component of the particles that is predominantly accelerated is the parallel one to the local magnetic field. This regime of particle acceleration is very similar in all these evolved snapshots and lasts for several hundred hours until the saturation energy. The simulations reveal a clear association of the accelerated particles with the regions of fast reconnection, indicating its dominant role in the acceleration process. Beyond those saturation values, the particles suffer further acceleration to energies up to 100 times larger, but at a slower rate due to drift in the varying magnetic field. In the early stages of the development of the non-

linear growth of CDKI in the jet, when there are still no sites of fast reconnection, injected particles are also efficiently accelerated, but by magnetic curvature drift in the wiggling jet spine. However, in order to particles to be accelerated by this process, they have to be injected with an initial energy much larger than that required for particles to accelerate in reconnection sites. Finally, we have also obtained from the simulations an acceleration time due to reconnection with a weak dependence on the particles energy  $E$ ,  $t_A \propto E^{0.1}$ . The energy spectrum of the accelerated particles develops a high energy tail with a power-law index  $p \sim -1.2$  at the beginning of the acceleration, in agreement with earlier works. Our results provide an appropriate multi-dimensional framework for exploring this process in real systems and explain their complex emission patterns, especially in the very high energy bands and the associated neutrino emission recently detected in some blazars.

Keywords: Method: numerical; Magnetohydrodynamic; Particle acceleration; High energy astrophysics; Cosmic rays; Jets (Astronomy).

# Resumo

Os fenômeno onipresente de jatos relativísticos associados a buracos negros desempenha um papel importante na astrofísica de altas e muito altas energias (em inglês, VHE). Em particular, as observações indicam que os blazares (núcleos galácticos ativos com jatos relativísticos de feixe colimado apontando para a linha de visada) mostram emissão VHE altamente variável, implicando em regiões de emissão extremamente compactas. Nesta tese, realizando simulações numéricas tridimensionais relativísticas magnetohidrodinâmicas com relatividade especial (3D-SRMHD), investigamos a aceleração de partículas teste injetadas em um jato magnetizado relativístico sujeito à instabilidade de torção desencadeada por correntes (em inglês, current driven kink instability, CDKI), a qual excita turbulência e reconexão magnética rápida. Verificamos que uma vez que a turbulência está totalmente desenvolvida no jato, atingindo um estado quase estacionário, a amplitude das torções excitadas ao longo da coluna do jato também atinge um crescimento máximo, causando o rompimento das linhas do campo magnético e a formação de vários locais de reconexão rápida. Isso ocorre depois que a CDKI atinge um platô em seu crescimento não linear. Realizamos uma identificação sistemática dos sítios de reconexão magnética no jato e obtivemos taxas médias de reconexão magnética de  $\sim 0.05$  (em unidades da velocidade de Alfvén) que são comparáveis às previsões da teoria da reconexão rápida induzida por turbulência. Centenas a milhares de prótons, injetados em passos temporais no qual o jato está aproximadamente estacionário, experimentam uma aceleração exponencial até uma energia máxima. Para um campo magnético no jato de  $B \sim 0.1$  G, esta energia de saturação é  $\sim 10^{16}$  eV, enquanto para  $B \sim 10$  G é  $\sim 10^{18}$  eV. O raio de Larmor das partículas que atingem a energia de saturação corresponde ao tamanho da região de aceleração, sendo da ordem do diâmetro do jato perturbado. Durante essa aceleração exponencial, a componente de velocidade das partículas que é predominantemente acelerada é a paralela ao campo magnético local. Este regime de aceleração de partículas é muito semelhante em todos os intervalos mais evoluídos do jato e dura por várias centenas de horas até a energia de saturação. As simulações revelam uma clara associação das partículas aceleradas com as regiões de reconexão rápida, indicando seu papel dominante no processo de aceleração. Além desses valores de saturação, as partículas sofrem aceleração adicional para energias até 100 vezes maiores, mas a uma taxa mais lenta, devido a *drift* no campo magnético

variável. Nos estágios iniciais do desenvolvimento do crescimento não linear da CDKI no jato, quando ainda não há locais de reconexão magnética rápida, as partículas injetadas também são eficientemente aceleradas, mas por *drift* devido à curvatura do campo magnético na espinha restorcida do jato. No entanto, para que as partículas sejam aceleradas por esse processo, elas precisam ser injetadas com uma energia inicial muito maior do que a necessária para elas acelerarem nos locais de reconexão magnética. Finalmente, também obtivemos das simulações um tempo de aceleração devido à reconexão com uma fraca dependência da energia das partículas  $E$ ,  $t_A \propto E^{0.1}$ . O espectro de energia das partículas aceleradas desenvolve uma cauda de alta energia com índice de lei de potência  $p \sim -1.2$ , no início da aceleração, o qual é compatível com trabalhos anteriores. Nossos resultados fornecem uma estrutura multidimensional apropriada para explorar aceleração em sistemas reais e explicar padrões de emissão complexos nos mesmos, especialmente nas bandas de energia muito altas e também a emissão de neutrinos associada, recentemente detectados em alguns blazares.

Palavras-chave: Método: numérico; Magnetohidrodinâmica; Aceleração de partículas; Astrofísica de altas energias; Raios cósmicos; Jatos (Astronomia).

# Contents

<b>1</b>	<b>Introduction</b>	<b>1</b>
1.1	Relativistic jets . . . . .	2
1.1.1	Rapid variability in AGN Blazars: a theoretical challenge . . . . .	3
1.2	Magnetic reconnection as a particle acceleration mechanism . . . . .	8
1.3	Fast magnetic reconnection in relativistic jets . . . . .	12
1.3.1	Current-driven kink instability (CDKI) . . . . .	12
1.3.2	Magnetic reconnection driven by CDKI . . . . .	14
1.4	Another particle acceleration mechanism: magnetic curvature drift . . . . .	14
1.5	Goal of this work . . . . .	16
<b>2</b>	<b>Numerical Methodology for Relativistic MHD Jet Simulations and Test Particle Simulations</b>	<b>18</b>
2.1	3D MHD simulations of Relativistic jets . . . . .	19
2.1.1	Initial and Boundary Conditions . . . . .	20
2.2	Algorithm of identification of current sheets . . . . .	24
2.3	Simulation of test particle acceleration by magnetic reconnection in relativistic jets . . . . .	28
<b>3</b>	<b>Results</b>	<b>31</b>
3.1	3D MHD simulation of the relativistic tower jet . . . . .	31
3.1.1	Identification of current sheets in our simulations . . . . .	33
3.1.2	Development of current driven kink instability (CDKI) . . . . .	38
3.1.3	Distribution of the Magnetic Reconnection Velocities . . . . .	40
3.1.4	Magnetization parameter and Current sheet . . . . .	43
3.2	Particle acceleration . . . . .	43
3.2.1	Magnetic Reconnection acceleration . . . . .	47

3.2.2	Particle acceleration in the earlier stages of the CDKI . . . . .	51
3.2.3	Resolution Effects . . . . .	54
3.2.4	Particle acceleration rates . . . . .	58
3.2.5	Particles Spectrum . . . . .	61
3.2.6	Boundary effects . . . . .	62
3.2.7	Magnetic field effects . . . . .	64
3.3	Effects of the dynamical time variations of the background jet on particle acceleration . . . . .	66
<b>4</b>	<b>Conclusions and Prospects for Future Work</b>	<b>69</b>
4.1	Future Prospects . . . . .	74
<b>A</b>	<b>Godunov Method</b>	<b>75</b>
<b>B</b>	<b>Flux-interpolated Constrained Transport Scheme</b>	<b>77</b>

# List of Figures

1.1	Images of the FRI radio galaxy M87 on scales from the outer lobes to near the black hole. (a) Lobe, jet and outer lobes, showing the present outburst and a more ancient one almost perpendicular to the former; (b) galaxy jet and inner lobes; (c) full view of the black hole jet; (d) innermost jet; (e) jet launching region near supermassive black hole; and (f) inner accretion disk and black hole (Blandford et al., 2019). . . . .	4
1.2	Schematic representation of the different classes of AGNs. In this diagram, QSO stands for "quasi-stellar-object", BLRG for "broad-line-region", NLRG for "narrow-line-region", FSRQ for "flat-spectrum-radio-quasar", and BL Lac for "BL Lacertae", the prototype of this sub-class (see text for more details, and Beckmann and Shrader, 2012). . . . .	5
1.3	Schematic representation of a Blazar showing that the jet that emerges from the source (an accretion disk surrounding a BH) points to our line of sight in the Earth. The cartoon also shows a proton (p) that escapes from the source and cascades into pions ( $\pi$ ), electron-positron pairs ( $e^\pm$ ), and neutrinos ( $\nu$ ) while propagating into the ambient medium (IceCube/NASA <a href="https://www.km3net.org/km3net-congratulates-icecube/credit-icecube-nasa-artistic-view-of-a-blazar-emitting-neutrinos-and-gamma-rays/">https://www.km3net.org/km3net-congratulates-icecube/credit-icecube-nasa-artistic-view-of-a-blazar-emitting-neutrinos-and-gamma-rays/</a> ). . . . .	6
1.4	(A) Gamma-ray observations by Fermi-LAT and (B) MAGIC superposed to IceCube observations. Here we can see the blazars TXS 0506+056 and PKS 052+049. Gray and red curves show the 50% and 90% neutrino containment regions, respectively (Aartsen et al., 2018). . . . .	6
1.5	Reconnection sheet showing the magnetic field distribution with two fluxes of opposite polarity $+\mathbf{B}$ and $-\mathbf{B}$ . In the left panel, the line traces the trajectory of a test particle, when it enters the magnetic field discontinuity (current sheet) it bounces back and forth and its energy increases exponentially. The change of colors in the trajectory from red to white corresponds to the growth of the particle energy. The right panel shows the variation of the particle kinetic energy with the x coordinate and with the time (de Gouveia Dal Pino and Lazarian, 2005; Kowal et al., 2011). . . . .	10

1.6	The left panels show particle kinetic energy distributions for 10,000 protons injected in fast magnetic reconnection (top) and 3D turbulence (bottom). The colors red or blue indicate the parallel or perpendicular velocity component to the local magnetic field being accelerated. The diagram in the detail shows the accelerated particles spectrum where we see the development of a power law tail in the high energy. In the right panels, $XY$ cuts through the domain at $z = 0$ of the absolute value of current density $ \mathbf{J} $ overlapped with the magnetic vectors (Kowal et al., 2012). . . . .	11
1.7	This panel shows the distortion of the helical magnetic field caused by the kink instability (Roth, 1997). . . . .	14
1.8	Types of instabilities in the plasma column with strong toroidal magnetic fields for modes $m = 0$ , $m = 1$ and $m = 2$ where $m = 1$ corresponds to the kink instability (Braithwaite, 2006). . . . .	15
1.9	Schematic representation of the development of curvature drift acceleration (see text for more details) (extracted from Alves et al., 2018). . . . .	16
2.1	Radial profiles of the initial parameters for the simulations j240 and j480: Radial profiles of (a) the toroidal magnetic field $ B_\phi $ (in units of $\sqrt{4\pi\rho_0c^2}$ ), (b) the axial magnetic field $B_z$ (also in units of $\sqrt{4\pi\rho_0c^2}$ ), (c) the toroidal velocity $v_\phi$ (in units of $c$ ), (d) the axial velocity $v_z$ (also in units of $c$ ), (e) the density $\rho$ (in units of $\rho_0$ ) for a decreasing density profile with $\Omega_0 = 2.0$ and (f) the Alfvén speed $v_A/c$ . . . . .	23
2.2	Sketch sample of a 2D subarray centered at the cell with $j_{max}$ identified. The choice of the size is $3 \times 3$ cells. . . . .	25
2.3	The left sketch shows a new coordinate system centered in a local reconnection site. The right sketch shows how the edges have been defined as the cells with $ \mathbf{J}  \sim 1/2 \mathbf{J}_{max} $ (Kadowaki et al., 2018b). . . . .	26
2.4	Sample of profiles rejected and accepted, following the criteria of the most symmetric magnetic and velocity field profiles (Kadowaki et al., 2018b). . .	27

3.1	Time evolution of the tower jet at $t = 25, 30, 40, 44, 46$ and $50 L/c$ (from top left to bottom right). The diagrams depict isosurfaces of the current density intensity at half maximum $ J $ (orange color), the solid black lines correspond to the magnetic field lines, and the green circles correspond to the position of fast magnetic reconnection regions (with velocities larger than or equal to the average reconnection speed) identified with the algorithm described in Section 2.2. At z-y plane, it is shown the density map of the central slice of the jet (at $x = 0$ ). The time $t$ is in units of $L/c$ , the density in units of $\rho_o$ , and the current density is also in code units. . . . .	32
3.2	Diagrams of three magnetic reconnection sites in the jet frame, selected from snapshot $t = 50L/c$ . The diagrams were produced by a line integral convolution (LIC) method combined with the 2D projection of the magnetic field (top diagrams) and current density (bottom diagrams) magnitudes in the $\hat{e}_1$ - $\hat{e}_2$ plane. . . . .	33
3.3	The top diagram shows a zoom-in plot of the magnetic field streamlines (black and magenta lines) around a sample of identified reconnection sites (green and black circles), at $t = 50L/c$ , in the jet frame. The colored arrows represent the axes of the local coordinate system, and the orange isosurface corresponds to the associated current sheet with half of the maximum value of $ J $ at the primary reconnection site (green circle). The bottom diagrams show the corresponding 2D LIC maps (as in Figure 3.2). . . . .	35
3.4	Time-distribution of the Lorentz factor ( $\Gamma$ ) of the diffusion regions with respect to the jet frame, for the model j240. The histogram corresponds to Lorentz factors obtained during the entire evolution of the simulation (with 200 bins in each direction). . . . .	36
3.5	Time evolution in code units of the reconnection velocity in the tower jet for the two resolutions investigated in this work. It includes to the whole sample of reconnection regions (with symmetric and nonsymmetric profiles). The time $t$ is in units of $L/c$ . The shaded light blue and red colors give the entire distribution of reconnection velocities from maximum to minimum values for the two jet models, j240 and j480, respectively. The blue and red lines give the corresponding average reconnection speeds, $\langle V_{rec} \rangle$ , for each model (over all identified sites in each snapshot). . . . .	37
3.6	Volume-averaged energy time evolution within a cylinder of radius $R/L \leq 3.0$ for the simulation. In red: kinetic energy transverse to the z-axis. In blue: total electromagnetic energy. The kinetic energy density is in log scale, while the electromagnetic energy density is in linear scale. . . . .	39

- 3.7 Histograms of the reconnection rate  $V_{rec}$  for the model j240. The left diagrams correspond to time-distributions obtained during the entire evolution of the simulation (with 200 bins in each direction), and the right diagrams correspond to 1D-distributions (red lines) with a log-normal fit (black lines) obtained between the snapshots 50 and 66 $L/c$  (with 140 bins). The top distributions correspond to the whole sample, and the bottom ones correspond to a constrained sample considering only the most symmetric profiles of the velocity and magnetic fields at the edge of the diffusion regions. . . . 41
- 3.8 Two-dimensional cuts in the  $x - z$  plane at  $y = 0$ , in logarithm scale of the current density  $\nabla \times \mathbf{B}$  (left panels), and magnetization parameter  $\sigma = B^2/\gamma^2\rho h$  (right panels) at  $t = 44, 46$  and  $50 L/c$  (from top to bottom). The time  $t$  is in units of  $L/c$ . . . . . 42
- 3.9 Two-dimensional histograms of particle positions for different snapshots of the model j240. From top to bottom,  $t = 25 L/c$  (*ut25o*),  $t = 30 L/c$  (*t30o*),  $t = 44 L/c$  (*t44o*),  $t = 46 L/c$  (*t46o*), and  $t = 50 L/c$  (*t50o*), respectively. Each row, from left to right, shows histograms projected on  $xy$ ,  $xz$ , and  $yz$  plans. To make visualization more clear, the histograms depict only particles accelerating with increment  $\Delta E_p/E_p > 0.4$ , and with energies larger than  $10^2$  MeV ( $\sim 10^{-1}m_p c^2$ ), except for  $t = 25 L/c$ , for which the minimum energy depicted is  $10^4$  MeV. The different colors indicate the (normalized) concentration of particles in each region of the jet (see text for details). . . . . 44

- 3.10 Three-dimensional histogram of accelerated particle positions (square symbols) for the snapshot  $t = 50 L/c$  of jet model  $j240$ , in different viewing angles indicated by the Cartesian axes in the bottom left of each figure. It was integrated over the particles acceleration time between 100 and 5000 hours, which corresponds to the exponential acceleration regime (see Figure 3.11, bottom right panel). Only the positions of particles accelerated with energy increment  $\Delta E_p/E_p > 0.4$  were included, and energy between  $E_p > 10^{-1} m_p c^2$  and the saturation energy  $E_p \sim 10^7 m_p c^2$ . In order to improve visualization, particles that accelerated to a maximum energy less than  $10^3$  MeV were also removed, and to avoid boundary effects, the counts were constrained to the domain between  $[-2.5, 2.5] L$  in the x and y directions, and  $[0.5, 5.5] L$  in the z direction. The circles correspond to the positions of fast magnetic reconnection sites (with velocities larger than or equal to the average reconnection speed) and their color, represent their reconnection velocity in units of the local Alfvén speed. The isosurfaces of the current density intensity at half maximum  $|J|$  (yellow color) are also depicted ( $J_{max}/2 \sim 1.25$ ). . . . . 45
- 3.11 Kinetic energy evolution (normalized by the proton rest mass energy, which is equivalent to  $(\gamma - 1)$ ) for the particles injected in the snapshots  $t = 40, 44, 46$  and  $50 L/c$  of the jet model  $j240$ , from top left to bottom right, respectively. The color bars indicate the number of particles. The small plots in the upper left of each panel show the time evolution of the particles gyro-radius. The horizontal orange line corresponds to the cell size of the simulated background jet, the grey color corresponds to the entire distribution of gyro-radius values, and the blue line gives the average value. 48
- 3.12 Kinetic energy evolution, normalized by the proton rest mass energy, for the particles injected in the snapshots  $t = 40, 44, 46$  and  $50 L/c$  of the jet model  $j240$ , from top left to bottom right, respectively. The colors indicate which particle velocity component is being accelerated (red or blue for parallel or perpendicular component to the local magnetic field, respectively). The small plots in the upper left inset of each panel show the time evolution of the particles gyro-radius. The horizontal orange line corresponds to the cell size of the simulated background jet, the grey color corresponds to the entire distribution of gyro-radius values, and the blue line gives the average value. . . . . 50

3.13	Kinetic energy evolution for particles injected in the snapshot $t = 25 L/c$ of the jet model $j240$ . The top panel corresponds to particles injected with a Maxwellian distribution and $\langle E_p \rangle \sim 10^{-3} m_p c^2$ , as in Figure 3.11. The bottom panel corresponds to particles injected with a monoenergetic distribution with larger energy $E_p \sim 10 m_p c^2$ . The color bar indicates the number of particles. The small plots in the detail depict the evolution of the particles gyro-radius, the same as in Figure 3.11. . . . .	52
3.14	Kinetic energy evolution for particles injected in the snapshot $t = 25 L/c$ of the jet model $j240$ , corresponds to particles injected with a monoenergetic distribution with larger energy $E_p \sim 10 m_p c^2$ , the same as in right panel of Figure 3.13. The colors indicate which particle velocity component is being accelerated (red or blue for parallel or perpendicular component to the local magnetic field, respectively). The small plot in the detail depict the evolution of the particles gyro-radius, the same as in Figure 3.13. . . .	53
3.15	Kinetic energy evolution for particles injected in the snapshot $t = 30 L/c$ of the jet model $j240$ ( $t30o$ ). As in Figure 3.11, particles are injected with $\langle E_p \rangle \sim 10^{-3} m_p c^2$ and a Maxwellian distribution. The color bar in the left panel indicates the number of particles and the small plot in the detail depicts the evolution of the particles gyro-radius. The two colors in the right panel indicate which velocity component of the particles is being accelerated (red or blue for parallel or perpendicular component to the local magnetic field, respectively). . . . .	54
3.16	Particle kinetic energy evolution, normalized by the rest mass energy, for 1,000 protons injected in $t = 50 L/c$ snapshot of the higher resolution jet model ( $t480$ , see Table 2.1). The initial conditions for the test particles are the same as in the lower resolution test shown in Figure 3.11 for the same time step (bottom panel), except that there 10,000 protons were used. The color bar indicates the number of particles. The small plot on upper left shows the evolution of the particles gyro-radius. . . . .	56
3.17	Particle kinetic energy evolution, normalized by the rest mass energy, for 1,000 protons injected in $t = 25$ (upper) $t = 30 L/c$ (bottom) snapshots of the higher resolution jet model ( $t480$ , see Table 2.1), $480t25o$ and $480t30o$ , respectively. The initial conditions for the test particles are the same as in the lower resolution test shown in Figure 3.13 (top panel) and Figure 3.15 for the same time step (bottom panel). The color bar indicates the number of particles. The small plot on upper left shows the evolution of the particles gyro-radius. . . . .	57

3.18	Acceleration time (top panel), power law index of the acceleration time, $\alpha$ index (middle), and kinetic energy growth rate (bottom) as functions of the particle kinetic energy normalized by the proton rest mass energy for the different test particle models of Table 3.2. The error bars are obtained calculating the standard deviation. . . . .	59
3.19	Acceleration time (left) and power law index of the acceleration time (right) of the test particles in $t = 30 L/c$ for the jet models of lower ( $240^3$ ) and higher resolution ( $480^3$ ), t30o and 480t30o, respectively. . . . .	61
3.20	Particles energy spectrum evolution as a function of the normalized kinetic energy ( $m_p c^2$ ) in the jet snapshots, from top left to bottom right: $t = 25$ (particle model <i>ut25o</i> ); 30 (particle model <i>t30o</i> ), 46 ( <i>t46o</i> ), and $50 L/c$ (test particle model <i>t50o</i> ). The red line in all panels but the top left, corresponds to the initial Maxwellian distribution of the particles. In the top left panel particles are injected with a monoenergetic spectrum. The timesteps (in hours) of the acceleration are depicted in the detail of each panel. . . . .	63
3.21	Particle energy spectrum as a function of the normalized kinetic energy at two different early time steps of the acceleration (in hours) for the jet snapshot $t = 50 L/c$ . The dotted gray line is the initial Maxwellian distribution. The high energy tail of each distribution is fitted by a power-law. . . . .	64
3.22	Particle kinetic energy evolution, normalized by the rest mass energy, for particles injected in $t = 50 L/c$ snapshot of the jet model ( <i>j240</i> , see Table 3.2). This test is similar to that of the bottom right diagram of Figure 3.11, except that here particles were periodically re-injected through all the boundaries of the jet system (see model <i>t50p</i> in Table 3.2). The color bar indicates the number of particles. The small plot on the upper left shows the evolution of the particles gyro-radius. . . . .	65
3.23	Kinetic energy evolution for particles injected at snapshot $t = 50 L/c$ ( <i>9t50o</i> ) of the jet model <i>j240</i> with an initial background magnetic field at jet axis $B_0 = 9.4$ G and a background density $\rho_0 = 10^4 \text{ cm}^{-3}$ (see Table 3.2). The initial conditions are the same as in the test particle model ( <i>t50o</i> ) shown in the bottom right panel of Figure 3.11, except that there $B_0 = 0.094$ G and $\rho_0 = 1 \text{ cm}^{-3}$ , leaving unaltered the Alfvén velocity in both tests (see text for details). The color bar indicates the number of particles and the small plot in the detail shows the evolution of the particles gyro-radius. . . . .	65

A.1	Schematic representation of a 3D cell, where the volume-averaged conserved variables $\tilde{\mathbf{U}}$ is in the center of the box, and $i, j$ and $k$ represent the three directions of the box. The magnetic field $\mathbf{B}$ is calculated at the edge of the cells. . . . .	76
B.1	Sketch sample of a 2D grid centered at the cell position $(i,j)$ . The electric field $\Omega$ is located at the cell corners with the purpose to calculate $\nabla \cdot B$ at the center of the cell. . . . .	78

# List of Tables

2.1	Parameters for the MHD simulations. . . . .	24
3.1	Reconnection velocity values in units of the local Alfvén speed in j240. . .	38
3.2	Parameters for the test particle simulations. . . . .	46
3.3	Reconnection velocity values in units of the local Alfvén speed in j480. . .	56

# Chapter 1

## Introduction

Astrophysical jets are supersonic collimated flows that transport mass, momentum, energy and magnetic flux, which are present in different classes of astrophysical sources, from young stellar objects (YSOs) with thermal non relativistic jets, to relativistic jets propagating with velocities close to the light speed in X-ray binary systems that host a stellar-mass black hole (also denominated BH XRBs or microquasars), active galaxies that host supermassive black holes (BH)<sup>1</sup> in their nucleus (or AGNs), and gamma-ray-bursts (GRBs) whose engine is still not known, but it is ultimately produced by the merger of black holes or neutron stars (Spruit et al., 2001; Giannios, 2008; McKinney and Uzdensky, 2012; Giannios and Uzdensky, 2019). Since most of these compact objects are not visible, the jet arising from them propagating over very large distances can provide information about their progenitors. For instance AGN jets can travel distances  $\gtrsim 10^6$  pc, which is up to  $10^9$  times the Schwarzschild radius,  $R_S = 2GM/c^2$ , of their central supermassive black hole. Therefore, the jets can provide important information about the physical processes that take place in their internal regions (Das, 1999; de Gouveia Dal Pino, 2005; Matthews et al., 2020). Currently, there are major puzzles related to the origin of the very high energy (VHE) variable emission observed, especially in high luminous AGN jets pointing to the line of sight (named blazars). These observations put severe constraints on existing models of acceleration of the particles that are responsible for this VHE emission in these sources (see e.g., Aharonian et al., 2007; Giannios et al., 2009; de Gouveia Dal Pino and Kowal, 2015; de Gouveia Dal Pino et al., 2018; Christie et al., 2019; Alves et al., 2018; Matthews et al., 2020)

In this Ph.D. work, we investigate the acceleration of test particles injected in the magnetically dominated regions of a three-dimensional relativistic magnetohydrodynamical jet, and show that magnetic reconnection is the dominant particle acceleration process, that provides a potential solution for this puzzle. In the next Sections, we present a brief overview of the physical and radiative properties of relativistic jets and, in particular, of

---

<sup>1</sup>A supermassive BH has a mass of the order  $10^6-10^9 M_\odot$ , where  $M_\odot$  is the solar mass.

those connected with AGN blazars. Then, we discuss the particle acceleration processes that may be relevant in such systems and, especially, the mechanism of magnetic reconnection and how it can be driven in relativistic magnetized jets. Finally, we draw the plan and the aims of this thesis, describing the contents of the next chapters.

## 1.1 Relativistic jets

Relativistic, collimated jets are ubiquitous in astrophysical sources, as stressed. Their propagation speeds span from mildly ( $v \sim 0.26c$ )- or highly-relativistic ( $v \sim 0.92c$ ) in microquasars and AGNs, to ultra-relativistic ( $v \sim 0.9999c$ ) ones in GRBs. An important property common to all these classes of objects is the required presence of magnetic fields to allow their formation. There are different models to explain the formation of a jet and the most accepted are those that involve the combination of magnetic field and rotation (e.g., Blandford and Znajek, 1977; Blandford and Payne, 1982). In a steady jet, the relativistic energy and angular momentum outflows are carried predominantly by the electromagnetic field (or Poynting-flux). According to Blandford and Znajek (1977), the relativistic jet is driven by the rotational energy of the BH, which twists the magnetic field lines that in turn, transport energy to the surroundings, pulling the flow outward as a Poynting-flux dominated<sup>2</sup> jet. Another mechanism of jet formation, proposed by Blandford and Payne (1982) claims that the accretion disk, rotating around the BH, can transfer angular momentum and energy to the magnetic field lines embedded in it and these will raise from the disk accelerating the surrounding ionized gas (plasma) in a perpendicular to the disk and anchored in the disk, they rotate with the disk and ionized matter by a magneto-centrifugal process along the field lines which are wound up, forming a steady jet with a helical magnetic field structure.

Observed polarized non-thermal<sup>3</sup> emission in all wavelengths also evidences that these jets are highly magnetized, especially near the launching region, at the source (e.g., Laurent et al., 2011; Doeleman et al., 2012; Martí-Vidal et al., 2015). For instance, it has been reported evidences of a helical magnetic field feature in the radio galaxy M87 jet (Figure 1.1) (Harris et al., 2003; Blandford et al., 2019). General relativistic magnetohydrodynamic (GRMHD) simulations with accretion disks around the spinning black hole of these sources are compatible with the observations and the proposed mechanisms for jet formation (Blandford and Znajek, 1977; Blandford and Payne, 1982). They reveal the

---

<sup>2</sup>The Poynting flux in plasma is given by  $\mathbf{S} = (c/4\pi)\mathbf{E} \times \mathbf{B}$ . A system is Poynting flux dominated if  $\mathbf{S}$  is very strong, or in other words, if the plasma thermal pressure and inertial forces are smaller than the magnetic Lorentz force.

<sup>3</sup>The non-thermal emission happens when the emitted radiation does not depend on the temperature of the emitter, but on non-thermal processes, for instance, Synchrotron radiation and Compton scattering (Rybicki and Lightman, 1991).

formation of a Poynting flux dominated jet spine with a large Lorentz factor<sup>4</sup>, surrounded by a mildly relativistic (matter-dominated) sheath, and a sub-relativistic wind (e.g., McKinney, 2006; Hardee et al., 2007; Abramowicz and Fragile, 2013; Yuan and Narayan, 2014). This spine-sheath structure has indeed been inferred from very-long-baseline Interferometry (VLBI) observations from nearby radiogalaxies like M87 (Kovalev et al., 2007), 3C84 (Nagai et al., 2014), and Cyg A (Boccardi et al., 2015), as well as in blazars like Mrk501 (Giroletti et al., 2004) and 3C273 (Lobanov and Zensus, 2001)(see Section 1.1.1).

Another important constraint from the observations is the fact that at distances large enough from the sources these jets should become kinetically dominated and as such, they should convert most of the magnetic energy into kinetic. A parameter that defines the degree of magnetization of a relativistic jet is the  $\sigma$  parameter, defined as the ratio of the magnetic plus electric energy flux to the mass energy flux. For values of  $\sigma \geq 1$ , the jet is considered magnetically dominated (see Section 3.1.4, in Chapter 3). A mechanism that could favor the conversion from magnetic to kinetically dominated in jets is magnetic reconnection (e.g., Giannios, 2010; de Gouveia Dal Pino and Kowal, 2015; de Gouveia Dal Pino et al., 2018; Werner et al., 2018, and references there in). Lately, this process has been largely investigated in the framework of compact sources like pulsar nebulae (e.g., Lyubarsky and Kirk, 2001; Clausen-Brown and Lyutikov, 2012; Cerutti et al., 2014; Sironi and Spitkovsky, 2014), gamma-ray bursts (GRBs) (e.g., Drenkhahn and Spruit, 2002; Giannios and Spruit, 2007; Zhang and Yan, 2011), as well as jets and accretion flows around black holes (e.g., de Gouveia Dal Pino and Lazarian, 2005; Giannios et al., 2009; de Gouveia Dal Pino et al., 2010b,a; Giannios, 2010; McKinney and Uzdensky, 2012; Kadowaki et al., 2015; Singh et al., 2015; Khiali et al., 2015; Singh et al., 2016; Sironi et al., 2015; de Gouveia Dal Pino et al., 2018; Kadowaki et al., 2018b,a; Rodriguez-Ramirez et al., 2019; Christie et al., 2019; Fowler et al., 2019; Giannios and Uzdensky, 2019; Nishikawa et al., 2020; Nathanail et al., 2020; Davelaar et al., 2020).

### 1.1.1 Rapid variability in AGN Blazars: a theoretical challenge

The nucleus of a galaxy is called AGN when it contains a supermassive BH which accretes gas through a disk and emits high, non-stellar luminosity covering the whole electromagnetic spectrum (Beckmann and Shrader, 2012; Blandford et al., 2019). These AGNs can form relativistic jets, as described above, and can be classified from their radio-loudness and physical emission, as radio-loud (RL) and radio-quiet (RQ) objects, with and without large-scale emission (see e.g. Wilson and Colbert, 1995). The radiation emitted by AGNs is certainly not isotropic for this reason. They may appear quite different when viewed from different angles (see Figure 1.2). RQ AGN can be divided in two subclasses,

---

<sup>4</sup>The Lorentz factor  $\gamma = (1 - \beta^2)^{-1/2}$ , where  $\beta = v/c$  is the ratio between the velocity of the source and the speed of light.

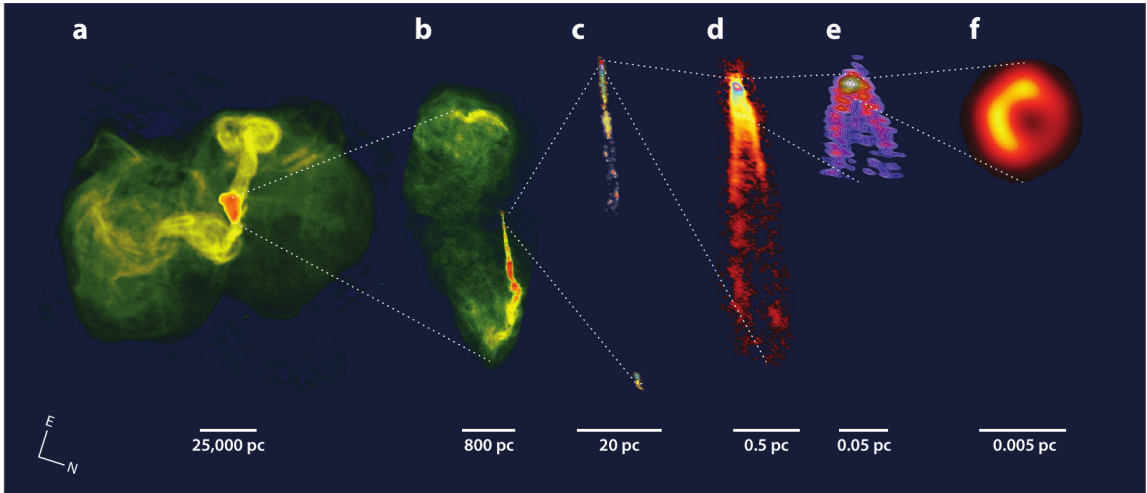


Figure 1.1: Images of the FRI radio galaxy M87 on scales from the outer lobes to near the black hole. (a) Lobe, jet and outer lobes, showing the present outburst and a more ancient one almost perpendicular to the former; (b) galaxy jet and inner lobes; (c) full view of the black hole jet; (d) innermost jet; (e) jet launching region near supermassive black hole; and (f) inner accretion disk and black hole (Blandford et al., 2019).

Seyfert 1 and 2. Seyfert 1 are viewed close to their pole, while Seyfert 2 close to their equatorial plane. RL AGNs are subdivided into low power (Fanaroff-Riley class I, FRI) radio galaxies, and BL Lacertae (BL Lac) objects. BL Lacs, in turn, are a sub-class of the blazars. These include all AGNs with the jet pointing close to the line-of-sight ( $\leq 20 - 30$ ) (Figures 1.2 and 1.3), characterized by highly luminous and rapidly variable continuum emission at all observed frequencies from radio to gamma-rays (e.g., Urry and Padovani, 1995). They include both the BL Lacs and flat-spectrum radio quasars (FSRQs). While both blazar classes share the properties of a nonthermal continuum, by definition FSRQs have strong and broad (rest-frame equivalent width  $EW_r \gtrsim 5A$ ) optical emission lines, while in BL Lacs the optical lines are weak ( $EW_r \lesssim 5A$ ) or absent. FSRQs have higher bolometric luminosities than BL Lacs and can exhibit signs of thermal activity possibly related to an accretion disk in their optical and UV spectra, in contrast to BL Lacs, which have smooth continua. The broad emission lines are intrinsically brighter in FSRQs than in BL Lacs, although with distributions spanning a similar range in luminosity over four decades (e.g., Sambruna, 1997). In the high energies, BL Lacs are characterized by a spectral energy distribution in which two peaks occur (e.g., one at hard X-rays and the other at high energy (HE) or very high energy (VHE)  $\gamma$ -rays). In the classification of the AGNs viewed at larger angles, if the large-scale lobes dominate the radio emission, then the object is a classical FRI radio galaxy. While FRI are low-luminosity radio galaxies, FR II are high-luminosity radio galaxies with dominating core emission (Antonucci, 1993; Urry and Padovani, 1995; Beckmann and Shrader, 2012; Blandford et al., 2019).

Among all classes of relativistic jets, reconnection can be particularly important in

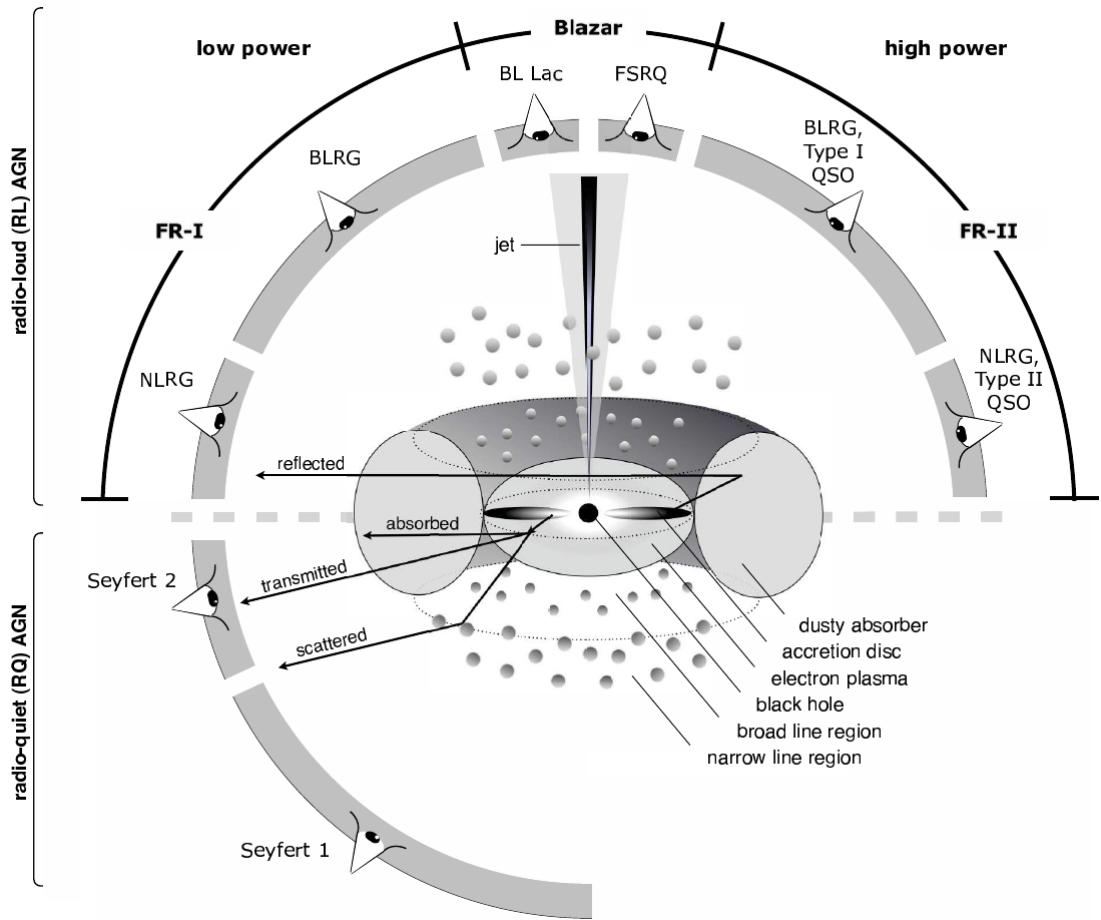


Figure 1.2: Schematic representation of the different classes of AGNs. In this diagram, QSO stands for "quasi-stellar-object", BLRG for "broad-line-region", NLRG for "narrow-line-region", FSRQ for "flat-spectrum-radio-quasar", and BL Lac for "BL Lacertae", the prototype of this sub-class (see text for more details, and Beckmann and Shrader, 2012).

blazars (Figure 1.3). Having a jet pointing close to the line-of-sight is a geometry particularly favorable since relativistic effects, like the Doppler boosting<sup>5</sup> with an apparent enhancement of the observed emission, are maximized. As stressed, blazars are characterized by rapid variability, non-thermal emission in all wavelengths, which is generally attributed to relativistic particles (protons and electrons) accelerated stochastically in recollimation shocks along the jet and in their head (de Gouveia Dal Pino, 2005; Mizuno et al., 2015; Hovatta and Lindfors, 2019; Matthews et al., 2020, e.g.), resulting in heavily Doppler boosted observed radiation (see e.g. Jorstad et al., 2017).

However, there is increasing evidence that shock acceleration may not be always as efficient, particularly in the magnetically dominated regions of these jets where shocks are

<sup>5</sup>The Doppler boosting (or relativistic beaming) is a relativistic effect which modifies the apparent luminosity ( $L_0$ ) of the emitting matter by  $L = L_0 \delta^n$ , when it is moving close to the speed of light, where  $\delta$  is the Doppler factor  $\delta = \gamma^{-1}(1 - \beta \cos \theta)^{-1}$  and  $\theta$  the jet orientation with respect to the line of sight, and  $n$  depends on the geometry and spectral index and is typically in the range between 2 and 3 (Kellermann et al., 2007).

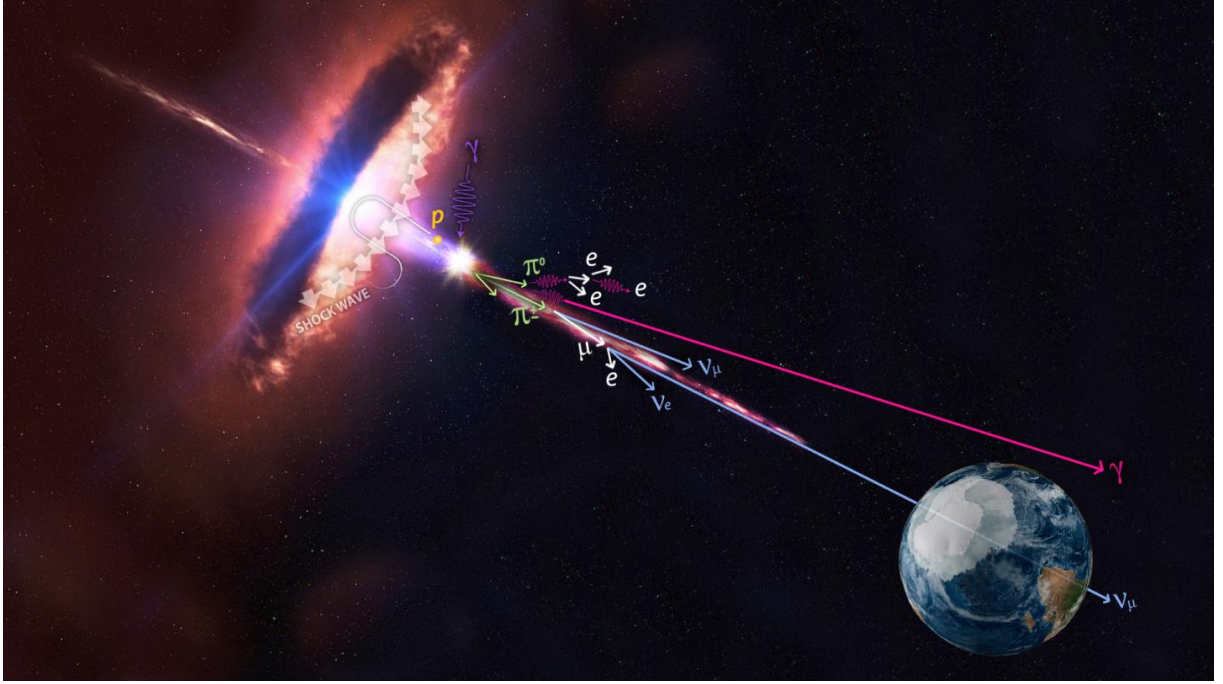


Figure 1.3: Schematic representation of a Blazar showing that the jet that emerges from the source (an accretion disk surrounding a BH) points to our line of sight in the Earth. The cartoon also shows a proton (p) that escapes from the source and cascades into pions ( $\pi$ ), electron-positron pairs ( $e^\pm$ ), and neutrinos ( $\nu$ ) while propagating into the ambient medium (IceCube/NASA <https://www.km3net.org/km3net-congratulates-icecube/credit-icecube-nasa-artistic-view-of-a-blazar-emitting-neutrinos-and-gamma-rays/>).

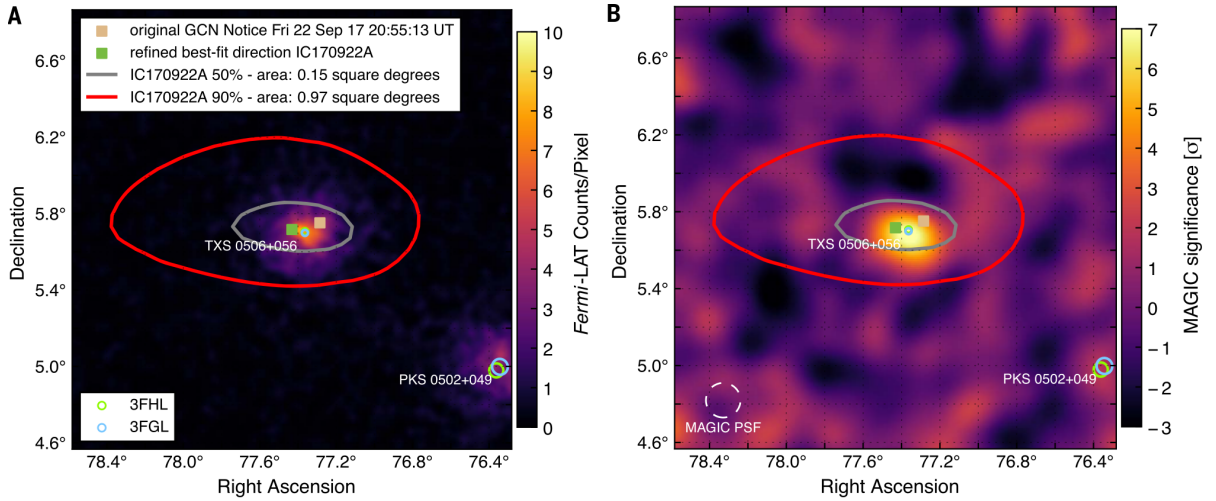


Figure 1.4: (A) Gamma-ray observations by Fermi-LAT and (B) MAGIC superposed to IceCube observations. Here we can see the blazars TXS 0506+056 and PKS 052+049. Gray and red curves show the 50% and 90% neutrino containment regions, respectively (Aartsen et al., 2018).

faint, to explain the very high energy emission (Sironi et al., 2013; de Gouveia Dal Pino and Kowal, 2015; Bell et al., 2018). This may be the case, for instance, of the blazars PKS 2155-304 (Aharonian et al., 2007) and MRK501 (Albert et al., 2007) (see also 3C 279 (Ackermann et al., 2016) and 3C 54.3 (Britto et al., 2016)). They produce very short duration gamma-ray flares, of minutes or less, at the TeV band, which imply extremely compact acceleration/emission regions.

In fact, in 2006, an extremely bright flare of BL Lac PKS 2155-304 was observed at TeV with a timescale flux variability of  $\sim 200$  s (Aharonian et al., 2007). Causality arguments imply that the emission region has an extension  $l \sim c\delta t$ , where  $\delta t$  is the time variability. This is much shorter than the Schwarzschild radius of the supermassive black holes of these blazars ( $M_{BH} \sim 10^9 M_\odot$ )  $r_g/c = GM/c^3 = 1.4M_9$  h, where  $r_g$  is the gravitational (Schwarzschild) radius and  $M_9 = M/10^9 M_\odot$  is the black hole mass. In other words, this emission should be produced in extremely compact zones in the jet. Furthermore, the fact that we observe these TeV photons, implies that the corresponding Lorentz factor of the emission region has to be  $\Gamma \sim 50$ , which is much larger than the typical jet bulk values in these sources ( $\Gamma \simeq 5 - 10$ ). This larger Lorentz factor ensures that gamma-rays will not be re-absorbed within the source, due to electron-positron pair creation (e.g., Begelman et al., 2008).

The only mechanism that seems to be able to drive both, the high variability and compactness of the TeV emission is fast magnetic reconnection involving misaligned current sheets inside the jet. This was first suggested by Giannios et al. (2009) and they called their model "jets-in-a-jet". They invoked the emission of plasma "blobs" by magnetic reconnection inside a Poynting-flux dominated jet, with Lorentz factor of the blob,  $\Gamma_{co} \gg 1$ . They considered a magnetic energy dissipation through magnetic reconnection by current-driven instabilities. Using this model, they explained the emission of TeV gamma-rays by a jet with a bulk Lorentz factor  $\Gamma \sim 10$  (see also, Giannios, 2013; Kushwaha et al., 2017). A similar mechanism has been also invoked to explain the prompt emission in gamma-ray-bursts (e.g. Giannios, 2008; Zhang and Yan, 2011).

Another striking recent discovery has been the simultaneous detection of gamma-rays and high-energy neutrinos, with the energy of  $\sim 290$  TeV, from the blazar TXS 0506 +056 (Aartsen et al., 2018). This has evidenced, for the first time, the presence of high-energy protons interacting with ambient photons creating a flux of high-energy pions and a subsequent decay in gamma-rays and neutrinos (Figure 1.4). Neutrinos travel freely and are not stopped by other particles or deflected by magnetic fields (see Figure 1.3). The observation of astrophysical high energy neutrinos coming from blazars implies the presence of high-energy protons with energies  $\sim 1$  PeV in the jet, something that up to now was not obvious<sup>6</sup>. It has been argued that if these protons are produced in magnetically

---

<sup>6</sup>In fact, the chemical composition of relativistic jets is still a matter of debate. The absence of

dominated regions of the jet near the core, then since shocks there are faint, they have to be probably accelerated by fast magnetic reconnection (e.g., de Gouveia Dal Pino et al., 2018).

In the next section, we will discuss this mechanism.

## 1.2 Magnetic reconnection as a particle acceleration mechanism

Magnetic reconnection is produced from the merging of two magnetic fluxes of opposite polarity (Parker, 1957). For reviews on this subject, we refer to e.g., (Parker, 1957; Zweibel and Yamada, 2009; Lazarian et al., 2012, 2020). Here, we will present only a very brief summary of reconnection driven by turbulence. If the microscopic Ohmic resistivity<sup>7</sup> is non null, the magnetic field lines may annihilate at the contact discontinuity (or current sheet).

Reconnection is *fast* when its rate  $V_R$  is a substantial fraction of the local Alfvén speed,  $V_A$ . The ubiquitous turbulence in astrophysical flows is acknowledged as one of the main driving mechanisms of fast reconnection due to the wandering of the magnetic field lines that allows for many simultaneous events of reconnection and the broadening of the outflow region removing the reconnected flux more efficiently. These two factors result in the reconnection rate to be independent of the generally small microscopic magnetic resistivity (Lazarian and Vishniac, 1999) (see also Eyink et al., 2011; Kowal et al., 2009; Takamoto et al., 2015; Santos-Lima et al., 2010, 2020),

$$V_{rec} = \min \left[ \left( \frac{L}{l} \right)^{1/2}, \left( \frac{l}{L} \right)^{1/2} \right] \left( \frac{V_l}{V_A} \right)^{1/2}, \quad (1.1)$$

where  $V_l$  and  $l$  are the velocity and size of the turbulent eddies at injection scale,  $L$  is the length of the system and  $V_A$  is the Alfvén speed.

The break and rearrangement of the reconnected lines cause the conversion of magnetic energy into kinetic energy and particle acceleration (Zweibel and Yamada, 2009; Yamada et al., 2016).

---

thermal emission from these systems does not allow for direct measurements of their chemical contents. The usual observation of Synchrotron emission from these systems is naturally interpreted as produced by relativistic electrons. But the baryonic contents in these jets are much harder to infer or detect from observations. The simultaneous detection in TSX 0506+056 of gamma-rays and neutrinos has been the first direct signature of a baryonic content in these systems.

<sup>7</sup>The Ohmic resistivity or electric resistivity,  $\eta = m_e \nu_c / n_e e^2$  (where  $\nu_c$  is the collision frequency between electrons and ions,  $m_e$  is the electron mass,  $n_e$  is the local density of electrons and  $e$  is the electron charge), quantifies the resistance of matter to conduct electric charge. The magnetic resistivity coefficient, in turn, is given by  $\nu_M = \eta c^2 / 4\pi$ . Non-null magnetic resistivity allows for reconnection, diffusion and decay of the magnetic field (e.g. Bittencourt, 2004).

de Gouveia Dal Pino and Lazarian (2005) first realized that particles could be accelerated in a fast magnetic reconnection site in a similar way as in diffusive shock acceleration (Bell, 1978; Blandford and Eichler, 1987) by first order Fermi process. For reviews on particle acceleration by magnetic reconnection see, e.g. de Gouveia Dal Pino and Kowal (2015); Matthews et al. (2020). In other words, when particles are trapped between the two converging magnetic flux tubes, they move back and forth between the two fluxes in the reconnection discontinuity (or current sheet) (see the top panel of Figure 1.5), gaining energy due to head-on collisions with magnetic fluctuations at a rate  $\Delta E/E \propto V_R/c$ , which implies a first order Fermi process and an exponential acceleration. This has been successfully tested numerically and Figure 1.5 shows an example of a magnetohydrodynamical (MHD) simulation of a current sheet with a single test particle trapped in it, suffering exponential Fermi acceleration, as described (Kowal et al., 2011) (see also Drake et al., 2006; Kowal et al., 2012).

Kowal et al. (2011), in particular, have demonstrated by means of two- and three-dimensional (2D and 3D) MHD simulations with test particles, the equivalence between this process and that of particles being accelerated within 2D merging magnetic islands (or plasmoids) excited, e.g., by tearing mode instability<sup>8</sup>. It is important to remark that magnetic islands are actually the 2D cross-sections of 3D flux tubes and in real systems, reconnection is 3D, and thus particle accelerates in reconnection sites (e.g. de Gouveia Dal Pino and Kowal, 2015).

The realization that reconnection acceleration can be a fundamental mechanism to explain observed non-thermal, highly variable emission, especially at very-high-energies (VHEs), in magnetically dominated sources, has motivated intensive study mainly through 2D and 3D particle-in-cell (PIC)<sup>9</sup> simulations of current sheets in a slab geometry in kinetic plasmas (e.g. Drake et al., 2006; Zenitani and Hoshino, 2001, 2007, 2008; Lyubarsky and Liverts, 2008; Drake et al., 2010; Clausen-Brown and Lyutikov, 2012; Cerutti et al., 2012; Li et al., 2015; Lyutikov et al., 2017; Werner et al., 2018, 2019; Sironi and Spitkovsky, 2014; Guo et al., 2015, 2016). These studies have probed only the kinetic scales of the process i.e., of a few hundreds of the skin depth length<sup>10</sup>. To assess the stochastic Fermi mechanism at the macroscopic scales of collisional flows present in most astrophysical systems, the tracking of test particle distributions in such flows is also a very useful and complementary tool to help in the understanding of the overall process across the

---

<sup>8</sup>Thin current sheets are generally unstable to resistive reconnecting instabilities, the archetype of which is the tearing mode instability. The fastest modes of this instability have wavelengths greater than the thickness of the current sheet and cause its breaking (Furth et al., 1963; Tenerani et al., 2015).

<sup>9</sup>Particle-in-cell or PIC method modeling the fluid of plasma gives primacy to the kinetic interaction among the constituent particles of the plasma in the self-consistent electric and magnetic fields (Büchner et al., 2003; Tskhakaya, 2008).

<sup>10</sup>The skin depth length of the plasma ( $l_s$ ) is the depth in which low-frequency electromagnetic radiation can penetrate in the plasma. It is given by the relation  $l_s = c/\omega_p$ , where  $\omega_p$  is the plasma frequency (Stenson et al. (2017))

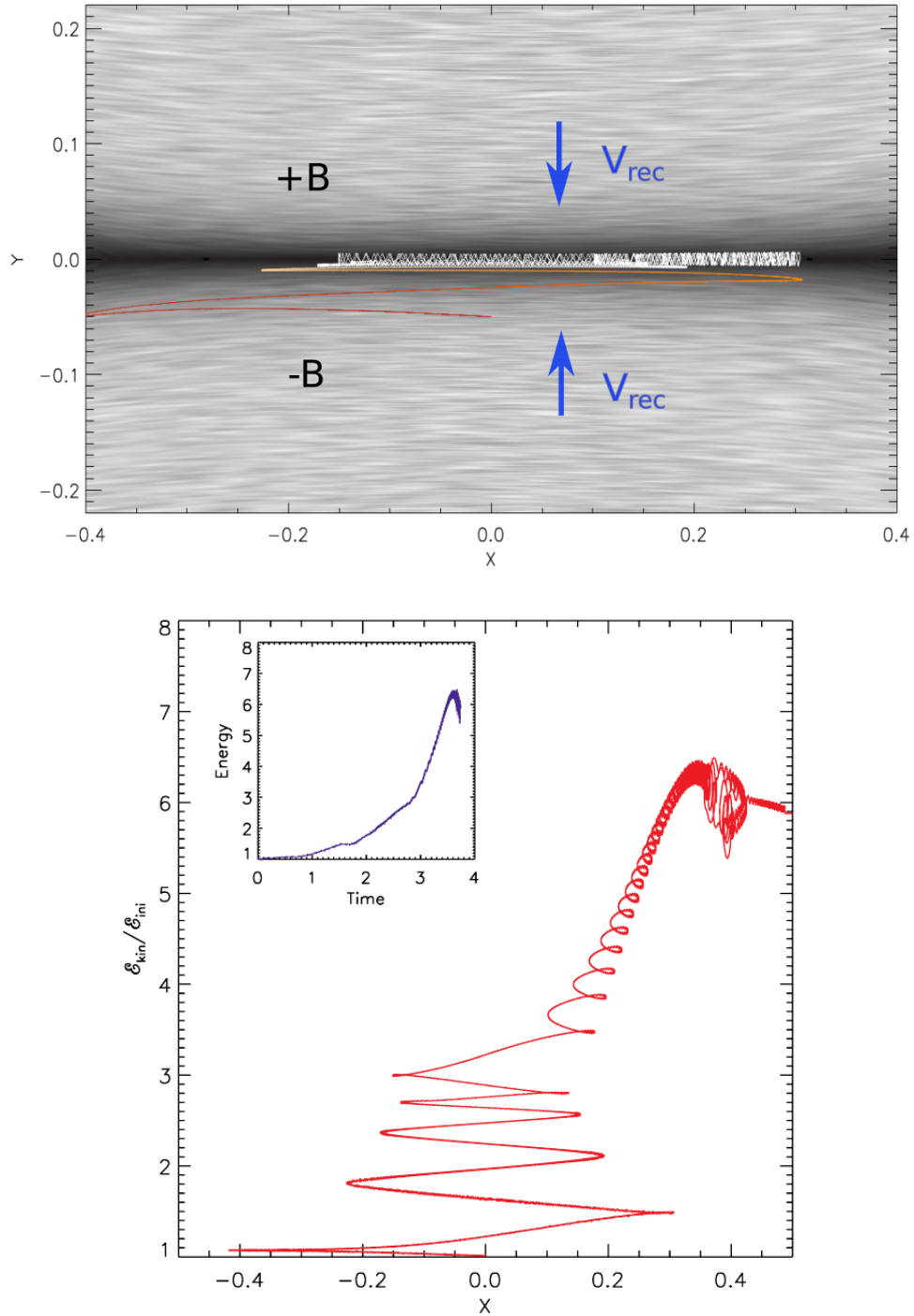


Figure 1.5: Reconnection sheet showing the magnetic field distribution with two fluxes of opposite polarity  $+\mathbf{B}$  and  $-\mathbf{B}$ . In the left panel, the line traces the trajectory of a test particle, when it enters the magnetic field discontinuity (current sheet) it bounces back and forth and its energy increases exponentially. The change of colors in the trajectory from red to white corresponds to the growth of the particle energy. The right panel shows the variation of the particle kinetic energy with the x coordinate and with the time (de Gouveia Dal Pino and Lazarian, 2005; Kowal et al., 2011).

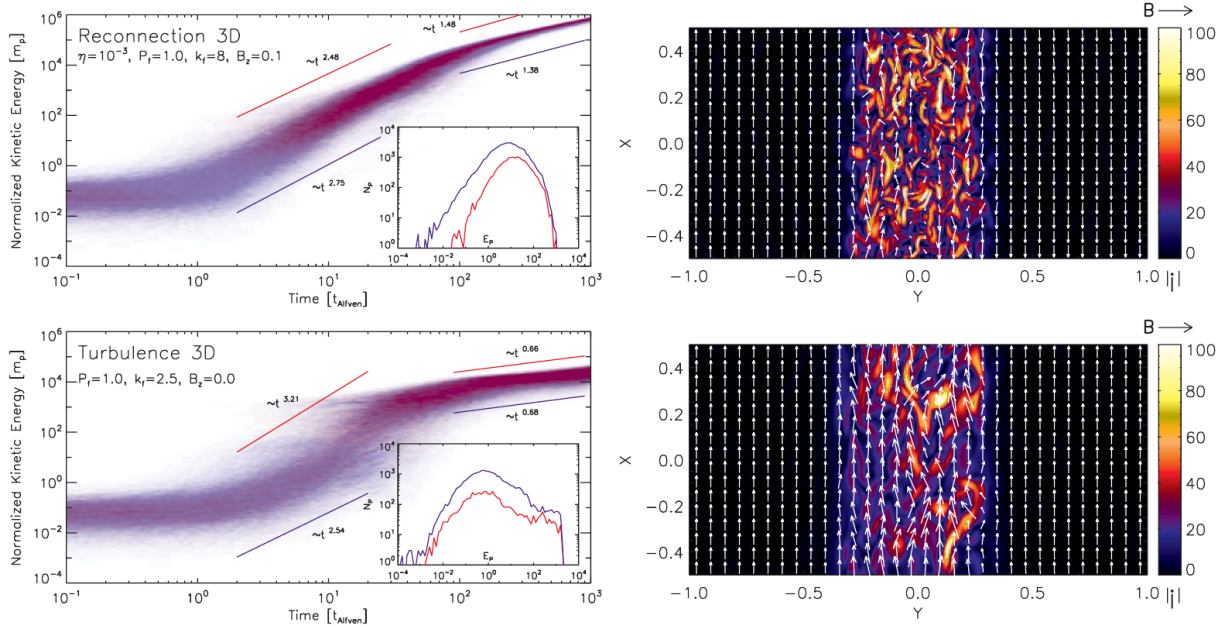


Figure 1.6: The left panels show particle kinetic energy distributions for 10,000 protons injected in fast magnetic reconnection (top) and 3D turbulence (bottom). The colors red or blue indicate the parallel or perpendicular velocity component to the local magnetic field being accelerated. The diagram in the detail shows the accelerated particles spectrum where we see the development of a power law tail in the high energy. In the right panels,  $XY$  cuts through the domain at  $z = 0$  of the absolute value of current density  $|\mathbf{J}|$  overlapped with the magnetic vectors (Kowal et al., 2012).

scales. Such studies have been performed combining 2D and 3D MHD simulations with the injection of thousands of test particles in the reconnection domain (Kowal et al., 2011, 2012; del Valle et al., 2016; Beresnyak and Li, 2016; de Gouveia Dal Pino et al., 2018, 2020).

In particular, Kowal et al. (2012) have distinguished the first order Fermi process that occurs inside large scale current sheets with embedded turbulence driving fast reconnection, from a second order Fermi process<sup>11</sup> occurring in pure turbulent environments (see also Brunetti and Lazarian, 2011; Brunetti and Vazza, 2020). It is worth to note that in a more recent PIC study, (Comisso and Sironi, 2018, 2019) also considered a pure turbulent, magnetically-dominated system, but with no guide field and found that particles are initially exponentially accelerated in small scale reconnecting current sheets and then, undergo further acceleration by stochastic interactions with the turbulent fluctuations at a slower rate. This is, in principle, similar to the process described above, especially in Kowal et al. (2012, see their Figure 1, here shown in the bottom panel of Figure 1.6). But

<sup>11</sup>We note that while the first-order Fermi process favors mainly head-on collisions where particles mostly "gain" energy during the stochastic process within the current sheet, in a second-order Fermi acceleration, there is no large scale converging field and particles can both, gain energy in head-on collisions and also loose energy due to "receding" collisions with the magnetic fluctuations of the turbulent flow. In this case, the energy gain is second order,  $\delta E/E \sim (V_{rec}/c)^2$  (e.g. de Gouveia Dal Pino and Kowal, 2015).

in an MHD environment, the presence of turbulence naturally leads to fast reconnection with the formation of 3D current sheets in the entire turbulent domain (Lazarian-Vishniac theory, Lazarian and Vishniac, 1999) and to stochastic particle acceleration in these sites, as described previously. A key difference between Comisso and Sironi (2018, 2019) simulations and those of Kowal et al. (2012) (and the ones in the present work, see Chapter 3) is that in the latter there is the underlying large scale magnetic field that favors the confinement of the particles in the regions where the current sheets are formed and thus the exponential acceleration can be sustained longer and not only during the initial stages.

Both, PIC and test particle+MHD approaches have probed the efficiency of the stochastic reconnection acceleration, particularly in 3D dimensions, with an exponential growth of the particle energy in time, implying a power-law energy dependence of the acceleration rate, and the production of an extended, non-thermal distribution of relativistic particles with a power-law tail (e.g., del Valle et al., 2016). The results above are applicable to magnetized astrophysical flows in general and especially to relativistic jets in regions near the source where they are possibly magnetically dominated. The investigation of magnetic reconnection acceleration in these objects is the main goal of the present thesis.

## 1.3 Fast magnetic reconnection in relativistic jets

The presence of instabilities in the jet can drive turbulence and thus fast magnetic reconnection (e.g., Spruit et al., 2001; Barniol Duran et al., 2017; de Gouveia Dal Pino et al., 2018; Gill et al., 2018). In particular, jets with helical magnetic field structure can be subject to the current-driven kink (CDK) instability (e.g., Begelman, 1998; Giannios and Spruit, 2006; Mizuno et al., 2009, 2011, 2012, 2014; Das and Begelman, 2019).

### 1.3.1 Current-driven kink instability (CDKI)

It is known, from theory and laboratory experiments of plasma physics that cylindrical, magnetized plasmas are unstable to various kinds of instabilities (Bateman, 1978; Hsu and Bellan, 2002; Bellan et al., 2005; Moser and Bellan, 2012). In magnetized outflows, the instabilities can be driven by two classes, pressure-driven and current-driven instabilities (Das and Begelman, 2019). Pressure-driven instability is induced by the electric current perpendicular to the magnetic field ( $j_{\perp}$ ) and by the interaction between the pressure of the gas and the magnetic tension of the magnetic field lines, and the instability occurs when the plasma pressure gradient is strong enough to push the plasma out of the curvature of magnetic field lines. Current-driven instabilities are driven by the current parallel to the magnetic field ( $j_{\parallel}$ ).

Let us consider a cylindrical jet with initial helical magnetic field geometry, with the poloidal (or  $B_r$  and  $B_z$ ) and toroidal ( $B_\phi$ ) components. When the column of plasma of the straight jet suffers a kink in the transverse direction, the toroidal magnetic field component is first distorted on one side only, creating an unbalancing on the magnetic tension force between this side and the opposite one, that leads to further tension and distortion of the column, as we see in Figure 1.7.

Quantitatively, if the toroidal field is dominant, then the jet is subject to this current-driven kink instability (Begelman, 1998), and the so called Kruskal-Shafranov criterion for this instability (Bateman, 1978),

$$q_{crit} > \frac{2\pi R}{L_z} \left| \frac{B_p}{B_\phi} \right|, \quad (1.2)$$

where  $R$  is the jet radius,  $L_z$  its length, and  $q_{crit} = 1$  for ideal MHD and smaller than 1 for RMHD and rotating jets (Narayan et al., 2009; Guan et al., 2014). Thus, in configurations with strong toroidal magnetic field, the CDK mode is unstable, and the growth time of the CDK is calculated by (Bateman, 1978)

$$t_{kink} \simeq \frac{2\pi R}{c} \frac{B_p}{B_\phi}. \quad (1.3)$$

where  $c$  is the speed of light.

More generally, in 3D jet structures, we can investigate the stability of cylindrical magnetized flows initially in equilibrium if we consider perturbations on the magnetic field of the form (Lyubarskii, 1999; Hardee, 2004)

$$f(r, \phi, z) = f(r) \exp\{i(\omega t + m\phi - kz)\}, \quad (1.4)$$

where the flow is along the  $z$ -axis,  $m$  is an integer azimuthal wavenumber which describes different models of instability,  $k$  is vertical wavenumber and  $\omega$  is the modal frequency. Different types of instabilities are developed for different values of modes, which involve pinch ( $m = 0$ ), helical or kink ( $m = \pm 1$ ), elliptical ( $m = \pm 2$ ) or triangular ( $m = \pm 3$ ) (see Figure 1.8). For instabilities with  $m \neq 0$  the wave propagates at an angle to the flow direction. The positive or negative sign specifies the wave propagation direction, when viewed outwards along with the flow in the clockwise and counterclockwise sense, respectively. The fastest-growing mode is  $|m| = 1$ , i.e. the CDKI, because it affects the jet axis, and its center of mass changes into a spiral shape. For all other values of  $|m|$ , the center of mass remains on the axis and the perturbations are concentrated on the outside (see for more details on this instability Bateman, 1978; Begelman, 1998; Lyubarskii, 1999; Hardee, 2004; Braithwaite, 2006; Narayan et al., 2009; Das and Begelman, 2019).

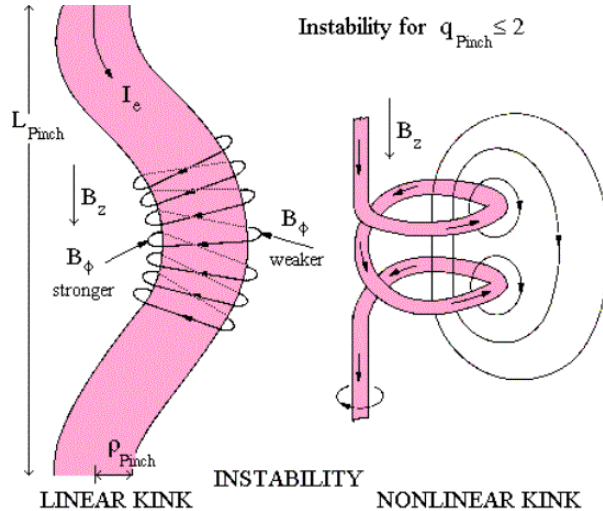


Figure 1.7: This panel shows the distortion of the helical magnetic field caused by the kink instability (Roth, 1997).

### 1.3.2 Magnetic reconnection driven by CDKI

As we have explained above, jets with strong helical or toroidal fields are subject to CDKI. This instability distorts the jet column and induces non-helical currents that ultimately can break the magnetic field lines and drive magnetic reconnection (see Figure 1.7). In this work, we will investigate the acceleration of particles mainly by magnetic reconnection induced by CDKI in relativistic jets.

A number of recent numerical works have revealed that this instability can operate in the jet spine without disrupting the entire jet structure, converting magnetic into kinetic energy, and driving reconnection (Porth and Komissarov, 2015; Singh et al., 2016; Bromberg and Tchekhovskoy, 2016; Tchekhovskoy and Bromberg, 2016; Striani et al., 2016; Bromberg et al., 2019; Davelaar et al., 2020). In particular, in their 3D relativistic MHD (RMHD) simulations of Poynting flux dominated, rotating jets with helical fields, Singh et al. (2016) verified that the CDK-induced-turbulence triggers the formation of current-sheets with fast reconnection rates  $\sim 0.05V_A$ . Following Singh et al. (2016), in this work, we will perform numerical simulations of relativistic jets and drive this instability in order to excite the formation of fast reconnection, which will allow for particle acceleration investigation.

## 1.4 Another particle acceleration mechanism: magnetic curvature drift

Current driven kink instability (CDKI) in a jet can drive another particle acceleration mechanism. Magnetic curvature drift is produced when the magnetic field lines are curved

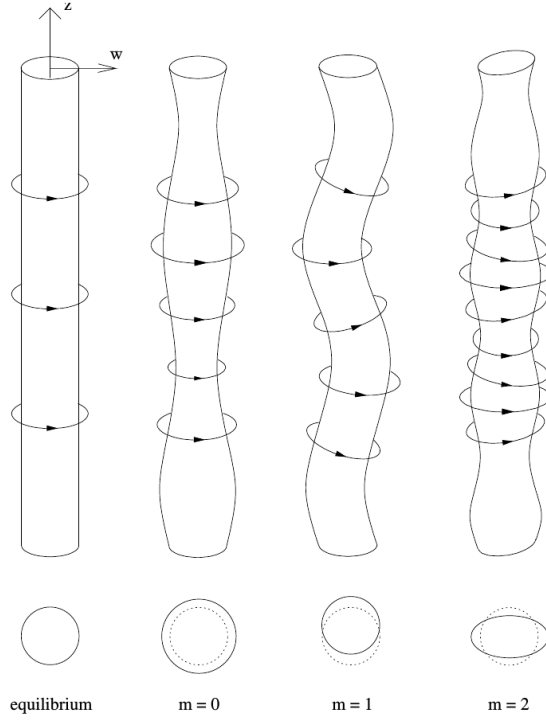


Figure 1.8: Types of instabilities in the plasma column with strong toroidal magnetic fields for modes  $m = 0$ ,  $m = 1$  and  $m = 2$  where  $m = 1$  corresponds to the kink instability (Braithwaite, 2006).

and the particle has a velocity component ( $v_{\parallel}$ ) along the curved field (Alves et al., 2018). The particles experiment a centrifugal force perpendicular to the magnetic field

$$\mathbf{F}_c = \gamma m v_{\parallel}^2 \frac{\mathbf{R}_c}{R_c^2}, \quad (1.5)$$

where  $R_c$  is the radius of curvature of the magnetic field lines. Then, the curvature drift (in Gaussian units) is,

$$\mathbf{v}_{curv} = \frac{c}{q} \frac{\mathbf{F}_c \times \mathbf{B}}{B^2} = -\frac{\gamma m v_{\parallel}^2 c}{q} \frac{\mathbf{R}_c \times \mathbf{B}}{R_c^2 B^2} = \frac{\gamma m v_{\parallel}^2 c}{q} \frac{\mathbf{B} \times (\mathbf{B} \cdot \nabla \mathbf{B})}{B^4}, \quad (1.6)$$

where  $\gamma$  is the Lorentz factor,  $c$  the light speed,  $m$  and  $q$  are the mass and the charge of the particle, respectively (Bittencourt, 2004).

As we mentioned earlier, the CDKI causes the jets to move bodily in a transverse direction and develop helical motions of the jet spine. These sideways motions give rise to an inductive electric field  $\mathbf{E} = -\mathbf{v} \times \mathbf{B}/c$ . In Alves et al. (2018), the authors investigated particle acceleration in the early non-linear stage of the CDKI, before the development of turbulence and the break of the magnetic field lines, and verified that particles are accelerated by magnetic curvature drift. They show that a net axial electric field emerges as a consequence of the nonlinear development of the CDKI. Figure 1.9 extracted from Alves et al. (2018) is a schematic 2D representation of the  $yz$ -plane of the center of the

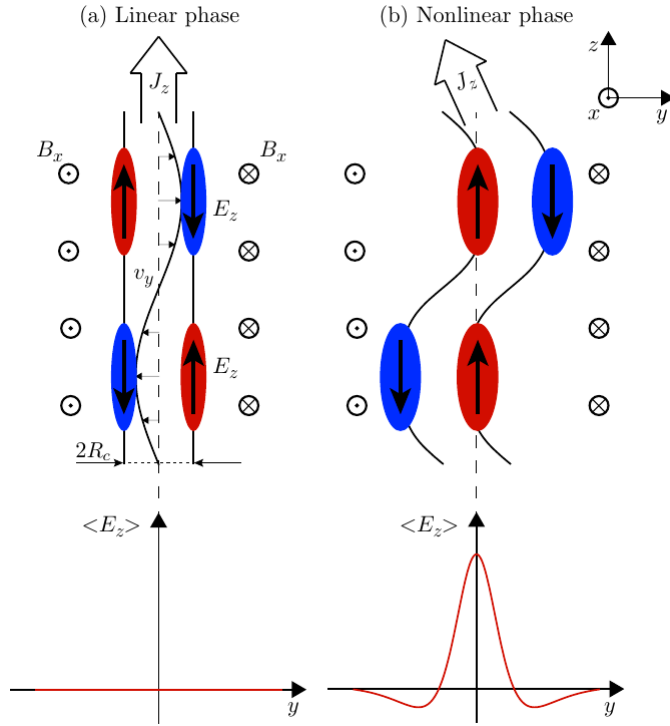


Figure 1.9: Schematic representation of the development of curvature drift acceleration (see text for more details) (extracted from Alves et al., 2018).

jet. It shows the velocity  $v_y$  of the flow along the axis as a consequence of the radial motions of the jet by the CDKI, and the direction of the toroidal magnetic field by  $B_x$ . In this 2D representation of the jet, the inductive electric field is given by  $E_z = v_y B_x / c$ , and in early stages the axially averaged electric field  $\langle E_z \rangle$  is practically null, but as the distortion of the jet grows,  $\langle E_z \rangle$  increases (see right panel of Figure 1.9) giving rise to an acceleration of particles in this direction. Alves et al. (2018) find that this electric field enables particle acceleration perpendicular to the magnetic field lines via the guiding center curvature drift with a velocity equal to equation (1.6).

In Chapter 3, we will see that this particle acceleration process also occurs in our simulations in the early stages of the development of the CDKI in the jet.

## 1.5 Goal of this work

In this thesis, we will expand upon the previous studies described above. We will perform 3D special relativistic magnetohydrodynamical (SRMHD) simulations of a Poynting-flux-dominated jet with an initial helical magnetic field, subject to the CDKI. Then, we will apply a magnetic reconnection search-algorithm, developed in Kadowaki et al. (2018b) to the simulated jet (Singh et al., 2016). With this search algorithm, we will identify sites of reconnection and obtain robust values of the reconnection rates and the magnetic power

of every reconnection events inside the jet, in different snapshots, as well as the topological characteristics of each reconnection region (see also Kadowaki et al., 2018a). Then, in order to obtain a full understanding of how the magnetic energy released by reconnection can be channeled into energetic nonthermal particles in the fast reconnection regions, we will investigate *in situ* particle acceleration by injecting hundreds to thousands of test particles in the 3D SRMHD jet model.

Below, we give the guide lines of the next chapters of this thesis. In Chapter 2, we describe the numerical methodology and the setup of the codes that we employ in this thesis, namely the SRMHD code for the jet simulation (RAISHIN, Mizuno et al., 2006, 2011, 2012, 2014; Singh et al., 2016), the search algorithm of reconnection sites (Kadowaki et al., 2018b), and the test particle acceleration code (GACCEL, Kowal et al., 2011, 2012). In Chapter 3, we present the results of this work, i.e., the acceleration of test particles mostly by magnetic reconnection driven in the relativistic jet by the development of the CDKI. We obtain the properties of the acceleration such as the particles energy growth with time, the acceleration rate, and the particles spectrum, as well as the spatial correlations of the accelerated particles with the reconnection regions. Finally, in Chapter 4, we discuss our findings, compare our results with former numerical studies and present the prospects for futures works.

We should remark that the results of this thesis have been summarized in two papers recently submitted to publication Medina-Torrejón et al. (2021); Kadowaki et al. (2021), The first of which is already published and the second already accepted. Preliminary results of this study have been also presented in de Gouveia Dal Pino et al. (2018, 2020).

## Chapter 2

# Numerical Methodology for Relativistic MHD Jet Simulations and Test Particle Simulations

In this chapter, we describe the numerical methodology employed to develop our study.

As stressed, we investigate in this work the acceleration of particles injected in a three-dimensional (3D) relativistic magnetohydrodynamical jet subject to current-driven kink instability (CDKI), which drives turbulence and fast magnetic reconnection. Following Kowal et al. (2011, 2012) and del Valle et al. (2016) (see also de Gouveia Dal Pino and Kowal, 2015), we inject test particles (100 - 10,000 protons) into frozen-in-time 3D MHD domains. However, instead of taking a large scale single current-sheet with embedded controlled weak stochastic turbulence, as in these former works (see also del Valle et al., 2016; de Gouveia Dal Pino and Kowal, 2015), we consider here *in – situ* particle acceleration in a relativistic 3D MHD jet where turbulence and fast magnetic reconnection are naturally induced by CDKI Mizuno et al. (2012); Singh et al. (2016). As in Kowal et al. (2011, 2012), we neglect the macroscopic MHD dynamical time variations (see further justification for this in Chapter 3). Once the instability reaches saturation and turbulence is fully developed with the appearance of several sites of fast reconnection in the jet, we inject test particles into a snapshot to follow their acceleration. Furthermore, in order to identify magnetic reconnection regions in our jet domain built by the MHD simulations, we used an algorithm developed by Kadowaki et al. (2018b); ? which identifies current density ( $\mathbf{J} = c\nabla \times \mathbf{B}/4\pi$ ) peaks characterizing the presence of magnetic discontinuities or current sheets in a given simulation snapshot.

We describe in the next sections the numerical methods for these three parts of our study, namely, for the 3D MHD relativistic simulations of the jet, using the RAISHIN code (Mizuno et al., 2006, 2011, 2012), for the search algorithm of magnetic reconnection

regions (Kadowaki et al., 2018b), and for the test particle simulations employing the GACCEL code (Kowal et al., 2011, 2012; del Valle et al., 2016).

## 2.1 3D MHD simulations of Relativistic jets

We perform special relativistic magnetohydrodynamics (SRMHD) simulations of a jet using the 3D well tested general relativistic magnetohydrodynamics (GRMHD) code RAISHIN (Mizuno et al., 2006, 2011, 2014). We consider in this analysis a fully developed jet, taking a portion of it (tower jet), far enough from the progenitor source and also far enough from its terminal shock (the jet head). We adopt an Eulerian frame moving with the bulk velocity of the flow.

RAISHIN code utilizes conservative, high-resolution shock capturing scheme (Godunov type scheme) to solve the 3D ideal SRMHD equations. We have employed a Harten-Lax-van Leer-Einfeldt (HLLC) approximate Riemann solver to compute the intercell fluxes in the computational grid (see Einfeldt, 1988; Komissarov, 1999). Besides, a method of flux-interpolated, constrained transport (flux-CT) is used to maintain a divergence-free magnetic field <sup>1</sup>. We employ the flux-CT scheme introduced by (Tóth, 2000). For the time advance of the equations, we use a multistep TVD Runge-Kutta third-order (RK3) method (e.g. Bodenheimer et al., 2006). In Appendix A, we describe briefly the Godunov scheme with the HLLC Riemann solver here employed and in Appendix B the flux-CT scheme. For more details, see Mizuno et al. (2006, 2011).

We integrate numerically the fundamental MHD variables  $\mathbf{P} = (\rho, p, v^i, B^k)$ , called the “primitive variables”, where  $\rho$  is the rest-mass density (measured in the comoving frame),  $p$  is the gas pressure and  $v^i$  is the three velocity vector of the fluid as measured by the Eulerian observer and  $B^k$  is the three vector of the magnetic field measured also in the Eulerian frame. The evolution of the MHD equations is written in conservative form. They give the time derivatives for “conserved” variables  $\mathbf{U}(\mathbf{P})$  in terms of source variables  $\mathbf{S}(\mathbf{P})$  and the divergence of flux variables  $\mathbf{F}$ . The evolution of the eight scalar fluid equations of GRMHD can be written in a compact way as follows (Mizuno et al., 2006; Del Zanna et al., 2007),

$$\frac{\partial \mathbf{U}}{\partial t} + \frac{\partial \mathbf{F}^i(\mathbf{U})}{\partial x^i} = \mathbf{S} . \quad (2.1)$$

In our simulations we use the metric of Minkowski as an appropriate one to integrate the SRMHD equations without source variables ( $\mathbf{S} = 0$ ). The conserved form for SRMHD

---

<sup>1</sup>In a numerical solution the absence of magnetic monopoles is not satisfied because of the numerical errors. In order to maintain divergence-free magnetic fields in the RAISHIN code, it is used flux-interpolated, constrained transport scheme (Tóth, 2000). This scheme conserves  $\nabla \cdot B = 0$  at each grid cell.

is:

$$\frac{\partial \mathbf{U}}{\partial t} + \frac{\partial \mathbf{F}^i(\mathbf{U})}{\partial x^i} = 0, \quad (2.2)$$

where the quantities  $\mathbf{U}$  and  $\mathbf{F}$  are

$$\mathbf{U} = \begin{pmatrix} D \\ S^j \\ \tau \\ B^k \end{pmatrix}, \quad (2.3)$$

$$\mathbf{F}^i = \begin{pmatrix} Dv^i \\ S^j v^i + (p + b^2/2)\delta^{ij} - b^j B^i/\gamma \\ \tau v^i + (p + b^2/2)v^i - b^t B^i/\gamma \\ v^i B^k - v^k B^i \end{pmatrix}, \quad (2.4)$$

where  $D = \gamma\rho$  is the mass density measured by the Eulerian observer,  $\gamma = (1 - v^2)^{-1/2}$  is the Lorentz factor,  $S_i$  is the momentum density of the magnetized fluid,

$$S_i = (\rho h + b^2)\gamma^2 v_i - b^t b_i, \quad (2.5)$$

$h = 1 + u + p/\rho$  is the specific enthalpy, and  $u$  is internal energy,  $b^\mu$  is the magnetic field 4-vector measured by a comoving observer

$$b^t = \gamma(\mathbf{v} \cdot \mathbf{B}), \quad (2.6)$$

$$b^i = \frac{B^i}{\gamma} + v^i b^t, \quad (2.7)$$

$\tau$  is the total energy density,

$$\tau = (\rho h + b^2)\gamma^2 - (p + \frac{b^2}{2}) - (b^t)^2 - D. \quad (2.8)$$

In order to close our system of equations, we have adopted an ideal gas equation of state with  $p = (\Gamma - 1)\rho u$ , where  $\Gamma = 5/3$  the adiabatic index.

### 2.1.1 Initial and Boundary Conditions

The code setup for the spatial development of CDKI is similar to one in Mizuno et al. (2012) and Singh et al. (2016), that is, a jet rotating with an angular velocity  $\Omega_0 = 2.0$  in code units with an initial force-free helical magnetic field and decreasing radial density

profile.

The computational domain is  $6L \times 6L \times 6L$  in a Cartesian  $(x, y, z)$  coordinate system, where  $L$  is the length scale unit of the computation domain. The code unit (c.u.) for the velocity is the speed of light  $c$ , the magnetic field is in units of  $\sqrt{4\pi\rho_0 c^2}$ , the density is in units of  $\rho_0$  (being  $\rho_0 = 1.0$  in the code), the pressure is in units of  $\rho_0 c^2$  and the time is in units of  $L/c$ .

We have chosen, in our simulations, a force-free helical magnetic field for the initial configuration with constant pitch ( $\mathcal{P} = RB_z/B_\phi$ ) (Mizuno et al., 2009, 2011). The force-free steady-state equilibrium of a rotating jet in cylindrical coordinates  $(R, \phi, z)$  is described by (Istomin and Pariev, 1994)

$$\frac{\Omega B_z}{c^2} \frac{d}{dR}(\Omega R^2 B_z) = B_z \frac{dB_z}{dR} + \frac{B_\phi}{R} \frac{d}{dR}(RB_\phi), \quad (2.9)$$

where  $\Omega$  is the angular velocity of a magnetic field  $B = (0, B_\phi, B_z)$ . Based on previous works (Mizuno et al., 2012; Singh et al., 2016), the initial angular velocity of the jet is written in the following form

$$\Omega = \begin{cases} \Omega_0 & \text{if } R \leq R_0 \\ \Omega_0 R_0/R & \text{if } R > R_0, \end{cases} \quad (2.10)$$

here  $R_0$  is the radius of the jet core. In the simulations  $R_0 = (1/4)L$  and  $\Omega_0 = 2.0 c/L$ . The initial poloidal magnetic field component of the jet is

$$B_z = \frac{B_0}{1 + (R/a)^2}, \quad (2.11)$$

where  $a$  is the characteristic radius of the magnetic field, for the simulations  $a = R_0 = (1/4)L$ . From (2.9) and this poloidal magnetic field, an analytical solution for the toroidal magnetic field is given by

$$B_\phi = -\frac{B_0(R/a)[1 + (\Omega a)^2]^{1/2}}{1 + (R/a)^2}. \quad (2.12)$$

In force-free MHD, the true plasma velocity is undefined. As we only can define the drift velocity ( $\mathbf{v} = c\mathbf{E} \times \mathbf{B}/B^2$ ) in the chosen configuration for the simulation, the initial poloidal and toroidal components of the drift velocity are given by

$$v_z = -\frac{B_\phi B_z}{B^2} \Omega R, \quad (2.13)$$

$$v_\phi = \left(1 - \frac{B_\phi^2}{B^2}\right) \Omega R. \quad (2.14)$$

The initial density profile decreases with the radius according to

$$\rho = \rho_1 \sqrt{\frac{B^2}{B_0^2}} \quad (2.15)$$

where  $\rho_1 = 0.8\rho_0$  and the magnetic field amplitude is  $B_0 = 0.7$  c.u. at the jet spine.

We assume an initial gas pressure decreasing radially, similar to equation (2.10)

$$p = \begin{cases} p_0 & \text{if } R \leq R_p \\ p_0 R_p / R & \text{if } R > R_p, \end{cases} \quad (2.16)$$

with  $R_p = (1/2)L$  and  $p_0 = 0.02$  in units of  $\rho_0 c^2$ . These values correspond to an initial beta parameter  $\beta = p_0 / (B_0^2 / 8\pi) = 0.08$  and a magnetization parameter  $\sigma_0 = B_0^2 / \gamma^2 \rho h = 0.6$  (where  $h$  is the specific enthalpy) at the jet axis. The sound speed is given by  $c_s / c = (\Gamma p / \rho h)^{1/2}$ , the Alfvén speed is given by

$$\frac{v_A}{c} \equiv \left[ \frac{b^2}{\rho h + b^2} \right]^{1/2}, \quad (2.17)$$

where  $\mathbf{b}$  is the magnetic field measured in the comoving frame,

$$b^2 = \frac{B^2}{\gamma^2} + (\mathbf{v} \cdot \mathbf{B})^2, \quad (2.18)$$

where  $\gamma$  is the bulk Lorentz factor of the jet. The initial profiles are presented in Figure 2.1, where we show the initial magnetic field components, the velocity components, the density, and Alfvén speed as a function of the radial distance to the jet axis.

In order to drive the instability and induce turbulence, we break the symmetry at the initial MHD equilibrium configuration applying a precession perturbation in all regions with a radial velocity profile given by

$$\frac{v_R}{c} = \frac{\delta v}{N} \exp\left(-\frac{R}{R_a}\right) \sum_{n=1}^N \cos(m\theta) \sin\left(\frac{\pi n z}{L_z}\right), \quad (2.19)$$

where the amplitude of the perturbation is  $\delta v = 0.01c$ , the radial width  $R_a = 0.25L$ ,  $N = 8$ ,  $\lambda = 2\pi/k = L_z/n$  and  $L_z = 6L$  is the grid length in  $z$  direction,  $k = 2\pi n/L_z$  the wave number, and we consider the mode  $m = 1$  in order to induce the CDK instability (see Chapter 1).

Table 2.1 gives the initial conditions for the jet model. We consider two different grid resolutions in the three directions:  $\Delta L = L/40$ , corresponding to 240 cells in each direction (model j240 in Table 2.1), and  $\Delta L = L/80$ , corresponding to 480 cells in each direction (model j480 in Table 2.1). Both models, j240 and j480 have the same initial

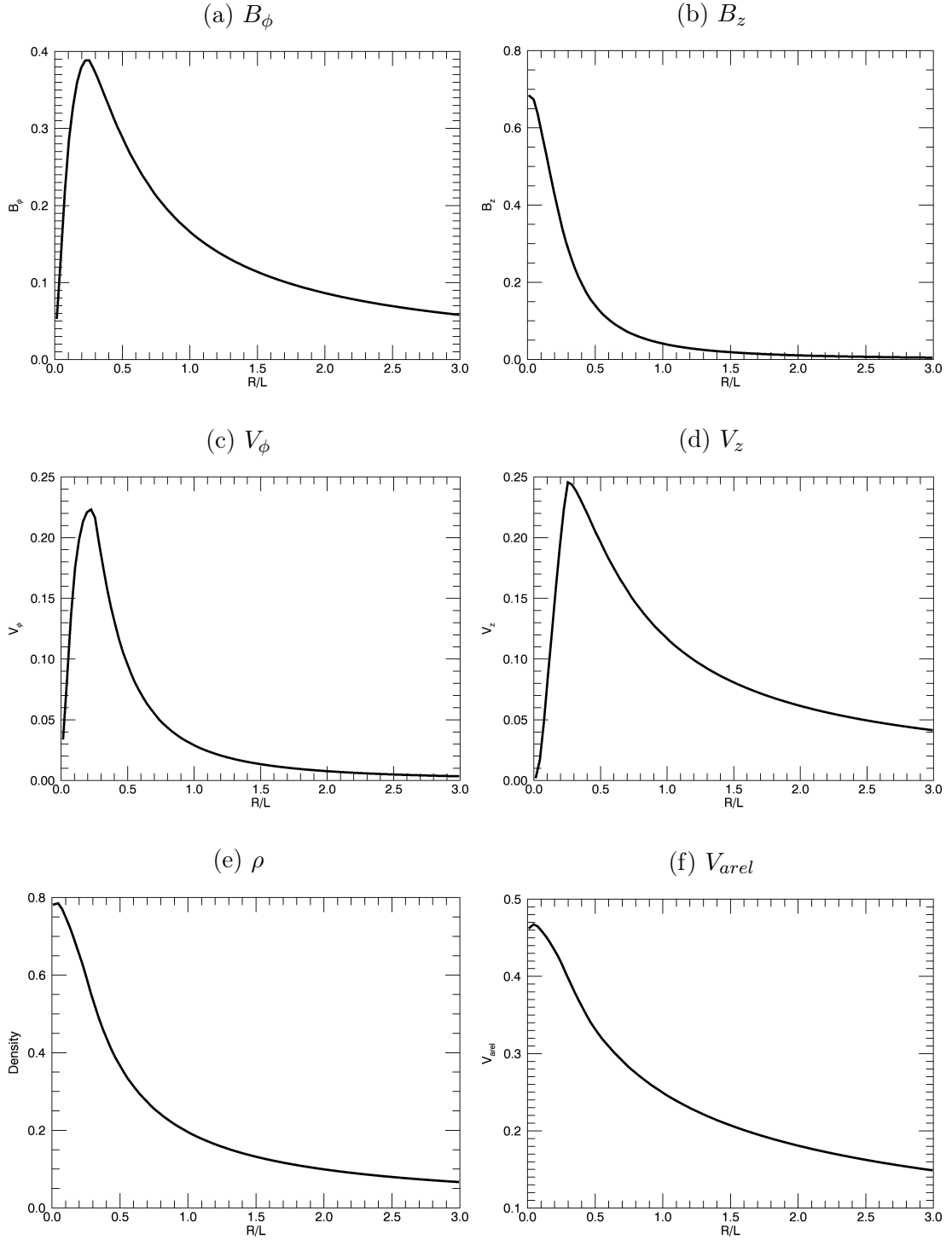


Figure 2.1: Radial profiles of the initial parameters for the simulations j240 and j480: Radial profiles of (a) the toroidal magnetic field  $|B_\phi|$  (in units of  $\sqrt{4\pi\rho_0 c^2}$ ), (b) the axial magnetic field  $B_z$  (also in units of  $\sqrt{4\pi\rho_0 c^2}$ ), (c) the toroidal velocity  $v_\phi$  (in units of  $c$ ), (d) the axial velocity  $v_z$  (also in units of  $c$ ), (e) the density  $\rho$  (in units of  $\rho_0$ ) for a decreasing density profile with  $\Omega_0 = 2.0$  and (f) the Alfvén speed  $v_A/c$ .

Table 2.1: Parameters for the MHD simulations.

Model	Resolution	$p_0[\rho_0 c^2]$	$B_0[\sqrt{4\pi\rho_0 c^2}]$	$\Omega_0[c/L]$	$R_0[L]$	$\sigma_0$
$j240$	$240^3$	0.02	0.7	2.0	0.25	0.6
$j480$	$480^3$	0.02	0.7	2.0	0.25	0.6

conditions. In Table 2.1,  $p_0$ ,  $B_0$  and  $\Omega_0$  are the initial gas pressure, the initial poloidal magnetic field, and the jet initial angular velocity in the jet axis, respectively.  $R_0$  is the initial radius of the jet core, before the perturbation. The initial magnetization is  $\sigma_0 = B_0^2/\gamma^2\rho h = 0.6$  (where  $h$  is the specific enthalpy) at the jet axis. The latter increases to maximum values around unity in more evolved times (see Chapter 3). We should remark that, although it is generally believed that the jet is highly magnetized at the launching site (Chapter 1), the location of the region where effective acceleration and radiative dissipation occurs is not well understood yet. Nevertheless, it is reasonable to suppose that an efficient reconnection acceleration and dissipation should occur when the magnetization has decreased to values  $\sigma \sim 1$ . This is, in fact, compatible with a recent proposal by Giannios and Uzdensky (2019). In this work, we will explore a similar magnetization condition (Chapter 3).

We impose outflow boundaries (i.e. zero gradients for all variables) in the transverse directions  $x$  and  $y$  (at  $x = y = \pm 3L$ ), and adopt periodic boundaries in the  $z$  direction in a similar way to the setup in Mizuno et al. (2009, 2011, 2012). Outflow conditions allow all the variables to evolve freely at the transverse boundaries avoiding artificial numerical effects. The periodic boundaries in the  $z$ -direction allow to maintain the CDKI growing until the saturation and disruption inside of the domain (see Chapter 3).

## 2.2 Algorithm of identification of current sheets

The aim of the magnetic reconnection search algorithm (Kadowaki et al., 2018b; ?) is to locate current sheets in an MHD fluid. The first step is to calculate the local maximum magnitude of the current density ( $\mathbf{J} = c\nabla \times \mathbf{B}/4\pi$ ). The algorithm scans through all points with current density values greater than the globally averaged magnitude of current density ( $j > \langle |\mathbf{J}| \rangle$ ), and sets a threshold current density

$$j_{thr} = \varepsilon \langle |\mathbf{J}| \rangle, \quad (2.20)$$

where  $\varepsilon > 1$  is a free parameter. Within a surrounding cubic subarray whose size we can choose, the algorithm selects those cells that have local maximum ( $j_{max} = MAX(|\mathbf{J}|)$ ), and each subarray is centered at the candidate point (see Figure 2.2).

To identify the points of each given current sheet, the following condition must be

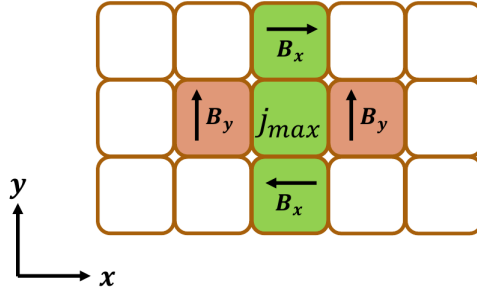


Figure 2.2: Sketch sample of a 2D subarray centered at the cell with  $j_{max}$  identified. The choice of the size is  $3 \times 3$  cells.

satisfied, each point must have a magnitude of current density greater than a minimal value,

$$j_{min} = bj_{max}, \quad (2.21)$$

where  $b$  is a parameter ( $b < 1$ ). The current sheet is determined considering the points adjacent to the peak with current densities greater than  $j_{min}$  (for 2D analysis we determine four points, for 3D analysis six points) and also from this list, the algorithm adds the adjacent points with current densities above  $j_{min}$ .

The next step of the algorithm is to check whether the local maximum is located between magnetic field lines of opposite polarity. The cells that follow this condition of opposite polarity are possible sites of reconnection. Following what Zhdankin et al. (2013) done to measure the current sheet thickness, we can determine the direction of the fastest drops in current density (or the highest variance of  $|\mathbf{J}|$ ) from the peak, computing numerically the current density 3D Hessian matrix ( $H_{ijk}$ ) at the peak, which corresponds to the second-order partial derivatives of the current density magnitude,

$$H_{ijk} = \begin{bmatrix} \partial_{xx}|\mathbf{J}|_{ijk}^{max} & \partial_{xy}|\mathbf{J}|_{ijk}^{max} & \partial_{xz}|\mathbf{J}|_{ijk}^{max} \\ \partial_{yx}|\mathbf{J}|_{ijk}^{max} & \partial_{yy}|\mathbf{J}|_{ijk}^{max} & \partial_{yz}|\mathbf{J}|_{ijk}^{max} \\ \partial_{zx}|\mathbf{J}|_{ijk}^{max} & \partial_{zy}|\mathbf{J}|_{ijk}^{max} & \partial_{zz}|\mathbf{J}|_{ijk}^{max} \end{bmatrix}. \quad (2.22)$$

Since the magnetic reconnection topology is complex in a 3D regime and the lines are not necessarily aligned with one of the axes of the Cartesian coordinate system, the algorithm adopts a new coordinate system centered in the local reconnection site obtained from the eigenvalues and eigenvectors of the 3D current density  $H_{ijk}$ . The eigenvectors of  $H_{ijk}$  provide the three orthonormal vectors of the new coordinate system centered in the local reconnection site (the directions will be represented by the unit vectors  $\hat{\mathbf{e}}_i$ , where  $i = 1, 2$  or  $3$ ), see Figure 2.3. The eigenvector associated with the highest eigenvalue of  $H_{ijk}$ , and as we mentioned above, corresponds to the direction of the highest variance of  $|\mathbf{J}|$ , this direction is assumed as the thickness of the magnetic reconnection site. In this work, this direction will be represented by the unit vectors  $\hat{\mathbf{e}}_1$ .

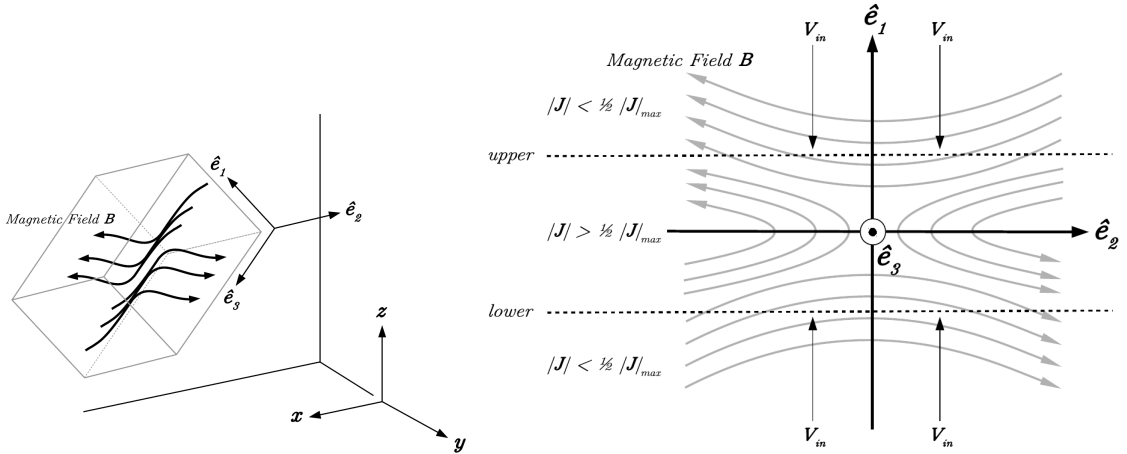


Figure 2.3: The left sketch shows a new coordinate system centered in a local reconnection site. The right sketch shows how the edges have been defined as the cells with  $|\mathbf{J}| \sim 1/2|\mathbf{J}_{max}|$  (Kadowaki et al., 2018b).

The algorithm also allows for the determination of the reconnection velocity. Similarly as in Kowal et al. (2009), the reconnection rate  $V_{rec} = \langle V_{in}/V_A \rangle$  is measured by averaging the inflow velocity  $V_{in}$  divided by the Alfvén speed  $V_A$  at the edges of the reconnection site

$$V_{rec} = \frac{[h_r |V_{e1}|/V_A]_{lower} + [h_r |V_{e1}|/V_A]_{upper}}{[h_r]_{lower} + [h_r]_{upper}}, \quad (2.23)$$

where  $|V_{e1}| = |V_{in}|$  is the projection onto the  $e_1$  direction, the absolute inflow velocity at the reconnection edges. And,  $h_r$  is the distance of the (lower or upper) edges to the center of the diffusion region.

The relativistic Alfvén speed is given by equations (2.17) and (2.18), where  $\mathbf{B} = B_{\hat{e}_1}\hat{e}_1 + B_{\hat{e}_2}\hat{e}_2 + B_{\hat{e}_3}\hat{e}_3$  is the magnetic field measured through the projection onto the three eigenvectors of the Hessian matrix. The algorithm identifies the edges and the cells belonging to a given local magnetic reconnection site, as shown in the right sketch of Figure 2.3, considering only sites with current density  $|\mathbf{J}|$  greater than half of the maximum local value given by  $|\mathbf{J}|_{max}$ . The algorithm also constrains the selection of reconnection sites based on the symmetry of the inflow velocity and the magnetic field components around the magnetic discontinuity. This constraint reduces considerably over or underestimations of the reconnection velocity. Figure 2.4 shows examples of rejected and accepted profiles of  $v_{\hat{e}_1}$ ,  $B_{\hat{e}_2}$  and  $B_{\hat{e}_3}$  interpolated along the  $\hat{e}_1$  axis, considering this symmetry criterion.

For the application of the reconnection search algorithm to the jet in this work, we have used a modified version of the algorithm developed by Kadowaki et al. (2018b) in order to include the relativistic effects. Equations 2.20 and 2.21 are applied in the coordinate frame (here called the jet frame). We have also introduced the reconnection comoving frame to evaluate quantitatively the reconnection events since each local cell can move relative to the jet frame with relativistic velocities. Therefore, we transformed

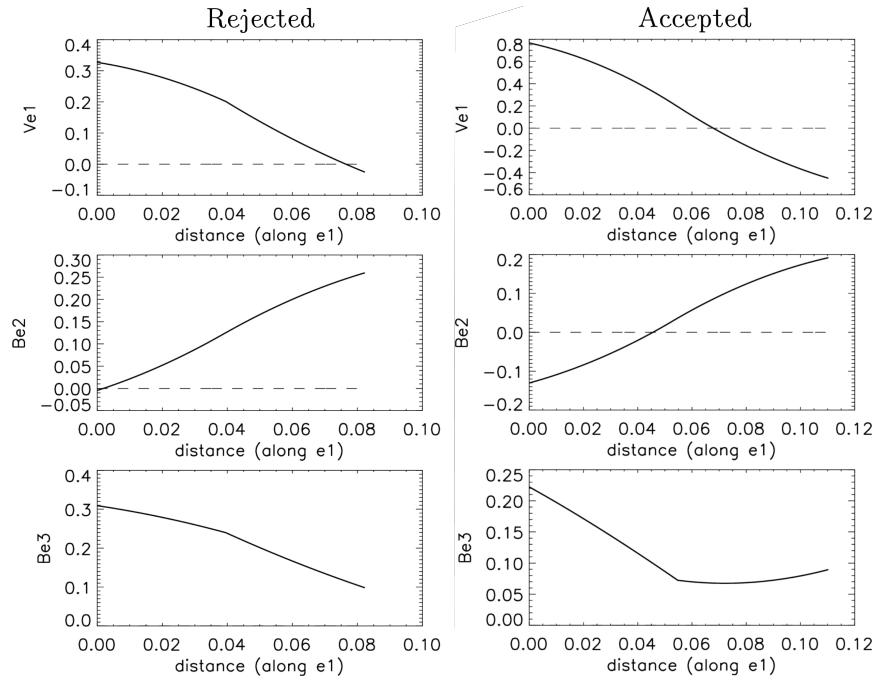


Figure 2.4: Sample of profiles rejected and accepted, following the criteria of the most symmetric magnetic and velocity field profiles (Kadowaki et al., 2018b).

all the variables inside each subarray data cube from the jet to the reconnection frame, via generalized Lorentz transformations. We have also implemented another criterion to constrain a reconnection region, where at least one of the edge velocities (left or right in  $\hat{\mathbf{e}}_2$ , see Figure 2.3) has to be directed to outside of the reconnect region. This allows for the removal of sites with positive velocities at the left edge and negative at the right edge, which are not real reconnection regions because in such cases the plasma is moving back into the diffusion region instead of going out.

This algorithm is able to perform a systematic search of all reconnection events in the system, allowing for visualization of the local magnetic topology of the current sheets, as well as quantification of the reconnection rate and the magnetic power released in these events, in three different frames (the reconnection, the jet, and the observer's frame).

## 2.3 Simulation of test particle acceleration by magnetic reconnection in relativistic jets

After simulating the evolution of the relativistic jet subject to the CDKI and the development of magnetic reconnection regions, and after the identification of these reconnection regions and their characteristic velocities of reconnection, we inject thousands of test particles in different snapshots. We then integrate the trajectories of the particles within the jet domain using the **GACCEL** code (developed by Grzegorz Kowal, see Kowal et al., 2011, 2012; del Valle et al., 2016) which solves the equation of motion for each charged particle

$$\frac{d(\gamma m \mathbf{u})}{dt} = q(\mathbf{E} + \frac{\mathbf{u}}{c} \times \mathbf{B}), \quad (2.24)$$

where  $\gamma \equiv (1 - u^2/c^2)^{-1/2}$  is the particle Lorentz factor,  $c$  is the speed of light,  $\mathbf{u}$ ,  $m$  and  $q$  are the particle velocity, mass and electric charge, respectively. The electric field is generated by both the background flow of magnetized plasma and by magnetic resistivity effects, and can be obtained directly from the Ohm's law equation

$$\mathbf{E} = -\frac{\mathbf{v}}{c} \times \mathbf{B} + \eta \mathbf{J}, \quad (2.25)$$

where  $\mathbf{v}$  is the plasma velocity,  $\mathbf{J}$  is the current density and  $\eta$  is the Ohmic resistivity coefficient. Since in our studies we are not interested in the acceleration of particles by the electric field resulting from resistivity effects, but in the acceleration provided by the plasma magnetic fluctuations, we neglected the term  $\eta \mathbf{J}$ . We note that, this term can be important only in the initial phases of the particle acceleration in the reconnection regions, but it is soon dominated by the first term, once the particles Larmor radius becomes as large as the size of the magnetic fluctuations (e.g., Kowal et al., 2011, 2012). Substituting the Ohm's law, the equation of motion (2.24) is

$$\frac{d}{dt}(\gamma m \mathbf{u}) = q[(\mathbf{u} - \mathbf{v}) \times \mathbf{B}]. \quad (2.26)$$

In the current study, we do not include particle radiative losses or their feedback on the background plasma, therefore test particles can gain or lose energy only through the interactions with the moving magnetized plasma and its fluctuations. The particle equation of motion (2.26) was integrated using the fourth-order Runge-Kutta method and the interpolation of the local values of the plasma velocity  $\mathbf{v}$  and magnetic field  $\mathbf{B}$  at each step of the integration has been done using linear interpolation of the values from the discrete grid of the MHD simulation domain. We integrated the equation (2.26) for 100 to 10,000 protons with a randomly chosen initial position in the domain and direction of motion, with an initial Maxwell distribution of the velocity corresponding to

a temperature of  $10^{10}K$  (non-relativistic particles) and mean kinetic energy of the order of 1 MeV ( $\sim 10^{-3}m_p c^2$ , where  $m_p$  is the proton mass) for the majority of cases. Only in one of the models investigated, we assume an initial monoenergetic distribution (see Chapter 3).

In order to check potential boundary effects, the trajectories of the particles were integrated considering the background domain with two different boundary conditions: periodic in all directions, and periodic in the  $z$  direction and outflow in the  $x$  &  $y$  directions, this latter as in the simulated MHD background. In the first case, the particles may be reinjected in the domain whenever they escape in any direction, while in the second case, they return to the environment only if they escape in the  $z$  direction. The results, as we will see in Section 3.2.1, are very similar in both cases, but the first implies much longer computing time. Also, we have found that the results are very similar whether we inject the particles in a specific region of the jet with a large concentration of reconnection sites or in the entire jet because the particles can propagate in the whole box.

As we have described in section 2.1, the background jet simulation is performed in code units (c.u.), dimensionless equations, but in order to integrate the trajectories of the particles in the **GACCEL** code, we need to convert the background conditions in physical units. The adopted time unit is one hour, the velocity unit is the light speed  $c$ . This implies that  $L = 1.1 \times 10^{14}$  cm or  $3.5 \times 10^{-5}$  pc. For the magnetic field we adopt two possible values that correspond to the initial magnetic field in the jet axis,  $B_0 = 0.094$  and 9.4 G. These values come from converting the code unit for the magnetic field strength,  $B_0 = 0.7$  c.u., or  $B_0 = 0.7\sqrt{4\pi\rho_0 c^2}$ , assuming  $\rho_0 = 1.0 \text{ cm}^{-3}$  and  $10^4 \text{ cm}^{-3}$ , respectively.

We note that in the particle framework, the dynamical length scales are settled by their Larmour radius

$$r_L = \frac{\gamma m c^2}{q|\mathbf{B}|}. \quad (2.27)$$

In order for the particle eventually, to be able to interact resonantly with the background plasma magnetic fluctuations, the Larmour radius has to be of the order of the size of these fluctuations.

For the analysis of our results it is important to compute the acceleration rate of the particles, which is defined as,

$$t_{acc}^{-1} = \frac{dE/dt}{E}. \quad (2.28)$$

In order to compute the mean acceleration time  $t_{acc}$  of the test particles as a function of energy, we calculated the acceleration time of each particle in a bin of kinetic energy between  $E$  and  $E + \Delta E$

$$t_{acc} = \sum_{i=1}^{N_E} \frac{t_i}{N_E}, \quad (2.29)$$

where  $t_i$  is the acceleration time of particle  $i$  and  $N_E$  is the number of particles with

energy between  $E$  and  $E + \Delta E$ . The corresponding standard deviation is

$$\sigma^2 = \sum_{i=1}^{N_E} \frac{(t_{acc} - \bar{t})^2}{N_E - 1}, \quad (2.30)$$

where  $\bar{t}$  is the mean value of  $t_i$  for all the particles with energy between  $E$  and  $E + \Delta E$ . We will see in Chapter 3 the kinetic energy undergoes a regime of exponential growth. Thus we can describe it as a power-law energy dependence of the time,

$$\log E = s \log t + b, \quad (2.31)$$

$$E = 10^{bt^s}, \quad (2.32)$$

where  $s$  is the slope of the fitting and  $b$  is the intersection of the line with  $\log E$  axis. From (2.28) and (2.32)

$$t_{acc}^{-1} = \frac{s10^{bt^{s-1}}}{10^{bt^s}}, \quad (2.33)$$

$$t_{acc}^{-1} = st^{-1}, \quad (2.34)$$

$$t_{acc}^{-1} = s10^{-b/s} E^{-1/s}. \quad (2.35)$$

Therefore, the acceleration time is

$$t_{acc} \propto E^{1/s}, \quad (2.36)$$

or

$$t_{acc} \propto E^\alpha, \quad (2.37)$$

where  $\alpha$  is the acceleration time index. From (2.37), we can obtain  $\alpha$  as,

$$\alpha = \frac{\Delta \log(t_{acc})}{\Delta \log(E)}. \quad (2.38)$$

In the next Chapter we will present the results of this work based on the employment of the numerical techniques described above.

# Chapter 3

## Results

In this chapter, we present the results of our study on the acceleration of particles (protons) injected in a three-dimensional special relativistic magnetohydrodynamical (SRMHD) jet subject to current-driven kink instability (CDKI), which drives turbulence and fast magnetic reconnection. First, we show the results of our three-dimensional SRMHD simulations of the Poynting Flux dominated tower jet subject to CDKI, as described in Section 2.1 of Chapter 2. Then, we show the results of the application of the reconnection search algorithm to the simulated jet, as described in section 2.2 of Chapter 2. Finally, we present the results of the acceleration of test particles in this domain in different snapshots along the jet evolution, using the method described in Section 2.3 of Chapter 2. We remark that most of our test particle study has been done using the background model *j240*, see Table 2.1. The higher resolution model *j480* was performed in order to test the convergence of the SRMHD results. We will see later on in Section 3.2.3, that these convergence tests were well succeeded, and for this reason, we have considered model *j240* for most of the acceleration analyses.

### 3.1 3D MHD simulation of the relativistic tower jet

Figure 3.1 shows the time evolution of the relativistic jet model *j240* (see Table 2.1) for snapshots at  $t = 25, 30, 40, 44, 46,$  and  $50 L/c$ . It depicts, in color scales, the isosurface of the magnetic current density intensity at half maximum in orange and the density map of the jet central slice (at the plane  $z$ - $y$ , and  $x = 0$ ), as well as the magnetic field lines in black. As time evolves and the CDKI grows, the jet spine becomes increasingly deformed and disruptive, driving turbulence and magnetic reconnection.

In the next section we describe in detail the development of these reconnection events.

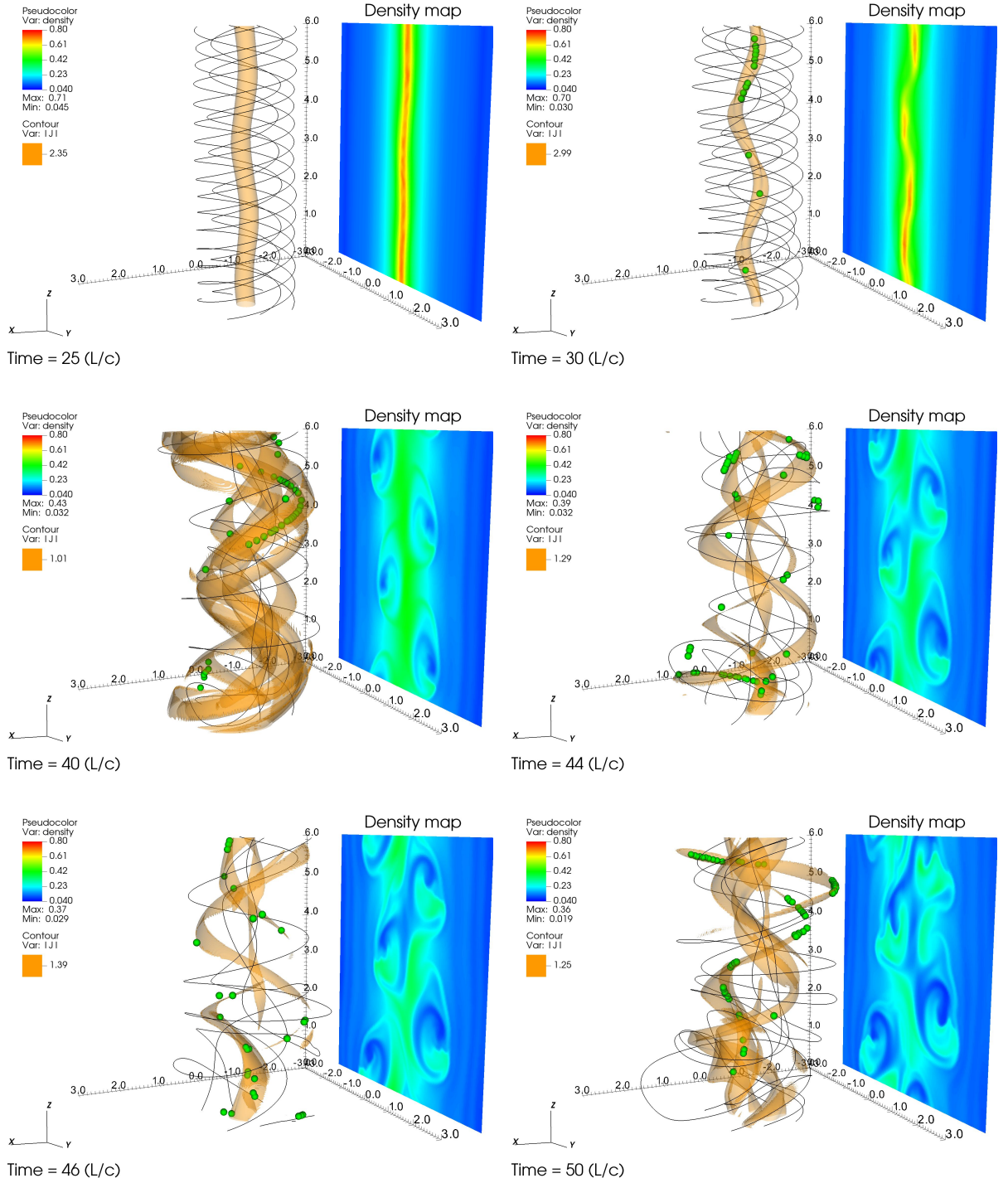


Figure 3.1: Time evolution of the tower jet at  $t = 25, 30, 40, 44, 46$  and  $50 L/c$  (from top left to bottom right). The diagrams depict isosurfaces of the current density intensity at half maximum  $|J|$  (orange color), the solid black lines correspond to the magnetic field lines, and the green circles correspond to the position of fast magnetic reconnection regions (with velocities larger than or equal to the average reconnection speed) identified with the algorithm described in Section 2.2. At  $z$ - $y$  plane, it is shown the density map of the central slice of the jet (at  $x = 0$ ). The time  $t$  is in units of  $L/c$ , the density in units of  $\rho_0$ , and the current density is also in code units.

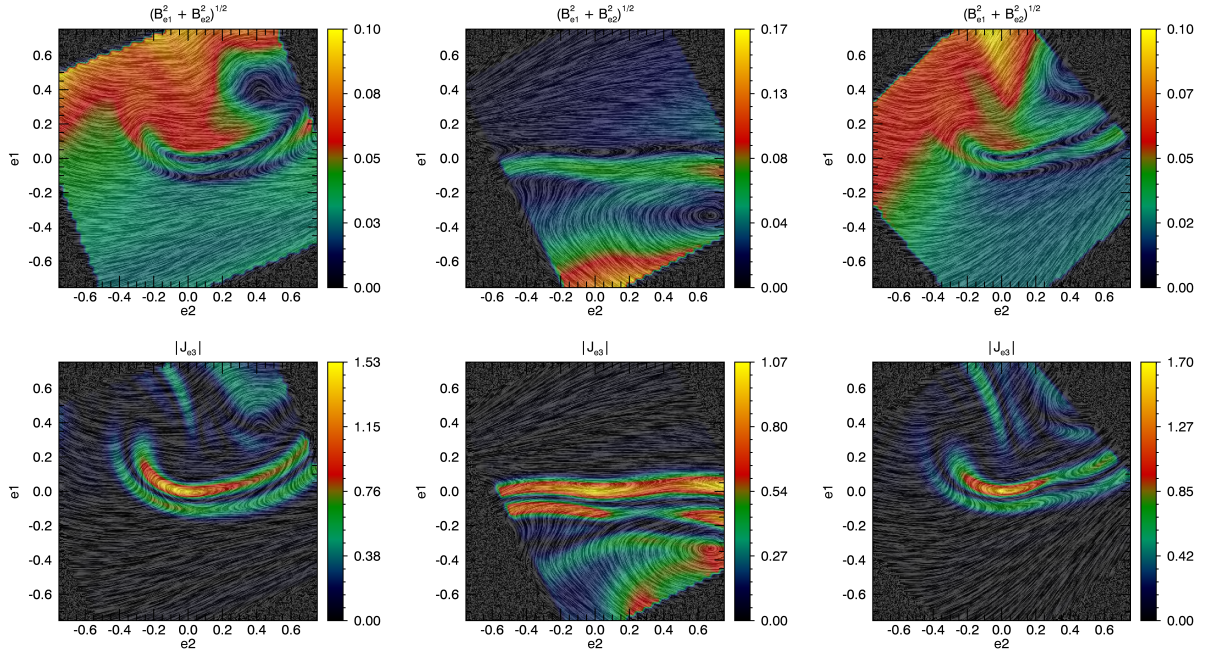


Figure 3.2: Diagrams of three magnetic reconnection sites in the jet frame, selected from snapshot  $t = 50L/c$ . The diagrams were produced by a line integral convolution (LIC) method combined with the 2D projection of the magnetic field (top diagrams) and current density (bottom diagrams) magnitudes in the  $\hat{e}_1$ - $\hat{e}_2$  plane.

### 3.1.1 Identification of current sheets in our simulations

The resolution of our simulated jet is large enough to allow us to follow the growth of the turbulence and disentangle the reconnection structures. We used the algorithm described in Section 2.2 of Chapter 2 (Kadowaki et al., 2018b; ?) to identify sites of fast reconnection in our simulations of the relativistic jet. We used the parameters values  $\epsilon$  (associated to the threshold current density, see equation (2.20)) and  $b$  (which corresponds to the minimum value for the current sheet, see equation (2.21)) equal to 5 and 0.1, respectively. At each potential reconnection site, we determine a cubic subarray size of  $3 \times 3 \times 3$  cells. This means, the current sheets (Figure 2.3 right) for our jet have been defined by the cells with  $|\mathbf{J}| > 0.1 |\mathbf{J}_{max}|$ , because unlike the study in the shear box (Kadowaki et al., 2018b), in the jet not so many reconnection regions were identified. As selection criteria, we consider only the opposite sign of the magnetic field and the reconnection speeds, without considering the symmetry of the profiles, or the criteria of the outflow velocity, as explained in Section 2.2. Since each local maximum cell can move relative to the jet frame with relativistic velocities, we have introduced the reconnection comoving frame, to evaluate quantitatively the reconnection events, then, we transformed all the variables from the jet to the reconnection frame, via generalized Lorentz transformations (see Section 2.2).

In order to verify how reconnection events can behave along with the relativistic jet, we

have selected a sample of sites identified as magnetic reconnection structures by the search algorithm. Figure 3.2 shows the  $2D$  maps of three such sites in the jet frame, selected at  $t = 50 L/c$  snapshot. These have been produced using the line integral convolution (LIC) method (Cabral and Leedom, 1993) to represent, at the same diagram, the magnetic streamlines, and the magnetic field (top diagrams), and current density (bottom diagrams) magnitudes. The diagrams correspond to an arbitrary slice in the  $\hat{e}_1$ - $\hat{e}_2$  plane (the local coordinate system at the jet frame, see section 2.2), and they were obtained by a cubic interpolation of the data, for visualization purposes. The bottom diagrams of Figure 3.2 show the high concentration of the magnetic field around the reconnection sheets. The column on the left shows an elongated “bow-shaped” magnetic island with an X-point-like structure right below, whereas the middle diagrams show a complex topology with at least three magnetic islands. The right column shows similar behavior with two islands (already reconnected) separated by an X-point-like structure, and accumulated magnetic field lines (in reconnection) below them. The diagrams show clearly the anti-correlation between the magnetic field and the current density, as we should expect for reconnection events. This study is useful to follow the time evolution of these structures since each example may represent reconnection events in different stages. Moreover, such analysis allows us to identify false-positives events in our sample (i.e., regions identified by the search algorithm that are actually not associated with reconnection events). However, for a complete analysis, it would be necessary to check about 200 sites per snapshot separately in a total of  $\sim 660$  snapshots for model j240, but that is out of the scope of the present study.

In spite of the information provided by Figure 3.2, the  $2D$  projection of the magnetic field components is not enough to reveal the complex  $3D$  topology of a reconnection event. Furthermore,  $3D$  reconnection does not always imply that the three components of the magnetic field are annihilating at a time as we see in this work in most cases, where only one of the components of the magnetic field is annihilated (see also, e.g., Priest et al., 2003; Parnell et al., 2010; Yamada et al., 2010; Pontin et al., 2011, and references therein). Figure 3.3 shows a sample of identified reconnection sites (green and black circles in the top diagram) in the jet frame, at  $t = 50L/c$ . The top diagram shows a zoom-in plot of the magnetic field streamlines (black and magenta lines). The colored arrows represent the axes  $\hat{e}_1$ ,  $\hat{e}_2$ , and  $\hat{e}_3$  (yellow, blue, and red, respectively) of the local coordinate system, the orange isosurface corresponds to the associated current sheet with half of the maximum value of  $|J|$  at the primary reconnection site (green circle), and the black circles correspond to secondary reconnection events. The black lines represent the asymptotic (non-reconnected) magnetic field far away from the diffusion region, whereas the magenta lines represent the twisted and braided magnetic field lines that produce a thin and strong current density isosurface with the maximum value at the green circle’s position. As we expected, the  $\hat{e}_1$ -axis is perpendicular to the current sheet, whereas the

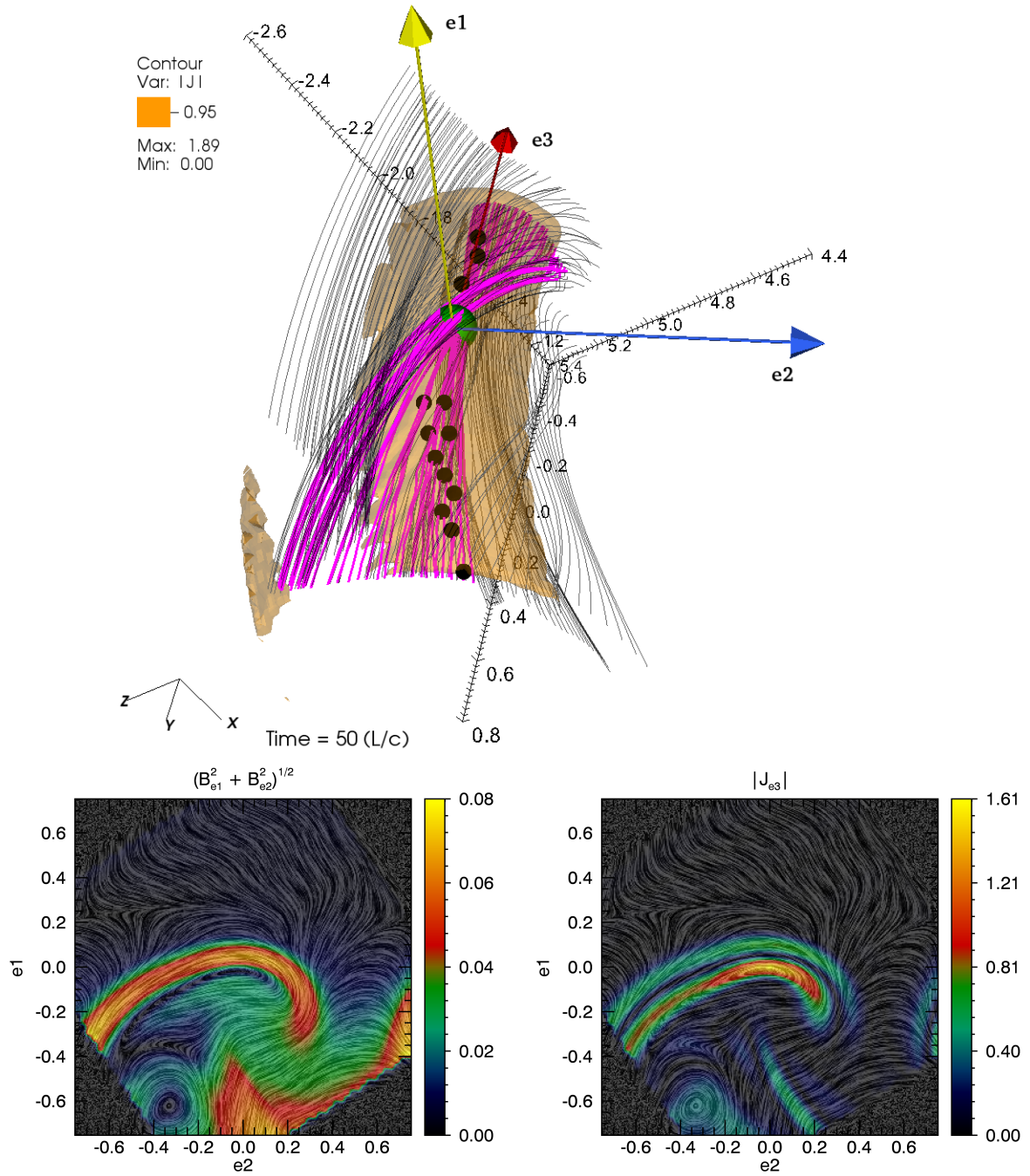


Figure 3.3: The top diagram shows a zoom-in plot of the magnetic field streamlines (black and magenta lines) around a sample of identified reconnection sites (green and black circles), at  $t = 50L/c$ , in the jet frame. The colored arrows represent the axes of the local coordinate system, and the orange isosurface corresponds to the associated current sheet with half of the maximum value of  $|J|$  at the primary reconnection site (green circle). The bottom diagrams show the corresponding 2D LIC maps (as in Figure 3.2).

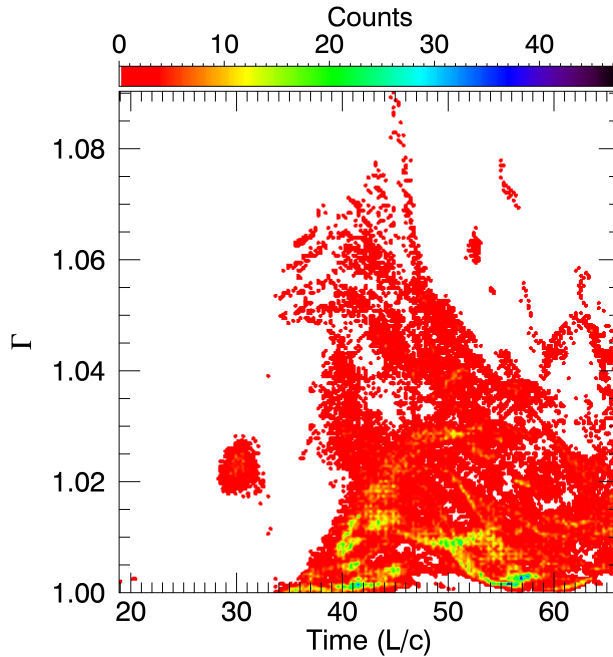


Figure 3.4: Time-distribution of the Lorentz factor ( $\Gamma$ ) of the diffusion regions with respect to the jet frame, for the model j240. The histogram corresponds to Lorentz factors obtained during the entire evolution of the simulation (with 200 bins in each direction).

$\hat{e}_2$ - $\hat{e}_3$  plane is aligned it. The  $\hat{e}_3$  axis matches the direction of the local magnetic guide field, proving the efficiency of the algorithm in separating the dominant non-reconnected magnetic component from those in reconnection.

Finally, the  $2D$  LIC maps at the bottom of Figure 3.3 show the magnetic (left panel) and current density magnitudes (right panel) around the primary reconnection site, green circle in the top diagram. Both maps show a magnetic island topology as a result of the projection of the reconnected components in the  $\hat{e}_1$ - $\hat{e}_2$  plane. The local magnetic guide field is still present but hidden by the projection. Therefore, despite the useful information obtained from these  $2D$  maps, the overall  $3D$  scenario and the real nature of the magnetic islands, which are  $2D$  projections of reconnected flux tubes (Kowal et al., 2011), should be analyzed carefully. This discussion is important since the formation of current sheets along the jet due to reconnection events is expected (see, e.g., Giannios et al., 2009; Christie et al., 2019), but the real magnetic topology will be more complex than island-like or plasmoid structures (Singh et al., 2016).

Figure 3.4 shows that the time-distribution of the Lorentz factor ( $\Gamma$ ) in the diffusion regions, which has a maximum value of 1.09 at  $\sim 45 L/c$ . Thus although we have used the Lorentz transformation to obtain the velocity profiles around the diffusion region in the reconnection reference frame, such correction will not change significantly with respect to the Galilean transformation. Therefore, the velocities of the reconnection sites are mildly relativistic at the jet frame, with Lorentz factors of the order of unity.

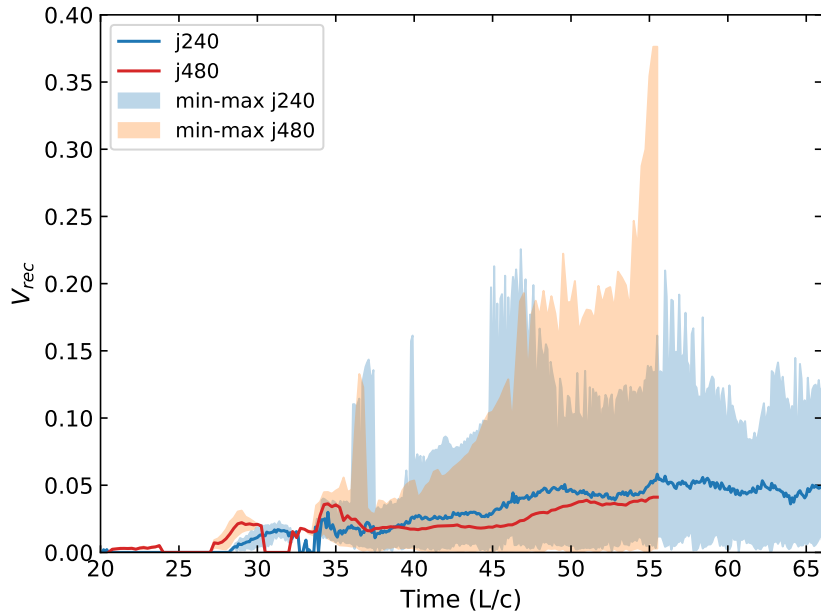


Figure 3.5: Time evolution in code units of the reconnection velocity in the tower jet for the two resolutions investigated in this work. It includes to the whole sample of reconnection regions (with symmetric and nonsymmetric profiles). The time  $t$  is in units of  $L/c$ . The shaded light blue and red colors give the entire distribution of reconnection velocities from maximum to minimum values for the two jet models, j240 and j480, respectively. The blue and red lines give the corresponding average reconnection speeds,  $\langle V_{rec} \rangle$ , for each model (over all identified sites in each snapshot).

Figure 3.5 presents the evolution of the mean reconnection velocity, equation 2.23 (normalized by the total local Alfvén velocity, equation 2.17), in the jet obtained from the computation of the reconnection velocity in each identified current sheet employing the search algorithm (Kadowaki et al., 2018b). It compares also the time evolution of the average reconnection rate obtained for the reference jet model with resolution of  $240^3$  cells (model j240, blue line), with the higher resolution model  $480^3$  (model j480, red line) cells, indicating that they are both similar.

In Figure 3.1, the green dots characterize all sites of *fast* reconnection (identified with the search algorithm), that is, with reconnection velocities larger than or equal to the average reconnection rate obtained for each snapshot. Table 3.1 presents this average and the maximum reconnection velocity values for each of the snapshots of Figure 3.1 (in units of local Alfvén speed), as well as the number of reconnection sites (or counts) with reconnection velocities larger than the average value.

We note that in  $t = 25 L/c$ , there are no green dots (or reconnection regions), because turbulence and fast reconnection is driven by the CDKI have not developed yet, but in  $t = 30 L/c$ , we identify already the break of symmetry of the plasma column and the appearance of a few fast reconnection sites at the jet axis. We find that until near  $t = 40 L/c$ , there are still very few sites of fast reconnection, but in this snapshot and

Table 3.1: Reconnection velocity values in units of the local Alfvén speed in j240.

Jet snapshot	$\langle V_{rec} \rangle$	$max(V_{rec})$	Total counts	Counts ( $V_{rec} \geq \langle V_{rec} \rangle$ )
25	0	0	0	0
30	0.01	0.02	25	11 (44%)
40	0.03	0.06	130	55 (42%)
44	0.03	0.1	161	58 (36%)
46	0.04	0.2	121	39 (32%)
50	0.05	0.1	136	66 (49%)

beyond, there are several sites spread over all the jet domain, as we see in  $t = 44, 46,$  and  $50 L/c$ , in Figure 3.1. It is interesting that in the snapshot  $t = 40 L/c$ , though it presents several sites, their reconnection velocities are all around the average (see values of  $\langle V_{rec} \rangle$  and  $max(V_{rec})$  in table 3.1), contrary to what we see in the more evolved snapshots where there are sites with very high reconnection speeds.

### 3.1.2 Development of current driven kink instability (CDKI)

As an indicator of the growth of the CDKI in Figure 3.6 we show the time evolution of the volume-averaged kinetic energy transverse to the z-axis within a cylinder of radius  $R/L \leq 3.0$  around the jet axis (Mizuno et al., 2009, 2011, 2012; Singh et al., 2016),

$$E_{k,xy} = \frac{1}{V_b} \int_{V_b} \frac{\rho v_x^2 + \rho v_y^2}{2} dx dy dz. \quad (3.1)$$

The difference between this energy value and the initial energy value (at  $t = 0$ ) indicates the radial motion induced by the growth of CDKI and this difference is depicted in the left panel of Figure 3.6. The volume-averaged total relativistic electromagnetic energy

$$E_{em} = \frac{1}{V_b} \int_{V_b} \frac{\mathbf{B}^2 + [\mathbf{v}^2 \mathbf{B}^2 - (\mathbf{v} \cdot \mathbf{B})^2]}{2} dx dy dz, \quad (3.2)$$

where  $V_b$  is the total volume where the average is calculated (see right panel of Figure 3.6).

As in Mizuno et al. (2012) and Singh et al. (2016), we can use the diagrams of the energy density evolution to quantify the growth of the CDKI. As it develops, electromagnetic energy is converted into kinetic energy and this is a striking feature revealed by Figure 3.6. Note that in this Figure, the electromagnetic energy is presented on a linear scale, while the kinetic energy is on a log scale. The initial relaxation of the system to equilibrium leads to a hump in the kinetic and electromagnetic energy density curve (until  $\sim 10 L/c$ ). Though the centrifugal and pressure forces of our initial setup are small, they are not entirely negligible and thus the initial force-free magnetic configuration is not in

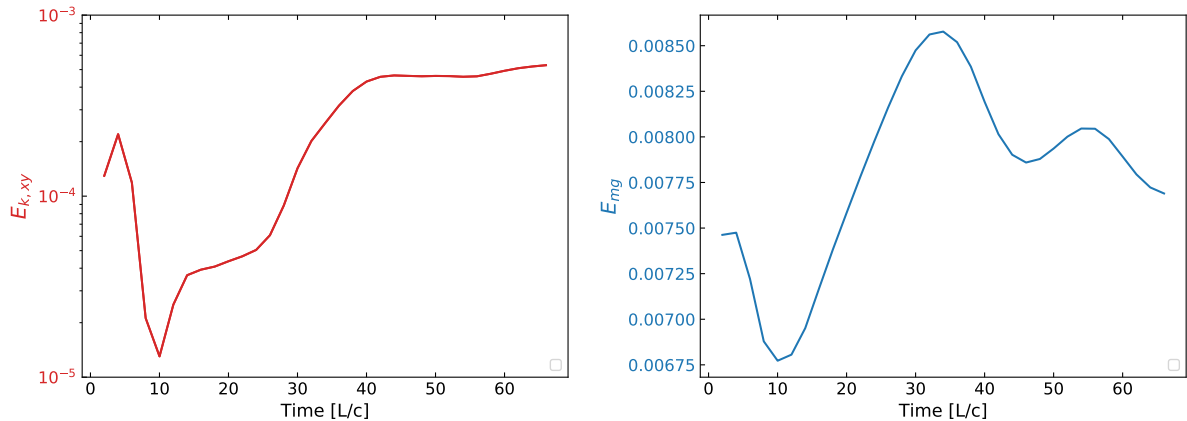


Figure 3.6: Volume-averaged energy time evolution within a cylinder of radius  $R/L \leq 3.0$  for the simulation. In red: kinetic energy transverse to the z-axis. In blue: total electromagnetic energy. The kinetic energy density is in log scale, while the electromagnetic energy density is in linear scale.

real equilibrium. Therefore, a little relaxation occurs after a few times steps. The kink instability comes into play only after the relaxation finishes. There is an initial linear growth of the electromagnetic energy between 10 and  $\sim 30 L/c$  due to the increasing wiggling distortion of the magnetic field structure in the jet spine in the initial increase of the CDKI (which in a log scale would be harder to perceive; see e.g. Mizuno et al., 2012). After a slower increase, the kinetic energy undergoes an exponential growth from  $t \sim 30 L/c$  to a maximum near  $t \sim 40 L/c$ , after which it approximately reaches a plateau while the magnetic energy decreases (see more details in Singh et al., 2016). We note that this plateau time also coincides with the one after which we have detected an increase in the turbulence and the number of fast reconnection sites in Figure 3.1. This plateau regime characterizes the achievement of non-linear saturation of the CDKI and a nearly steady-state turbulent regime in the system.

If we go back to Figure 3.5 and take a closer look, we see that after the time  $t \sim 40L/c$ , i.e. when the CDKI reaches the plateau, both resolution models have some variability in the peak of the reconnection speed attaining values as large as 0.23 and 0.38 for the model j240 and 480, respectively. But average reconnections rates are similar and *fast* during the nearly stationary turbulent regime for both models. The fact that these maximum reconnection rates are achieved after the CDKI reaches saturation and the kinetic energy increases in the system is clear evidence that fast magnetic reconnection is being driven by this instability.

The absence of significant differences between the two resolution models of Figure 3.5 are also compatible with the fact that fast magnetic reconnection driven by turbulence is independent of the numerical resistivity (as obtained by Kowal et al., 2009, 2012; Kadwaki et al., 2018b). This is in agreement with the turbulence-induced fast reconnection theory of Lazarian and Vishniac (1999), which predicts that the turbulence speeds up the

reconnection independently of the Ohmic resistivity of the environment.

In the next section, we extend a little more upon the analysis of the distribution of the reconnection sites.

### 3.1.3 Distribution of the Magnetic Reconnection Velocities

Figure 3.7 shows different histograms of the magnetic reconnection rate ( $V_{rec}$ ), for the model j240. The left diagrams correspond to time-distributions obtained during the entire evolution of the simulation (with 200 bins in each direction), and the right diagrams correspond to 1D-distributions obtained between 50 and  $66L/c$  time steps (with 140 bins), when the system is already in a quasi-steady turbulent regime (see also Section 3.1.2). The left top diagram shows, also, sporadic and slow reconnection events with values  $V_{rec} < 0.01$  around  $t = 20L/c$ . These events should be analyzed carefully because at this time the CDKI is still growing and possibly they are not real reconnection layers. However, they are not significant, as we will see later since the inferred reconnection speeds are very low. Furthermore, we note that there is a lack of events, especially between 33 and 34  $L/c$ , this may be happening because, at these times the CDKI is still growing, and the magnetic field is getting distorted, but with almost no disruption. After  $t \sim 35L/c$ , the number of events and the value of  $V_{rec}$  increase as the system reaches the saturation of the exponential growth of the kink instability (see Table 3.1 and Section 3.1.2), with the fastest rate of  $V_{rec} \sim 0.23$  (at  $t = 56L/c$ ).

The right top histogram shows that the distribution of  $V_{rec}$  does not resemble a normal distribution, showing a long tail on the side of the fastest rates (similar to the results obtained by Kadowaki et al., 2018b, for non-relativistic accretion disk systems). This skewed feature is characteristic of a log-normal distribution, and to test this hypothesis we have performed fits (black lines in the right histograms). We also constrained the sample in order to obtain the reconnection rate only for the most symmetric profiles (bottom histograms of Figure 3.7), we obtained from the fit of the constrained sample an average reconnection rate of the order of  $0.050 \pm 0.021$ , which does not differ from the value of the original sample ( $\langle V_{rec} \rangle = 0.051 \pm 0.026$ ). Furthermore, this value is compatible with that found in Singh et al. (2016). We note that the log-normal distribution is characteristic of a turbulent flow, thus being additional evidence that the turbulence induced by the CDKI (section 3.1.2), is driving the fast reconnection events (in agreement with the theory of Lazarian and Vishniac, 1999) (see also Santos-Lima et al., 2010; Kadowaki et al., 2018b) along the relativistic jet.

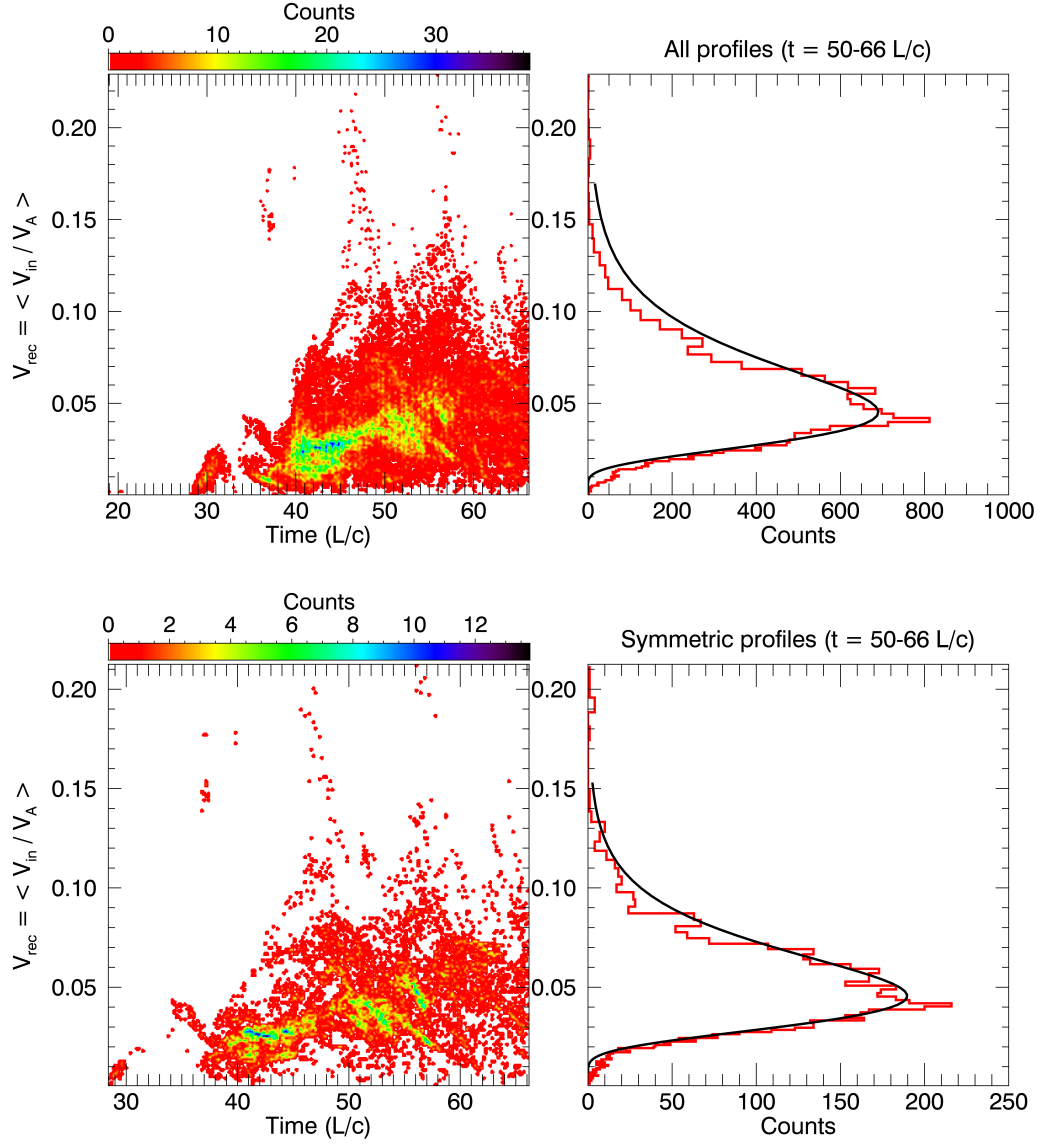


Figure 3.7: Histograms of the reconnection rate  $V_{rec}$  for the model j240. The left diagrams correspond to time-distributions obtained during the entire evolution of the simulation (with 200 bins in each direction), and the right diagrams correspond to  $1D$ -distributions (red lines) with a log-normal fit (black lines) obtained between the snapshots 50 and  $66L/c$  (with 140 bins). The top distributions correspond to the whole sample, and the bottom ones correspond to a constrained sample considering only the most symmetric profiles of the velocity and magnetic fields at the edge of the diffusion regions.

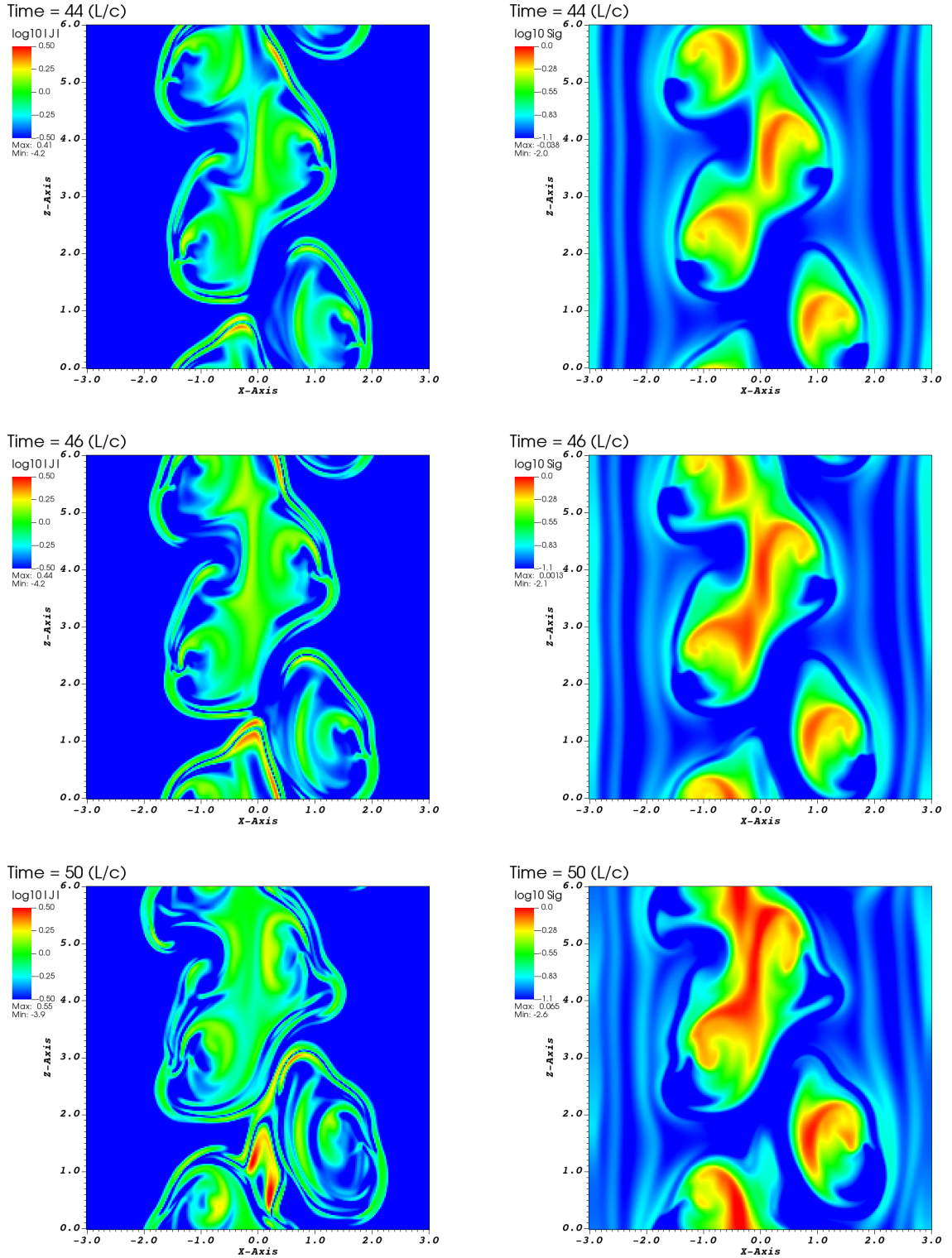


Figure 3.8: Two-dimensional cuts in the  $x - z$  plane at  $y = 0$ , in logarithm scale of the current density  $\nabla \times \mathbf{B}$  (left panels), and magnetization parameter  $\sigma = B^2/\gamma^2 \rho h$  (right panels) at  $t = 44, 46$  and  $50 L/c$  (from top to bottom). The time  $t$  is in units of  $L/c$ .

### 3.1.4 Magnetization parameter and Current sheet

As stressed before, regions where magnetic reconnection occurs are regions of enhanced current densities, due to the abrupt change of direction of the magnetic field. Therefore, regions of large current densities are where magnetic reconnection is possibly occurring. The magnetic discontinuities (current sheets) obviously are also characterized by a sharp decrease in the magnetization parameter. This implies, as stressed many times before, that magnetic reconnection regions are sites of maximum energy dissipation, which can contribute to the increase in kinetic energy of the relativistic tower jet and also allow for efficient particle acceleration (de Gouveia Dal Pino and Lazarian, 2005).

Figure 3.8 shows two-dimensional slices in the plane  $x$ - $z$  at  $y = 0$ , of the logarithmic distribution of the current density intensity ( $\nabla \times \mathbf{B}$ ) and the magnetization parameter  $\sigma = B^2/\gamma^2\rho h$  for the model  $j240$  at  $t = 44, 46,$  and  $50 L/c$ . This Figure is complementary to Figure 3.1, as it provides additional information specially for the magnetization parameter evolution. Comparing the current density with the magnetization parameter diagrams, we see that regions with large intensity values of current density, especially in the bottom of the slices for the three different snapshots, coincide with regions where the magnetization parameter is small. For  $t = 44 L/c$  this anti-correlation happens especially in the region for  $z$  between  $5.1$  e  $5.6 L$  and between  $0.7$  and  $0.9 L$ , and intensifies in the later snapshots.

Comparing with Figure 3.1, we see that these coincide with regions of fast reconnection in the jet axis and thus are appropriate for particle acceleration. In fact, these regions can be seen quite populated by particles undergoing acceleration in the two-dimensional histogram of the position of the particles in Figure 3.9 (see Section 3.2), especially for  $t = 46$  and  $50 L/c$ . We also note that the magnetization reaches maximum values around unity in these more evolved times ( $t = 44, 46$  and  $50 L/c$ ).

## 3.2 Particle acceleration

We have injected test particles in different snapshots of the SRMHD jet model  $j240$ , specifically, in the simulation times  $t = 25, 30, 40, 44, 46,$  and  $50 L/c$  (see also Figure 3.1). Table 3.2 shows the parameters for each test particle model used in the **GACCEL** code. "Jet snap" corresponds to the time of the jet snapshot in units  $L/c$ , "N" is the number of injected test particles, " $B_0$ " is the value of the initial magnetic field in the jet axis in Gauss unit. As stressed in Section 2.3, in order to check potential boundary effects, the trajectories of the particles are integrated considering two different boundary conditions, periodic in all directions (test particle model names ending with "p" in Table 3.2), or periodic in the  $z$  direction only with outflow boundaries in the  $x$  &  $y$  directions (test particle model names ending with "o" in Table 3.2) as in the simulated MHD background

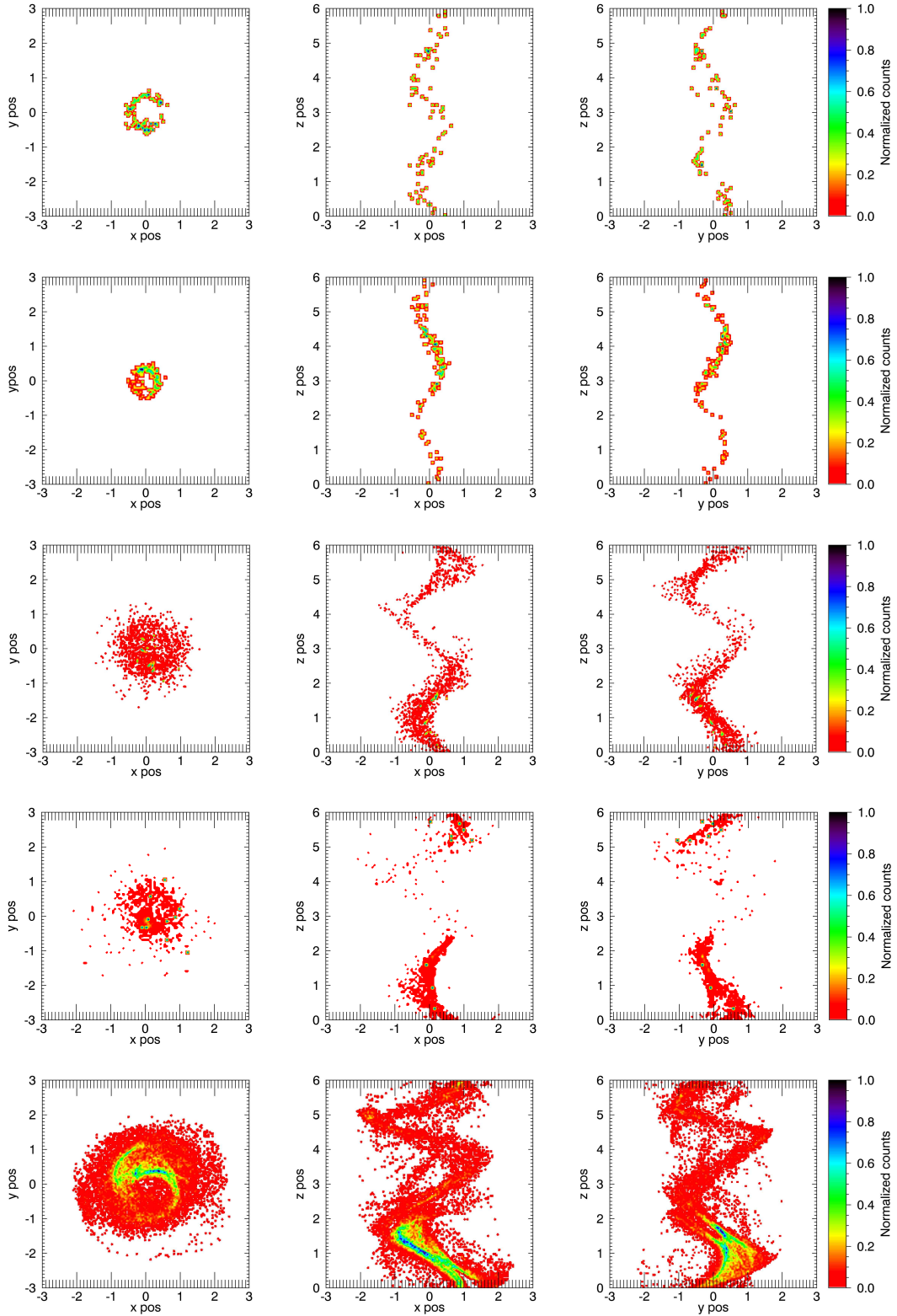


Figure 3.9: Two-dimensional histograms of particle positions for different snapshots of the model  $j240$ . From top to bottom,  $t = 25 L/c$  ( $ut25o$ ),  $t = 30 L/c$  ( $t30o$ ),  $t = 44 L/c$  ( $t44o$ ),  $t = 46 L/c$  ( $t46o$ ), and  $t = 50 L/c$  ( $t50o$ ), respectively. Each row, from left to right, shows histograms projected on  $xy$ ,  $xz$ , and  $yz$  plans. To make visualization more clear, the histograms depict only particles accelerating with increment  $\Delta E_p/E_p > 0.4$ , and with energies larger than  $10^2$  MeV ( $\sim 10^{-1}m_p c^2$ ), except for  $t = 25 L/c$ , for which the minimum energy depicted is  $10^4$  MeV. The different colors indicate the (normalized) concentration of particles in each region of the jet (see text for details).

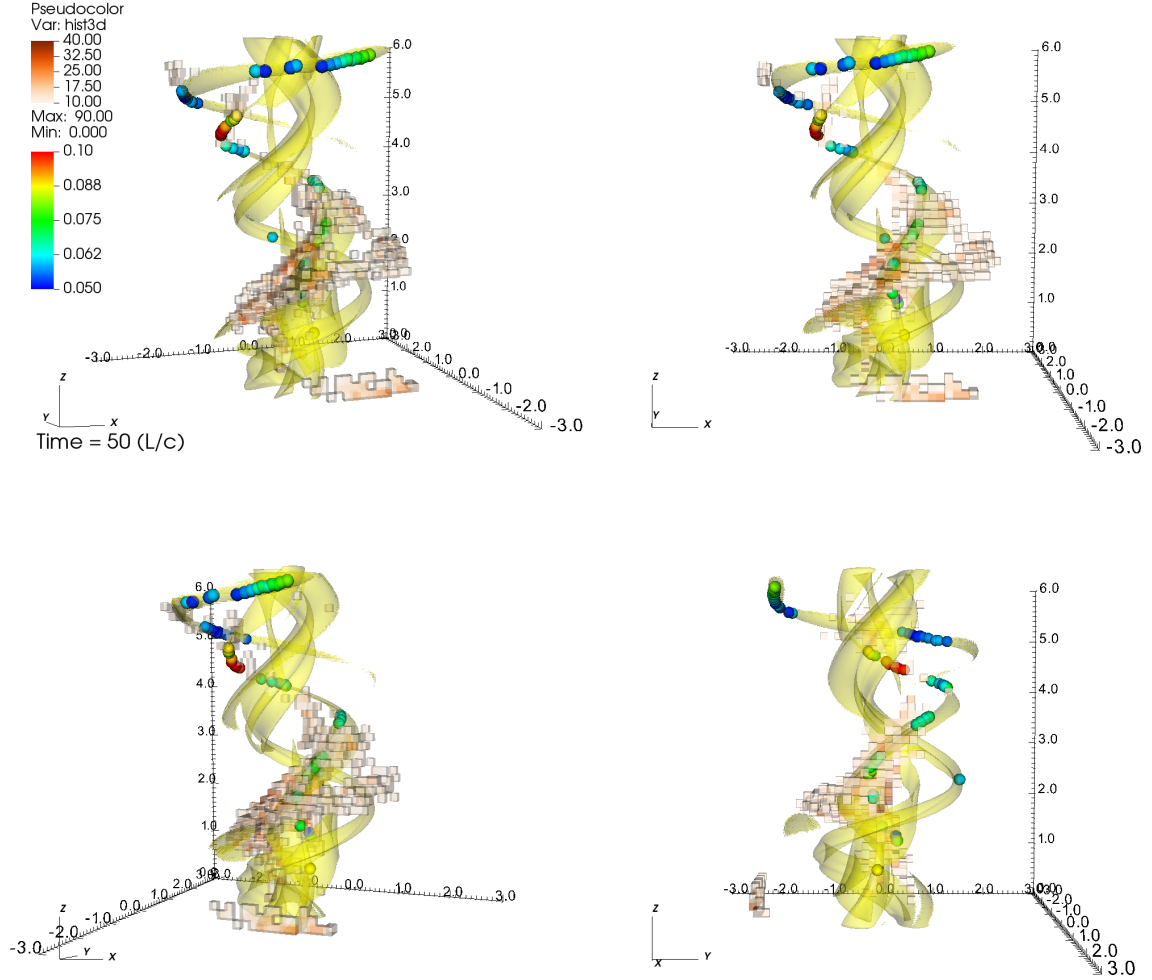


Figure 3.10: Three-dimensional histogram of accelerated particle positions (square symbols) for the snapshot  $t = 50 L/c$  of jet model  $j240$ , in different viewing angles indicated by the Cartesian axes in the bottom left of each figure. It was integrated over the particles acceleration time between 100 and 5000 hours, which corresponds to the exponential acceleration regime (see Figure 3.11, bottom right panel). Only the positions of particles accelerated with energy increment  $\Delta E_p/E_p > 0.4$  were included, and energy between  $E_p > 10^{-1} m_p c^2$  and the saturation energy  $E_p \sim 10^7 m_p c^2$ . In order to improve visualization, particles that accelerated to a maximum energy less than  $10^3$  MeV were also removed, and to avoid boundary effects, the counts were constrained to the domain between  $[-2.5, 2.5] L$  in the  $x$  and  $y$  directions, and  $[0.5, 5.5] L$  in the  $z$  direction. The circles correspond to the positions of fast magnetic reconnection sites (with velocities larger than or equal to the average reconnection speed) and their color, represent their reconnection velocity in units of the local Alfvén speed. The isosurfaces of the current density intensity at half maximum  $|J|$  (yellow color) are also depicted ( $J_{max}/2 \sim 1.25$ ).

Table 3.2: Parameters for the test particle simulations.

Test	Jet snap.	N	$B_0$	x & y	Initial distribution	Jet resolution
<i>t25o</i>	25	1,000	0.094	outflow	Maxwellian	$240^3$
<i>ut25o</i>	25	1,000	0.094	outflow	Monoenergetic	$240^3$
<i>t30o</i>	30	1,000	0.094	outflow	Maxwellian	$240^3$
<i>t40o</i>	40	5,000	0.094	outflow	Maxwellian	$240^3$
<i>t44o</i>	44	5,000	0.094	outflow	Maxwellian	$240^3$
<i>t46o</i>	46	1,000	0.094	outflow	Maxwellian	$240^3$
<i>t50o</i>	50	10,000	0.094	outflow	Maxwellian	$240^3$
<i>t50p</i>	50	1,000	0.094	periodic	Maxwellian	$240^3$
<i>9t50p</i>	50	100	9.4	periodic	Maxwellian	$240^3$
<i>9t50o</i>	50	100	9.4	outflow	Maxwellian	$240^3$
<i>480t50o</i>	50	1,000	0.094	outflow	Maxwellian	$480^3$
<i>480t30o</i>	30	1,000	0.094	outflow	Maxwellian	$480^3$
<i>480t25o</i>	25	1,000	0.094	outflow	Maxwellian	$480^3$

(see Section 2.3). This boundary condition is named "x & y" on Table 3.2. In most of the simulated models, we assume an initial Maxwellian distribution. Only in one of the models investigated, we have assumed an initial monoenergetic distribution, i.e., for *ut25o* in Table 3.2.

Figure 3.9 shows two-dimensional (2D) histograms of the positions of test particles in the snapshots  $t = 25, 30, 44, 46$  and  $50 L/c$ , projected on planes  $xy, xz,$  and  $yz$ . All histograms show only the position of particles accelerated with energy increment  $\Delta E_p/E_p > 0.4$  (here  $E_p$  is the kinetic energy of the proton) and energy larger than  $10^2$  MeV (or  $\sim 10^{-1}m_p c^2$ ), which is approximately the energy at which it starts an exponential acceleration growth (see Figure 3.11, bottom panels, in section 3.2.1 below). This condition applies to all snapshots, except to  $t = 25 L/c$ , for which particles start to undergo an exponential growth only for energies larger than  $10^4$  MeV (or  $\sim 10m_p c^2$ ). Also, only in this snapshot, the particles were injected with a monoenergetic spectrum ( $\sim 10m_p c^2$ ), as discussed in section 3.2.2, while in the other snapshots, particles were launched with a Maxwellian distribution (section 2.3).

When compared to Figure 3.1, Figure 3.9 indicates that particles are mainly accelerated along the wiggling jet spine for which the amplitude of the distortion increases as the CDKI grows and turbulent disruption develops along with the appearance of fast reconnection regions. Particles are clearly accelerated in these regions where the strength of the current density is larger and, particularly for times larger than  $t = 40 L/c$ , there are clearly several reconnection sites all over the wiggling structure. Note that while the CDKI is still growing in the early times, in  $t = 25 L/c$  there are no reconnection regions and in  $t = 30 L/c$  only very few along the jet axis. Particle acceleration in these snapshots will be discussed in section 3.2.2.

Figure 3.10 further elucidates these connections between particle’s acceleration and the sites of high current density and fast reconnection. It depicts a 3D histogram of the accelerated particles for the jet snapshot  $t = 50 L/c$ , viewed at different angles around the jet axis. The histogram was integrated over the particle acceleration time interval between 100 hours and 5000 hours, which corresponds to the exponential acceleration regime (see Figure 3.11 and section 3.2.1 below). As in Figure 3.9, only the position of particles accelerated with energy increment  $\Delta E_p/E_p > 0.4$ , and starting with energy  $\sim 10^{-1}m_p c^2$  ( $\sim 100$  MeV) were included, which is the energy when the particles start to accelerate exponentially. The particles depicted are accelerated up to the saturation energy of the exponential regime,  $\sim 10^7 m_p c^2$  (Figure 3.11, bottom panels). This figure indicates a clear association of the particles position (orange square symbols) with the acceleration regions, being mostly confined within the wiggling configuration of the half-maximum current density isocontours along the jet spine (shown in yellow). We also see a trend for a larger concentration of particles in regions of faster reconnection rates (the green, yellow, and red circles), particularly in the heights between  $1.0$  and  $3.5 L$ , and between  $4.0$  and  $5.0 L$  approximately. Besides, we note that there are also accelerated particles in the bottom and near the top of the domain. Since we have periodic boundary conditions in z-direction, these particles are likely associated with the reconnection sites seen in the top of the diagram. Finally, there are a few particles at the right edge around height  $2.0 L$  (especially when looking at the top diagrams of Figure 3.11) which seem to be detached from the maximum current density layers. An analysis of their energies indicates that most of them have already achieved the saturation value and thus have already disconnected from the reconnection regions.

In the next sections, we describe in detail the properties and the nature of the acceleration of the particles.

### 3.2.1 Magnetic Reconnection acceleration

Let us first discuss in detail particle acceleration in the more evolved snapshots of the jet, after the CDKI reaches the plateau, driving fully developed, near steady-state turbulence and fast reconnection all over the jet. Figure 3.11 compares the kinetic energy evolution of test particles injected in the snapshots  $t = 40$  (the initial time of the plateau),  $44$ ,  $46$ , and  $50 L/c$ , from top left to bottom right panels, respectively. The small plots in detail in each diagram show the evolution of the Larmor radius of the particles, with the orange line representing the cell size of the jet simulation and the blue line corresponds to the mean value of the Larmor radius.

As in previous studies of test particles in single currents sheets (Kowal et al., 2011, 2012; del Valle et al., 2016), we clearly see that the injected particles, after an initial slow drift, undergo an exponential growth in their kinetic energy up to a maximum value

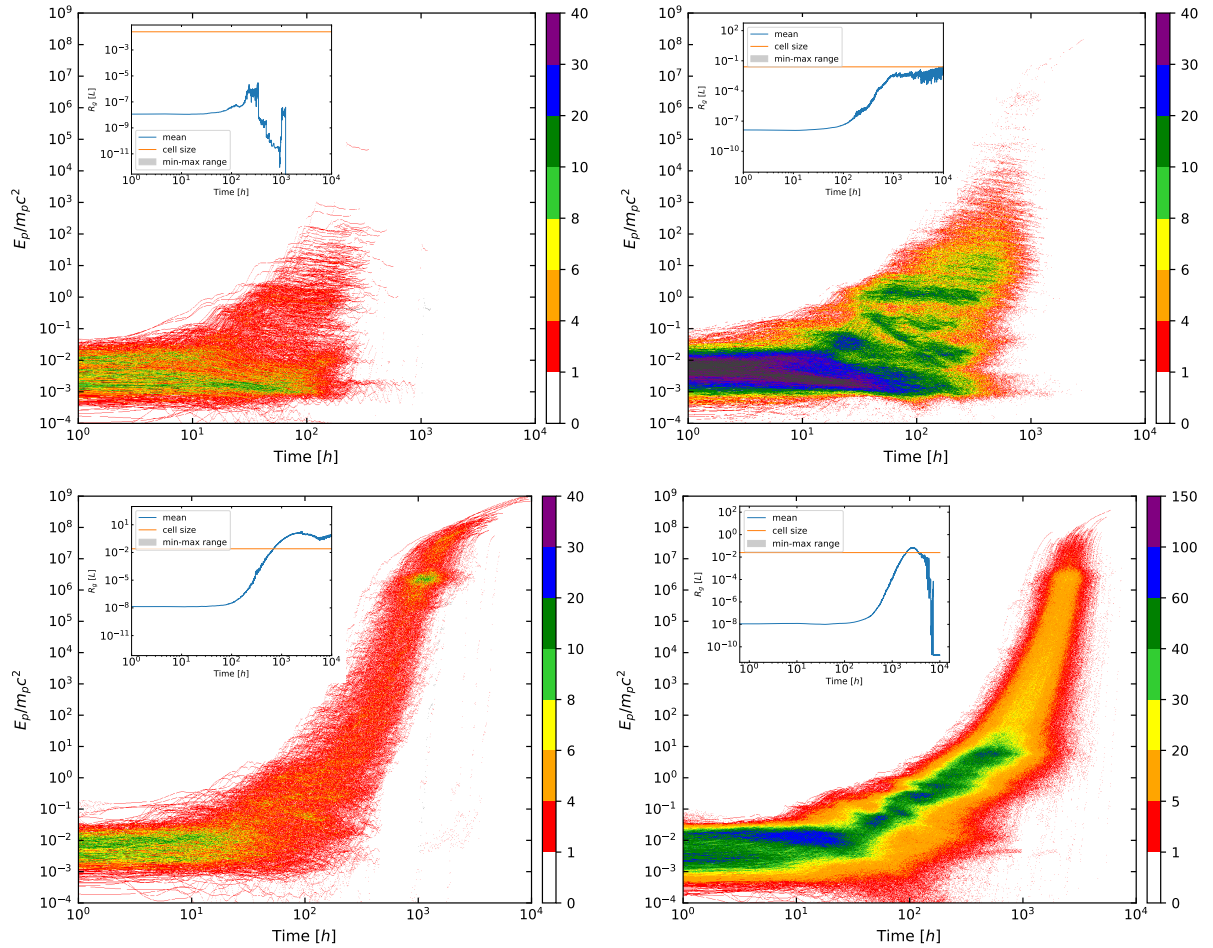


Figure 3.11: Kinetic energy evolution (normalized by the proton rest mass energy, which is equivalent to  $(\gamma - 1)$ ) for the particles injected in the snapshots  $t = 40, 44, 46$  and  $50 L/c$  of the jet model  $j240$ , from top left to bottom right, respectively. The color bars indicate the number of particles. The small plots in the upper left of each panel show the time evolution of the particles gyro-radius. The horizontal orange line corresponds to the cell size of the simulated background jet, the grey color corresponds to the entire distribution of gyro-radius values, and the blue line gives the average value.

around  $\sim 10^7 m_p c^2$  or  $\sim 10^{10}$  MeV, around  $t \sim 10^3$  hr, for the snapshots  $t = 46$ , and  $50 L/c$ . This is due to the stochastic Fermi-like acceleration in the current sheets, as described in chapter 1 (see also de Gouveia Dal Pino and Lazarian, 2005; de Gouveia Dal Pino and Kowal, 2015). The maximum energy growth corresponds to a Larmor radius  $E/(qB) \sim 4L$ , which is approximately equal to the perturbed jet diameter, above which the particles escape from the acceleration region (Kowal et al., 2012; del Valle et al., 2016). Beyond this value, the energy of the particle may still grow further, as we see for the  $t = 46$  and  $50 L/c$  snapshots, but at a smaller rate. As it is seen also in Kowal et al. (2011, 2012), this is due to further linear drift acceleration in the varying background large scale magnetic field of the system. The Larmor radius evolution plots indicate that initially, it is very small compared to the size of the cell. When it approaches the cell size, particles then start to interact resonantly with the magnetic fluctuations of the background plasma, undergoing exponential growth both in energy and Larmor radius.

We note that in the snapshot  $t = 40 L/c$  of Figure 3.11, which has not developed yet full turbulence with a substantial number of very fast reconnection events (Figure 3.1 and Table 3.1), though particles also undergo exponential acceleration, most of them do not achieve the saturation energy, contrary to what happens in the more evolved snapshots where nearly steady-state, and fully developed turbulence has been already achieved. In the more evolved time  $44 L/c$  (see Figure 3.11 top right) we identify a few more particles achieving the saturation energy similar to  $t = 46$  and  $50 L/c$  snapshots, but still a smaller number. This could, in principle, be also explained by the smaller number of very fast reconnection sites in  $t=44 L/c$  with peak velocities as large as those found in the snapshots  $t=46$  and  $50 L/c$ , as indicated by Figure 3.5 and Table 3.1. In any case, we will see later on (in Section 3.2.4) that this snapshot produces very similar particle acceleration times as those of the more evolved snapshots.

In Figure 3.12 we show the energy evolution of the accelerated particles for the same snapshots as in Figure 3.11, except that now we have separated the velocity components of the accelerated particles. The colors depict which component of the velocity of the particles is being predominantly accelerated, red for the parallel and blue for the perpendicular component to the direction of the local magnetic field. More specifically, we have that in the parallel case  $u_{//} > u_{\perp}$  and  $du_{//}/dt > 0$ , and in the perpendicular case  $u_{\perp} > u_{//}$  and  $du_{\perp}/dt > 0$ . We note that in the exponential regime, there is a clear dominance of the parallel component, characterizing an effective electric field mostly parallel to the reconnection layers, as expected, though the stochastic nature of the whole process also allows for the acceleration of the perpendicular component (see also Kowal et al., 2011, 2012). The slower drift acceleration regimes, both in the beginning and after the exponential growth regime, are dominated by the acceleration in the perpendicular direction of the local magnetic field.

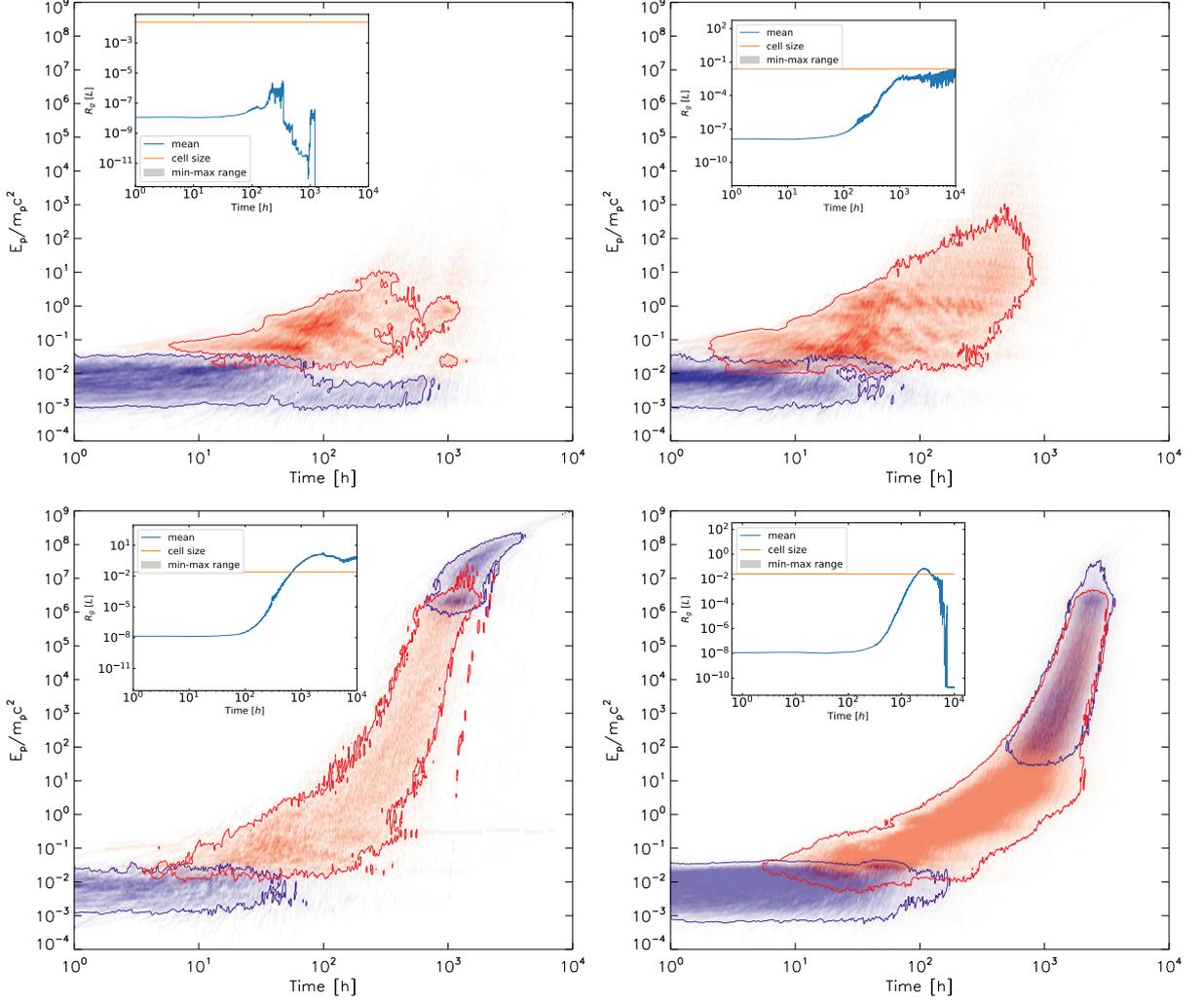


Figure 3.12: Kinetic energy evolution, normalized by the proton rest mass energy, for the particles injected in the snapshots  $t = 40, 44, 46$  and  $50 L/c$  of the jet model  $j240$ , from top left to bottom right, respectively. The colors indicate which particle velocity component is being accelerated (red or blue for parallel or perpendicular component to the local magnetic field, respectively). The small plots in the upper left inset of each panel show the time evolution of the particles gyro-radius. The horizontal orange line corresponds to the cell size of the simulated background jet, the grey color corresponds to the entire distribution of gyro-radius values, and the blue line gives the average value.

### 3.2.2 Particle acceleration in the earlier stages of the CDKI

As remarked previously, there are no identified reconnection events in the jet snapshot  $t = 25 L/c$  (Figure 3.1) and thus one would not expect any acceleration by magnetic reconnection. Nevertheless, motivated by the recent work of Alves et al. (2018) who claimed to detect magnetic curvature drift acceleration in a relativistic jet subject to the kink mode instability, we have also launched test particles in this snapshot in order to seek out for this process (see test particle model *t25o* in Table 3.2). The results are presented in Figure 3.13. The upper diagram (*t25o*) shows particles launched with similar initial energy distribution and intensity as in the evolved snapshots of Figure 3.11. In this case, we see that part of the particles undergo some acceleration, but saturate at an energy  $E_p \sim m_p c^2$ , which is much smaller than the values reached by the particles accelerated by reconnection in the evolved snapshots of Figure 3.11. Some particles even lose their energy. On the other hand, if we inject particles with an initial much larger energy  $10^4$  MeV or  $\sim 10m_p c^2$  (see test particle model *ut25o* in Table 3.2), they are accelerated as efficiently as in the evolved snapshots of Figure 3.11, though we find that part of the particles still lose their energy as in the run of the top diagram of Figure 3.13. A closer view into the plot of the Larmor radius evolution, indicates that this also increases exponentially once their value gets closer to the cell size of the background jet and exceeds it. This exponential acceleration is similar to what Alves et al. (2018) obtained in their PIC simulation of a tower jet.

Particle acceleration by magnetic curvature drift may also occur in helical jets subject to kink mode instability (Alves et al., 2018). It may happen in the early stages of the development of the instability, before turbulence and reconnection break out. As we have seen in section 1.3.1, the kink instability induces a growing helical modulation of the jet spine (see top panels of Figure 3.1), and the transverse motions excite an inductive electric field,  $\mathbf{E} = -\mathbf{v} \times \mathbf{B}/c$ . According to Alves et al. (2018), the axial component of this field  $\langle E_z \rangle$  becomes strong and coherent throughout the jet spine when the transverse displacements excited by the tangling magnetic field of the jet become comparable to its radius, i.e., when the kink instability enters the non-linear regime. This leads to a potent acceleration that we see in the bottom panel of Figure 3.13. However, we clearly see the difference from the comparison of the two diagrams of Figure 3.13 that, in order to the particles feel the effects of curvature drift they require some pre-acceleration.

The Figure 3.14 also depicts the particles kinetic energy evolution as the bottom panel of Figure 3.13, but with the velocity components separated, being red for the parallel, and blue for the perpendicular component to the direction of the local magnetic field. In contrast to the panels of Figure 3.12, we see a dominance of the perpendicular component in the exponential regime and beyond that, thus confirming the dominance of the curvature drift acceleration in this case where the accelerating electric field perpendicular

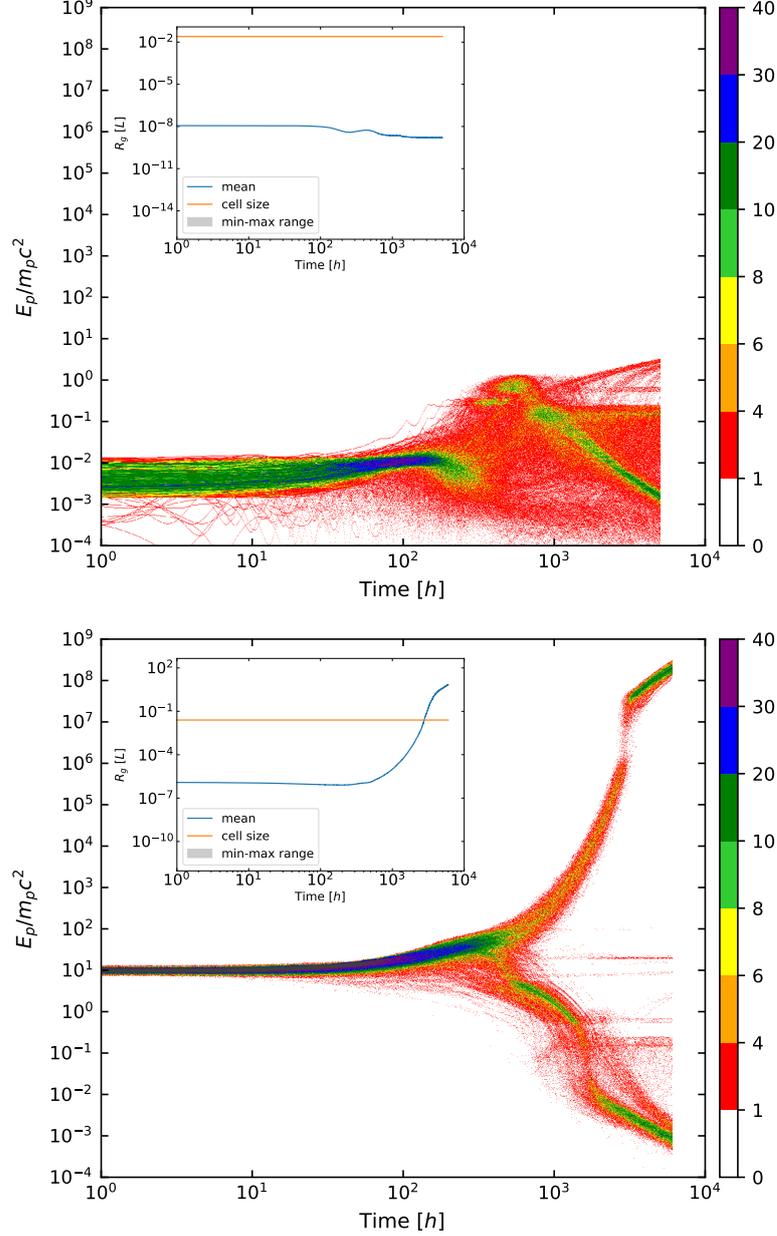


Figure 3.13: Kinetic energy evolution for particles injected in the snapshot  $t = 25 L/c$  of the jet model  $j240$ . The top panel corresponds to particles injected with a Maxwellian distribution and  $\langle E_p \rangle \sim 10^{-3} m_p c^2$ , as in Figure 3.11. The bottom panel corresponds to particles injected with a monoenergetic distribution with larger energy  $E_p \sim 10 m_p c^2$ . The color bar indicates the number of particles. The small plots in the detail depict the evolution of the particles gyro-radius, the same as in Figure 3.11.

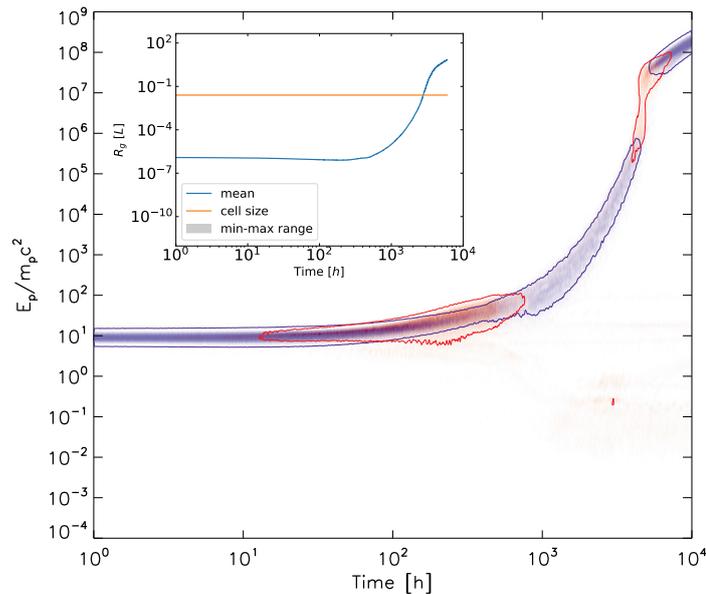


Figure 3.14: Kinetic energy evolution for particles injected in the snapshot  $t = 25 L/c$  of the jet model *j240*, corresponds to particles injected with a monoenergetic distribution with larger energy  $E_p \sim 10m_p c^2$ , the same as in right panel of Figure 3.13. The colors indicate which particle velocity component is being accelerated (red or blue for parallel or perpendicular component to the local magnetic field, respectively). The small plot in the detail depict the evolution of the particles gyro-radius, the same as in Figure 3.13.

to the magnetic field prevails.

Figure 3.15 depicts the kinetic energy evolution of test particles injected in the jet snapshot  $t = 30 L/c$  (*t30o* in Table 3.2), for which a few fast reconnection sites have been detected (see Figure 3.1). This snapshot is also still in the non-linear growing phase of the CDKI in the jet, before saturation (Figure 3.6). The particles were injected with the same initial energy  $\sim 1 \text{ MeV}$  ( $\sim 10^{-3}m_p c^2$ ) as in the evolved jet snapshots of Figure 3.11, or the model of the top panel of Figure 3.13.

Interestingly, the particles now undergo an exponential increase in the kinetic energy up to the same maximum value of the more evolved snapshots (Figure 3.11, snapshots  $t = 46$  and  $50 L/c$ ), even having only a few fast reconnection sites. Furthermore, contrary to what we see in snapshot  $t = 25 L/c$  (Figure 3.13), where particles could accelerate by magnetic curvature drift only starting with injection energy around  $10^4 \text{ MeV}$  (or  $\sim 10m_p c^2$ ), at  $t = 30 L/c$  they get accelerated starting with energies well below ( $\sim 10^{-3}m_p c^2$ ), as in the evolved snapshots. These results suggest that the particles are also experiencing magnetic reconnection acceleration in this case. Moreover, it seems that when reconnection is present, particles do not require the pre-acceleration, as in  $t = 25 L/c$  snapshot (Figure 3.13 bottom panel). During the exponential growth, the fact that both processes are present, i.e., fast reconnection and a large amplitude tangled spine with a still coherent magnetic field, it is possible that both mechanisms, curvature drift

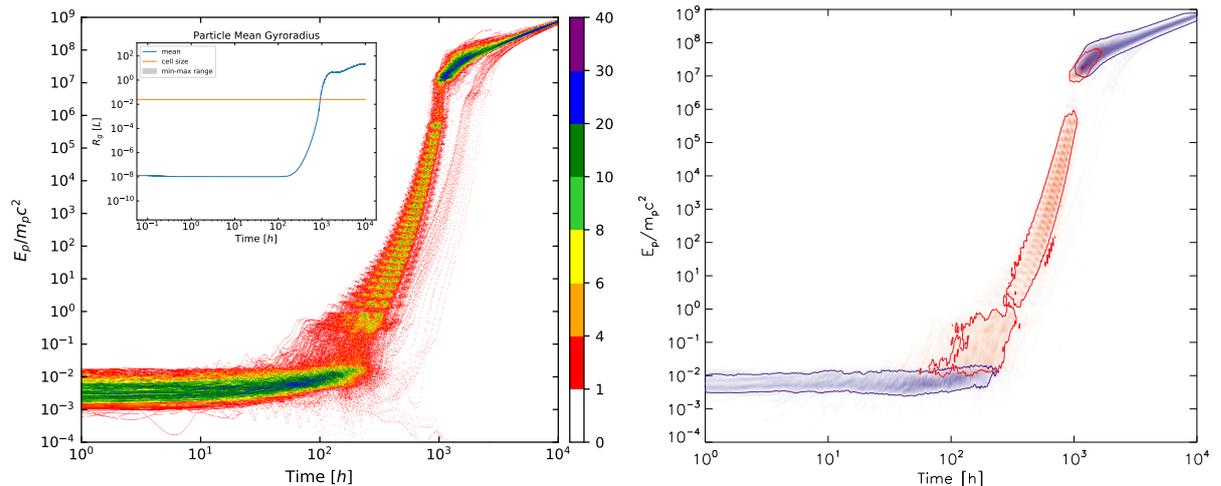


Figure 3.15: Kinetic energy evolution for particles injected in the snapshot  $t = 30 L/c$  of the jet model  $j240 (t30o)$ . As in Figure 3.11, particles are injected with  $\langle E_p \rangle \sim 10^{-3} m_p c^2$  and a Maxwellian distribution. The color bar in the left panel indicates the number of particles and the small plot in the detail depicts the evolution of the particles gyro-radius. The two colors in the right panel indicate which velocity component of the particles is being accelerated (red or blue for parallel or perpendicular component to the local magnetic field, respectively).

and reconnection acceleration, are operating simultaneously. This combination may also explain why we see a more efficient acceleration in this snapshot than around  $t = 40 L/c$ , when CDKI had just saturated and turbulent reconnection had just broken out, driven by it.

In fact, the right panel of Figure 3.15, indicates that the dominant velocity component accelerated in the exponential region is the parallel (as in Figure 3.12), though the number of particles is smaller in this regime, while in the more extended region of slower acceleration beyond that, where we see a much larger concentration of particles, the dominant component is the perpendicular one. The dominance of the parallel component in the exponential region is suggestive of a predominance of reconnection acceleration, while the dominance of the perpendicular component in the second region is characteristic of curvature and normal drift acceleration.

### 3.2.3 Resolution Effects

In order to examine potential resolution effects, we have also injected test particles in the higher resolution background relativistic jet simulation (model  $j480$  of Table 2.1). Figure 3.16 shows the kinetic energy evolution for accelerated particles launched at snapshot  $t = 50 L/c$  of this jet (test particle model  $480t50o$  in Table 3.2). The initial conditions for this run are the same as in the corresponding lower resolution model at  $t = 50 L/c$  (see bottom right panel of Figure 3.11).

Comparing Figure 3.16 with its lower resolution counterpart in Figure 3.11 (bottom right panel), we clearly see that they are very similar. The only visible difference is due to the number of test particles used in each test. In the snapshot of the lower resolution jet model, we employed 10,000 particles, while in the high resolution jet model we injected only 1,000 particles, for being computationally much more time consuming and expensive. The energy growth rate is also very similar in both cases, as we will see in the next section (Figure 3.18), though the particles in the higher resolution case reach the saturation energy of the exponential growth regime a little before  $10^3$  hr, while in the low resolution jet, a little after  $10^3$  hr, reflecting a slightly larger acceleration rate in the higher resolution case (see Figure 3.18).

This is due to the fact that in the higher resolution jet (smaller cell size), more regions of fast magnetic reconnection can be resolved at smaller scales, so that particles, starting with smaller Larmor radius, can interact more frequently with resonant magnetic fluctuations, making the acceleration rate slightly more efficient. In fact, we have found that the number of reconnection sites is six times larger than in the lower resolution jet (see Table 3.3). Nevertheless, since the change in the acceleration rates or the particles spectra are not substantial (see section 3.2.4 and 3.2.5), we proceed our analysis considering mainly the lower resolution jet model (*j240*), because the employment of the larger resolution counterpart for the entire analysis would be computationally rather long and expensive.

We should note that we have also repeated the test particle run for the earlier stages of the CDKI (see Figure 3.17). For the snapshot  $t = 25 L/c$  (as in the top panel of Figure 3.13, section 3.2.2), but employing the higher resolution jet model (*j480*), and we have obtained the same result, thus showing that that result is also not changed by the increase of the background resolution. It is important to emphasize that the search algorithm which we are using to identify reconnection sites, also found no reconnection regions in the higher resolution model at this snapshot (see Table 3.3), as in the lower resolution (Table 3.1).

On the other hand, for  $t = 30 L/c$ , we see that while the search algorithm has identified 25 reconnection sites in the lower resolution jet model (*t240*), in the higher resolution it identified only one event (see Tables 3.1 and 3.3). In order to see the effects of these results, we have also injected test particles in the higher resolution jet snapshot  $t = 30 L/c$  and found a similar result as that of the low resolution model in Figure 3.15, i.e., particles are accelerated up to energies close to  $10^8 m_p c^2$  in  $\sim 10^3$  hours (see Figure 3.17, bottom). This indicates that even a single fast reconnection event is enough to trigger the particle acceleration. In fact, in the next section we will see that the particle acceleration times obtained for both resolution models in this snapshot are almost indistinguishable (see Figure 3.19). A similar behavior is detected in all the other snapshots tested in the two resolutions.

Table 3.3: Reconnection velocity values in units of the local Alfvén speed in j480.

Jet snapshot	$\langle V_{rec} \rangle$	$max(V_{rec})$	Total counts	Counts ( $V_{rec} \geq \langle V_{rec} \rangle$ )
25	0	0	0	0
30	0.02	0.02	1	1
40	0.03	0.08	406	178 (44%)
44	0.03	0.1	829	344 (41%)
46	0.03	0.2	844	326 (39%)
50	0.06	0.2	878	352 (40%)

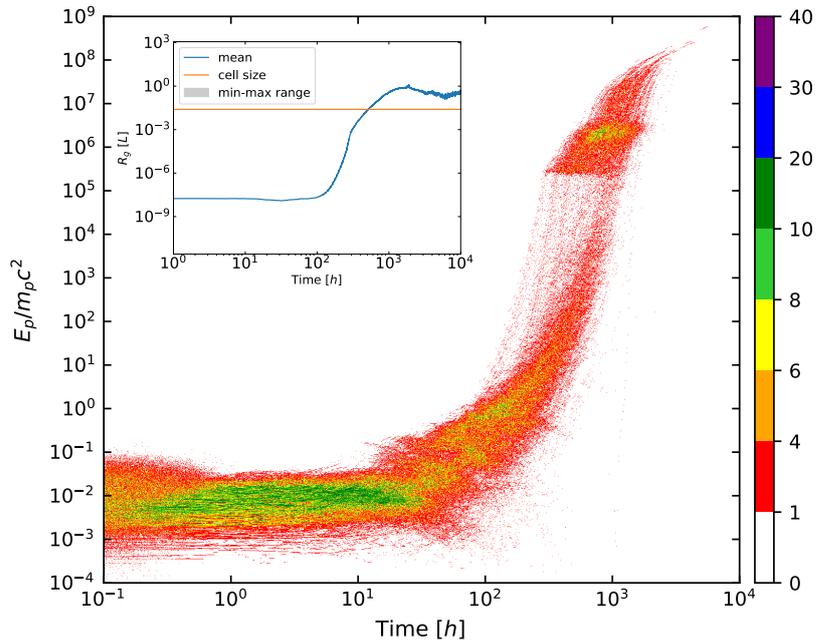


Figure 3.16: Particle kinetic energy evolution, normalized by the rest mass energy, for 1,000 protons injected in  $t = 50 L/c$  snapshot of the higher resolution jet model ( $t480$ , see Table 2.1). The initial conditions for the test particles are the same as in the lower resolution test shown in Figure 3.11 for the same time step (bottom panel), except that there 10,000 protons were used. The color bar indicates the number of particles. The small plot on upper left shows the evolution of the particles gyro-radius.

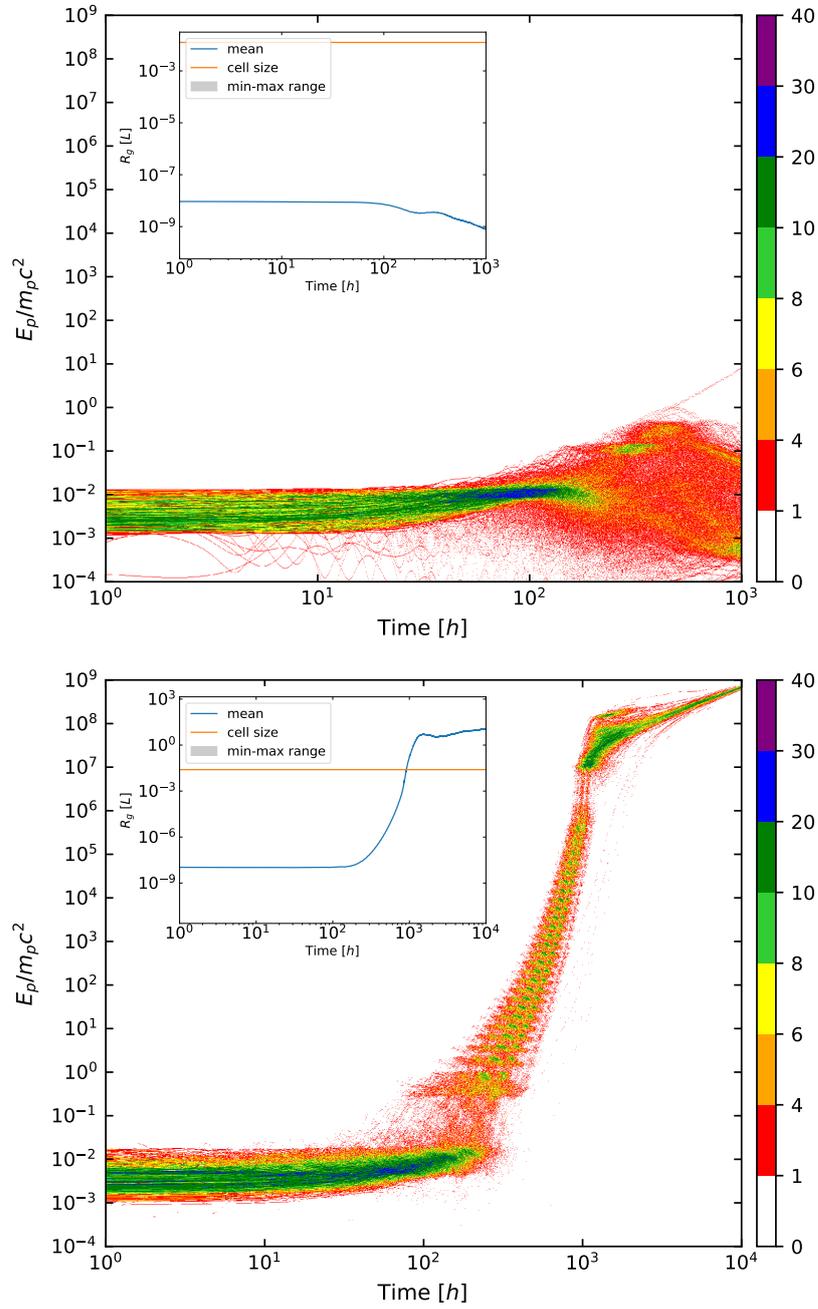


Figure 3.17: Particle kinetic energy evolution, normalized by the rest mass energy, for 1,000 protons injected in  $t = 25$  (upper)  $t = 30 L/c$  (bottom) snapshots of the higher resolution jet model ( $t480$ , see Table 2.1),  $480t25o$  and  $480t30o$ , respectively. The initial conditions for the test particles are the same as in the lower resolution test shown in Figure 3.13 (top panel) and Figure 3.15 for the same time step (bottom panel). The color bar indicates the number of particles. The small plot on upper left shows the evolution of the particles gyro-radius.

### 3.2.4 Particle acceleration rates

Magnetic reconnection acceleration, as in the Fermi process, predicts a dependence of the acceleration rate with the reconnection velocity and the particles energy (de Gouveia Dal Pino and Kowal, 2015; del Valle et al., 2016; Matthews et al., 2020). Similarly as in del Valle et al. (2016), in order to quantify the effectiveness of the acceleration of the particles for each test particle model (Table 3.2), we have calculated the average time per energy interval that particles take to reach a certain energy, which gives the *acceleration time* as a function of the energy shown in Figure 3.18 (top panel) for all the models. Using the same simulated data set, we depict in Figure 3.18 (middle panel), the power law index,  $\alpha = \Delta \log(t_{acc}) / \Delta \log E_p$ , of the the acceleration time dependence with particle energy,  $t_{acc} \propto E_p^\alpha$  (see also Section 2.3).

In both, top and middle diagrams of Figure 3.18, the particles in the different models enter the exponential growth regime of acceleration approximately around the energy  $\sim 10^{-1} m_p c^2$  (in agreement with the diagrams of particle kinetic energy evolution of Figures 3.11 to 3.16), and end the exponential growth near  $\sim 10^7 m_p c^2$  (except for model 9t50p that we discuss below in section 3.2.7). Before starting the exponential acceleration, the particles experience a slower growth in their energies which reflects in the larger  $\alpha$  index, especially for  $t = 25 L/c$ . The test corresponding to the snapshot  $t = 30 L/c$  has the smallest  $\alpha$  during this initial phase (dark blue line in Figure 3.18), characterizing a smoother transition to the exponential acceleration regime. This is compatible with the previous analysis where we have seen that in this early snapshot, the particles are experiencing both, magnetic curvature drift and reconnection acceleration. During the exponential growth regime,  $\alpha$  decreases to similar values around  $\alpha \sim 0.09 \pm 0.05$  for all models and energies in this regime.<sup>1</sup>

Beyond the exponential regime, the acceleration time and the  $\alpha$  index grow a little further due to the slower drift acceleration that particles experience after leaving the reconnection (or curvature drift in the case of  $t = 25 L/c$ ) acceleration regions, as discussed in Figures 3.11 to 3.16 (sections 3.2.1 and 3.2.2).

The kinetic energy growth rate as a function of the particle energy depicted in the bottom diagram reflects the results of the upper panels. It increases with the energy, at the same rate in the exponential regime for all models. Interestingly, the only model that shows a slightly smaller rate (and slightly larger  $\alpha$  index) is the one corresponding to snapshot  $t = 25 L/c$ , possibly due to the different acceleration process.

A closer look into the acceleration time presented in the top diagram of Figure 3.18, shows some slight differences between the models. Though these differences are approx-

---

<sup>1</sup>We note that the error bars in this determination were derived taking into account only the models having the jet *j240* as background, but the same value of  $\alpha$  is derived for the particle models having the higher resolution jet as background.

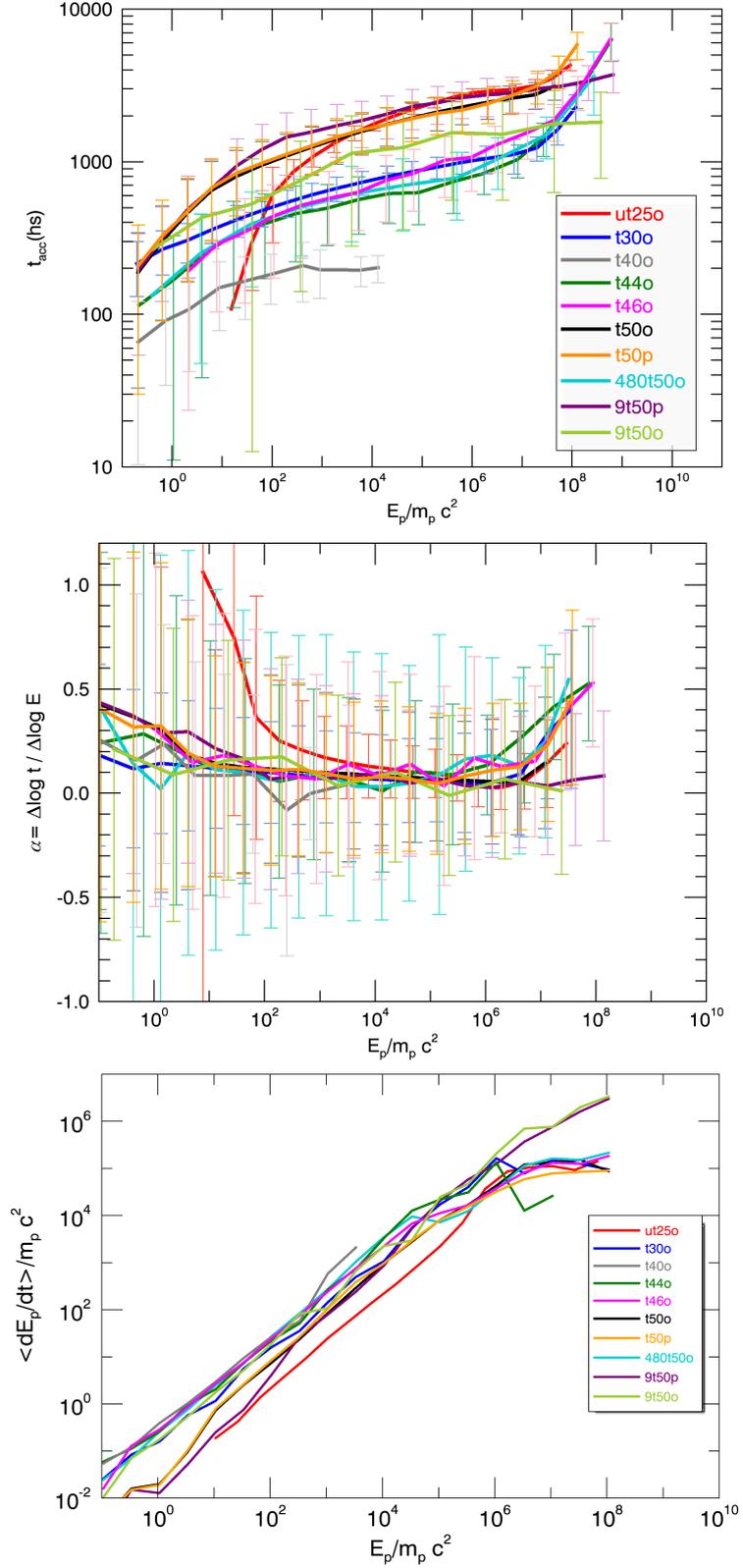


Figure 3.18: Acceleration time (top panel), power law index of the acceleration time,  $\alpha$  index (middle), and kinetic energy growth rate (bottom) as functions of the particle kinetic energy normalized by the proton rest mass energy for the different test particle models of Table 3.2. The error bars are obtained calculating the standard deviation.

imately encompassed by the uncertainties of the numerical calculations (as we see from the error bars, which were calculated by the standard deviation method), the higher resolution jet model (480t50o) produces a slightly smaller acceleration time than its lower resolution test counterpart (t50o). This is compatible with the results found in Figures 3.16 and 3.11 (bottom right), discussed in section 3.2.3).

Another interesting result is that for snapshot  $t = 30 L/c$  (t30o in Figure 3.15) which also shows (for both jet model resolutions) a smaller acceleration time, comparable to that of more evolved snapshots, like  $t = 44 L/c$  (t44o) and  $t = 46 L/c$  (t46o), for which we have detected a large number of fast reconnection sites with rates larger than the average value (see Table 3.1). Furthermore, these tests have acceleration times comparable to the high resolution model (480t50o). Regarding the models t44o and t46o, the larger efficiency can be attributed to the larger number of fast reconnection regions, while in t30o, this seems to be due to the combination of the two acceleration processes (as discussed in section 3.2.2).

In Figure 3.19, we compare the acceleration time and the alpha index of model  $t = 30 L/c$  in the lower (j240) and higher (j480) resolutions. This because in the scale of Figure 3.18 they cannot be distinguished, which is very good (and consistent with the other resolution tests presented in section 3.2.3). Nevertheless, it is curious that a single reconnection site has been identified in the high resolution model j480 (see Table 3.3). This may be due to the limitations of the reconnection search algorithm (Kadowaki et al., 2018b; ?), whose criteria may eventually fail in the identification of some reconnection sites. Also, analyzing the evolution of the accelerated velocity components of the particles in this higher resolution model, we have found a dominance of the parallel component to the local magnetic field in the exponential regime, as in the lower resolution model of Figure 3.15, characteristic of reconnection acceleration.

More peculiar behavior in Figure 3.18 is found in the acceleration time for the snapshot  $t = 40 L/c$  (t40o in the top diagram), which shows the lowest values since the beginning. We remind that this snapshot corresponds to the achievement of the plateau of the CDKI and the transition of the jet from the laminar to the fully developed turbulence regime. Besides, it has already several sites of fast reconnection, but all with velocities near the average value (Figure 3.1 and Table 3.1). Moreover, Figure 3.11 (top left) has indicated that in this snapshot most of the particles enter the exponential regime of acceleration, but do not achieve the saturation energy. All these facts combined seem to have favored this slightly smaller acceleration time at the beginning of the acceleration for this snapshot in the transition regime of the CDKI turbulence.

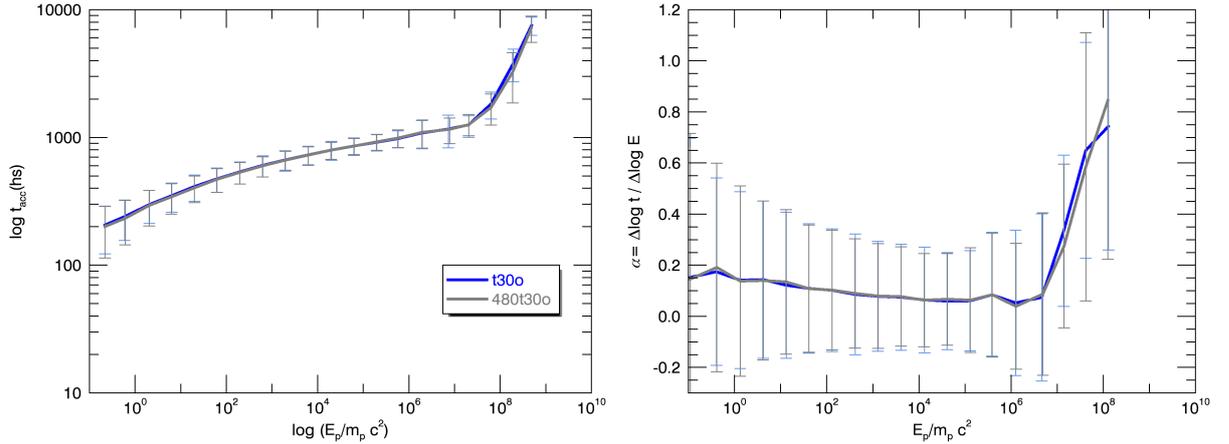


Figure 3.19: Acceleration time (left) and power law index of the acceleration time (right) of the test particles in  $t = 30 L/c$  for the jet models of lower ( $240^3$ ) and higher resolution ( $480^3$ ), t30o and 480t30o, respectively.

### 3.2.5 Particles Spectrum

Figure 3.20 shows the evolution of the energy spectrum of all particles (not only the accelerated ones) during the acceleration in the jet snapshots at  $t = 25 L/c$  (particle model *ut25o*), 30 (*t30o*), 46 (*t46o*) and 50  $L/c$  (*t50o*), from top left to bottom right panels, respectively. Several time intervals are depicted in each panel, in units of hour. Initially, the particles have a Maxwellian distribution (red line), except in the top left panel for the jet snapshot  $t = 25 L/c$ , where the injection spectrum is monoenergetic (with  $\sim 10 m_p c^2$ ). As particles accelerate, they start to populate the higher energy tail of the distribution, which becomes flatter at these energies (see the two bottom panels, in particular). We should remember that in our numerical setup, particles are continuously re-injected into the system and therefore, they never stop being accelerated. For this reason, the distribution shifts to larger and larger energies. Furthermore, even after the particles attain the maximum (saturated) energy at the end of the exponential acceleration regime due to reconnection (or magnetic curvature in the case of the snapshot  $t = 25 L/c$ , top panel), they continue to accelerate at a smaller rate due to normal drift (as remarked in Section 3.2.1).

We should also remember that the maximum energy achievable by the stochastic mechanism (at the saturation of the fast acceleration growth) occurs around  $t \sim 10^3$  hr for all the models depicted (see Figures 3.11, and 3.13), except in the top one, for which this occurs around  $t \sim 10^{3.5}$  hr (see Figure 3.13). Interestingly, we see that for this model (*ut25o*), and also model *t30o* (second panel from top), around these times, there is a double hump in the distribution (green dot-dashed curve), with an accumulation of particles at energies above  $10^7 m_p c^2$  for both, thus highlighting the transition from the exponential to the linear drift acceleration regimes. In the other models depicted, this transition is more smooth. Also notable, is the double peak in the distribution that appears in model *t30o*

in the earlier times at  $t \sim 10^2$  to  $10^{2.3}$  hr. This is possibly connected to the superposition of the two acceleration processes in this model, namely the magnetic curvature drift and the reconnection acceleration, as we discussed in section 3.2.2.

Perhaps, the most striking feature in all the diagrams of Figure 3.20 is that as particles reach very high energies, the distribution may even attain an almost zero power-law index tail in very evolved times, as we clearly see in the bottom diagram of the Figure. In real systems, however, this acceleration process should be interrupted by the escape of the particles from the finite volume of the acceleration zone and also due to radiative losses. As stressed above, since in our simulations the particles are continuously accelerated and there is no physical mechanism to allow them to escape, it is not possible to obtain the actual distribution of the accelerated particles. However, we can at least estimate the power-law index of the distribution soon after the particles start to populate the high-energy tail (see e.g., del Valle et al., 2016).

In Figure 3.21 we show the total number of particles as a function of energy for two different early timesteps of the acceleration, for the jet snapshot  $t = 50 L/c$ . The initial Maxwellian (normal) distribution is shown in a gray dotted line. The earliest time step plotted corresponds to the approximate time when a high-energy power-law tail starts to form (i.e., when particles reach kinetic energies larger than  $\sim 10^{-1} m_p c^2$ , according to Figure 3.11, bottom right panel); the second time corresponds to a little later time step. We see that the power-law index at the earlier time can be fitted by  $p = -1.19$ . The second power-law at later time is flatter due to the effects discussed above and therefore, it must be taken only as illustrative of the limitations of the method. Of course, in realistic systems, the presence of physical particle escape from the acceleration zone, radiative losses and dynamical feedback of the accelerated particles into the plasma will result in steeper spectrum in the late times too ( $|p| > 1$ ).

### 3.2.6 Boundary effects

As described in section 2.3, in most of the particle runs, we have allowed the particles to re-enter the system only through the jet periodic boundaries, along the  $z$  direction. Nevertheless, we have also performed a few tests where we allowed the particles to be re-injected into the system through all the boundaries, i.e., also when crossing the jet outflow boundaries in the  $x$  and  $y$  directions, aiming at increasing the number of accelerated particles. In Table 3.2, these few tests are labeled with “p”. Figure 3.22 shows one of these tests performed for the jet model  $j240$  in the snapshot  $t = 50 L/c$  (model  $t50p$ ), for which 1,000 particles were initially injected. It can be compared with its counterpart model shown in the bottom right panel of Figure 3.11, in which 10,000 particles (rather than 1,000) were injected and allowed to re-enter the system only in the  $z$  direction (test particle model  $t50o$ , Table 3.2). We note that both models have very similar behavior,

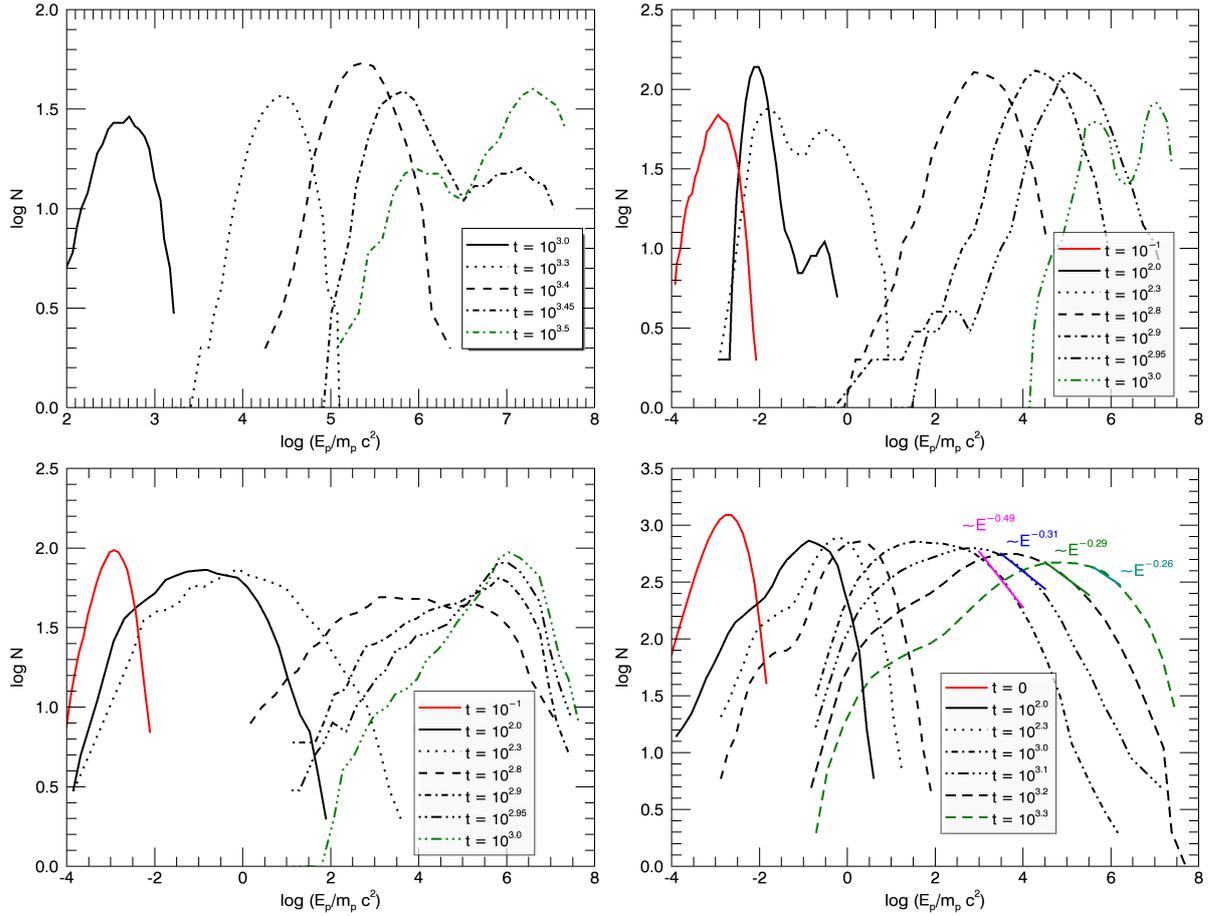


Figure 3.20: Particles energy spectrum evolution as a function of the normalized kinetic energy ( $m_p c^2$ ) in the jet snapshots, from top left to bottom right:  $t = 25$  (particle model *ut25o*); 30 (particle model *t30o*), 46 (*t46o*), and  $50 L/c$  (test particle model *t50o*). The red line in all panels but the top left, corresponds to the initial Maxwellian distribution of the particles. In the top left panel particles are injected with a monoenergetic spectrum. The timesteps (in hours) of the acceleration are depicted in the detail of each panel.

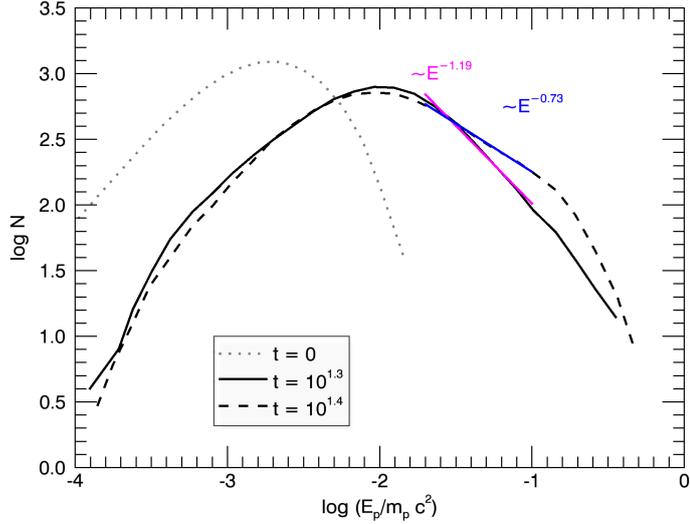


Figure 3.21: Particle energy spectrum as a function of the normalized kinetic energy at two different early time steps of the acceleration (in hours) for the jet snapshot  $t = 50 L/c$ . The dotted gray line is the initial Maxwellian distribution. The high energy tail of each distribution is fitted by a power-law.

except for the number of particles that are being accelerated along the system evolution. While in model  $t50o$  (bottom right panel of Figure 3.11), there are more particles at the beginning of the evolution, due to the much larger number of injected particles, in model  $t50p$  (Figure 3.22), we see a larger number of particles that are accelerated up to the maximum energy at the exponential regime and beyond, due to the larger number of re-injected particles in the periodic boundaries in all directions. We also see in Figure 3.18 that both models have similar acceleration properties, i.e., acceleration rate, power-law index  $\alpha$ , and kinetic energy growth rate.

### 3.2.7 Magnetic field effects

As in Figure 3.11 (bottom right diagram, test particle model  $t50o$ ), Figure 3.23 also shows the kinetic energy evolution for particles injected at snapshot  $t = 50 L/c$  of the jet model  $j240$ , except that now the initial background magnetic field at the jet axis is 100 times larger ( $B_0 = 9.4G$ ), corresponding to the test particle model  $9t50o$  of Table 3.2.

This change in the physical unit value of the magnetic field of the background jet was made in such a way that we have kept the scale invariance in the jet system. In other words, as stressed in section 2.1, the magnetic field code unit in the RMHD jet simulation is given by  $\sqrt{4\pi\rho_0 c^2}$ . Thus, when increasing the physical unit of the magnetic field by a factor of 100, we had also to increase the background density physical unit by a factor  $10^4$ , in order to keep unaltered the magnetic field in code unit and thus, the corresponding Alfvén speed. This means that in this test particle model with larger physical magnetic fields and densities ( $9t50$ ), the background reconnection velocities have also maintained

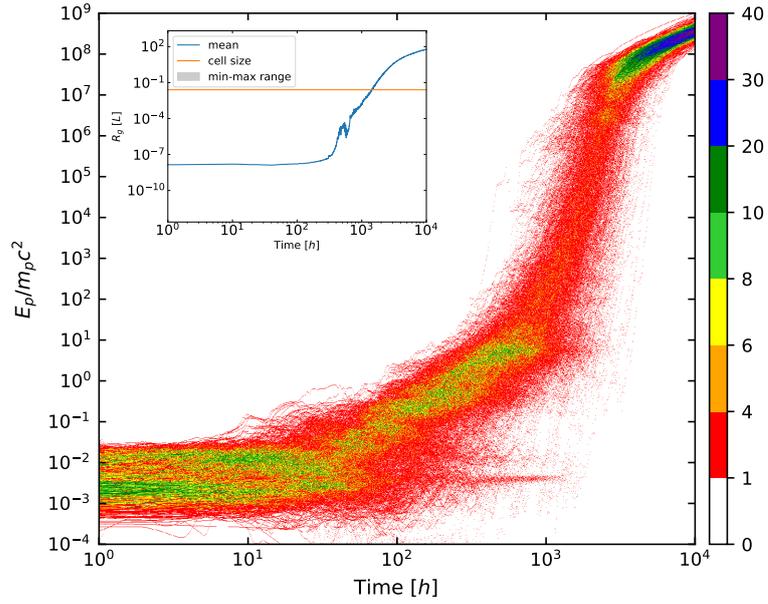


Figure 3.22: Particle kinetic energy evolution, normalized by the rest mass energy, for particles injected in  $t = 50 L/c$  snapshot of the jet model ( $j240$ , see Table 3.2). This test is similar to that of the bottom right diagram of Figure 3.11, except that here particles were periodically re-injected through all the boundaries of the jet system (see model  $t50p$  in Table 3.2). The color bar indicates the number of particles. The small plot on the upper left shows the evolution of the particles gyro-radius.

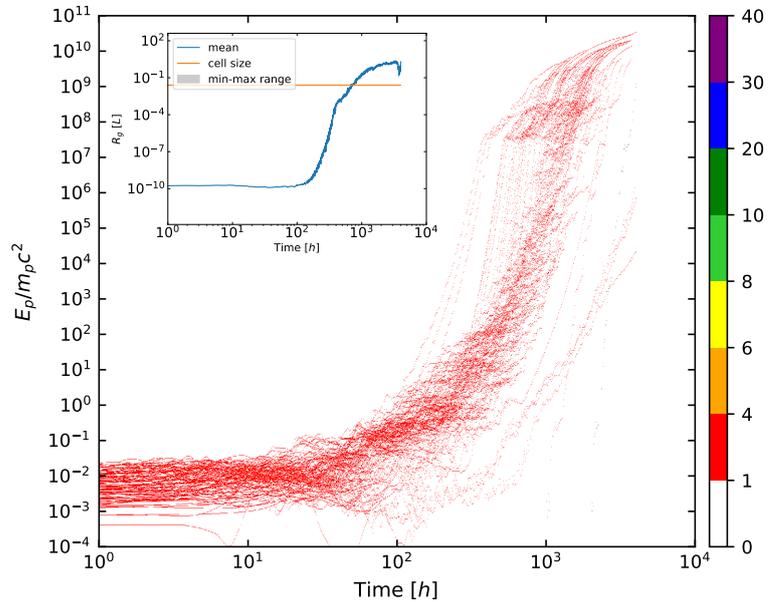


Figure 3.23: Kinetic energy evolution for particles injected at snapshot  $t = 50 L/c$  ( $9t50o$ ) of the jet model  $j240$  with an initial background magnetic field at jet axis  $B_0 = 9.4$  G and a background density  $\rho_0 = 10^4 \text{ cm}^{-3}$  (see Table 3.2). The initial conditions are the same as in the test particle model ( $t50o$ ) shown in the bottom right panel of Figure 3.11, except that there  $B_0 = 0.094$  G and  $\rho_0 = 1 \text{ cm}^{-3}$ , leaving unaltered the Alfvén velocity in both tests (see text for details). The color bar indicates the number of particles and the small plot in the detail shows the evolution of the particles gyro-radius.

the same as in model *t50o*. Therefore, particles in this new model (*9t50*) should feel essentially the same acceleration rates of the counterpart test model with the smaller jet magnetic field and density (model *t50o*). This is what we see comparing these models in the diagrams of Figure 3.18.

On the other hand, a closer view of Figure 3.23 shows that the increase of the background magnetic field by a factor of one hundred causes an increase of the maximum energy achieved by the particles also by two orders of magnitude with respect to the counterpart model *t50o* (see Figure 3.11, bottom right panel). In other words, while the maximum energy that particles attain in the exponential regime in model *t50o* is  $\sim 10^7 m_p c^2$ , in model *9t50*, it is  $\sim 10^9 m_p c^2$  (see also Figure 3.18). The plot in the detail of Figure 3.23 shows that the corresponding maximum Larmor radius ( $\propto E_p/B$ ) is the same as in model *t50o*, this because in both test particle models, the ratio of the maximum energy to the background magnetic field is the same, or in other words, the physical size of the acceleration region is the same in both cases. The slower drift acceleration that follows the exponential growth, accelerates the particles even further to an energy  $\sim 10^{10} m_p c^2$ .

Finally, we note that this test particle model with  $B_0 = 9.4$  G was also run considering periodic boundaries in all directions (see model *950p* in Table 3.2), and the results are very similar to those of the model *9t50o*, with periodic boundaries only in the  $z$ -direction, of Figure 3.23, in agreement with the results of Section 3.2.6. Also, both models present similar acceleration times,  $\alpha$  index, and energy growth rates, as indicated in Figure 3.18.

### 3.3 Effects of the dynamical time variations of the background jet on particle acceleration

In this work we have neglected the betatron effect (see e.g., Kowal et al., 2012; de Gouveia Dal Pino and Kowal, 2015), potential effects of the dynamical variations in the background plasma on the acceleration of the particles. When performing the test particle in an MHD background system, in order to follow the particles' interactions with it, we had to transform the background code units to physical units. As we have normalized the particles time unit in hours, this means that, for instance, from the background snapshot  $t = 40 L/c$  to  $t = 50 L/c$ , 10 hours have elapsed. Now, we have seen that particles interact resonantly with the magnetic background fluctuations (according to eq. 2.26) when their Larmor radii are comparable to the wavelength of these fluctuations. When the turbulence in the jet attains a nearly steady-state regime (beyond  $t = 40 L/c$  in the jet), the background dynamical variations become statistically negligible. In other words, the particles will face a very similar background spectrum of fluctuations in the recon-

nection regions spread over the distorted magnetic field spine and outside them, in every snapshot of this nearly stationary regime. This is consistent with the results we obtain for the particle acceleration properties for the evolved snapshots  $t = 46$  and  $50 L/c$ , which are very similar (see Figures 3.11 and 3.18). Earlier studies of the betatron effect, performing test particle simulations considering the background dynamical variations among the snapshots have shown that, in the case of pure turbulent environments (i.e., where the reconnection acceleration favors more a 2nd-order Fermi than a 1st-order, and thus this effect is more important), it introduces only a factor 2 difference in the acceleration rate (e.g. Kowal et al., 2012; de Gouveia Dal Pino and Kowal, 2015, and references therein). Since particles attain energies that are more than 8 orders of magnitude larger than the energy at injection, this effect is almost negligible. It may have some impact (of a factor 2) only at the beginning of the acceleration when particles are still growing their energy linearly, essentially by drift acceleration.

We have plans to perform studies of the particle back-reaction in the CDK unstable jet by incorporating particles directly into the relativistic MHD code. This will allow both, to compute the particle losses in the fluid and perform a more accurate estimation of the betatron effect. With regard to the earlier snapshots ( $t = 25, 30$  and  $40 L/c$ ), when the CDKI and the turbulence are still growing, and the system has not achieved the stationary state yet, one may argue that the background dynamical effects might have implications on the stochastic reconnection acceleration evolution in these cases. However, at  $t = 25 L/c$ , the system has no fast reconnection current sheets yet, and the particles experience only magnetic curvature drift acceleration, as discussed in Section 3.2.2. Of course, this ideal situation may not sustain for long in the real jet since the CDKI grows fast, but it illustrates what may happen with particles in the early transient stages of the growth of the instability and also serves to compare with other (PIC) works (e.g. Alves et al., 2018, see Chapter 4). The snapshot  $30 L/c$ , on the other hand, has already a few fast reconnection sites and, as discussed in Section 3.2.2, it combines the two processes of acceleration. The inclusion of dynamical effects of the background, in this case, would not affect much the results since again we note that the results for particle acceleration are very similar to the more evolved snapshots (see Figures 3.15 and 3.18). Finally, with regard to  $t = 40 L/c$ , this snapshot which is just before the CDK turbulence reaches the nearly steady-state regime, we see that though the exponential growth of the particles kinetic energy is similar to the evolved nearly stationary snapshots, the number of particles that achieve the maximum energy is much smaller (Figure 3.11, top right), which may be reflecting the (minor) effects of neglecting the plasma background evolution in this case.

Other interesting implications arise from the conversion of the simulations into physical units. The results from Figures 3.11, 3.16, 3.18, 3.22 and 3.23 imply a total acceleration

time (including the exponential acceleration regime by reconnection plus the slower final drift acceleration) of a few  $\sim 1000$  hr. During this time, particles have re-entered the system across the periodic boundaries in the longitudinal direction ( $z$ ) several times, traveling a total length of the order of  $\sim 10^{-1}$  pc along the jet. More precise calculations of the total acceleration time in the evolved snapshots directly from the simulations, result at most 7000 hr and, since particles do not travel exactly at the light speed, the resulting total length scales still correspond to sub-pc length scales (at most of  $\sim 10^{-1}$  pc). If we consider only the time elapsed during the acceleration exponential regime, the length scales are even smaller ( $\sim 10^{-2}$  pc). These physical length scales characterize the size of the turbulent induced reconnection dissipation region in a real jet where particles are accelerated. Within these (time and length) scales, the physical conditions in a real system are not expected to change substantially, except for the dissipation of the magnetic energy. It is interesting to note that these scales are also compatible with estimates of the size of the reconnection dissipation layer considered in recent blazar jet studies (see e.g. Christie et al., 2019; Giannios and Uzdensky, 2019). For instance, (Christie et al., 2019) consider a reconnection dissipation slab with  $10^{17}$  cm. (Giannios and Uzdensky, 2019) consider reconnection slabs of  $10^3 R_g$ , where  $R_g$  is the gravitational radius, which for black holes of  $10^8 - 10^9 M_\odot$  give  $10^{16}$  cm - to  $10^{17}$  cm. These values are all compatible with our results.

# Chapter 4

## Conclusions and Prospects for Future Work

In this thesis we have investigated the acceleration of particles injected in several snapshots of a 3D Poynting flux dominated jet with moderate magnetization ( $\sigma \sim 1$ ), subject to current driven kink instability (CDKI) which drives turbulence and fast magnetic reconnection. Motivated by Singh et al. (2016), we have examined the magnetic reconnection rates in such a system employing the algorithm developed in Kadowaki et al. (2018b), which was modified to take into account relativistic effects. Our results can be summarized as follows:

- Once turbulence driven by the CDKI is fully developed in the jet, achieving a nearly steady-state, the amplitude of the excited wiggles along the jet spine also attains a maximum growth and gets disruptive with the formation fast magnetic reconnection in several sites. This occurs after the jet snapshot  $t \sim 40 L/c$ , when the CDKI achieves a plateau. Injecting hundreds to thousands of protons in jet snapshots more evolved than this one, we find that, after about 100 hr, the particles undergo an exponential acceleration up to a maximum energy. For a background magnetic field around  $B \sim 0.1$  G, this saturated kinetic energy is  $\sim 10^7 m_p c^2$ , or  $\sim 10^{10}$  MeV (Figure 3.11), while for a magnetic strength one hundred times larger,  $B \sim 1$  G, the maximum accelerated energy increases also by a factor one hundred, to  $\sim 10^9 m_p c^2$ , or  $\sim 10^{12}$  MeV (Figure 3.23). Beyond these values, the particles suffer further acceleration (to energies up to 100 times larger), but at a much slower rate due to drift in the varying magnetic field.
- Particles achieving the saturation energy in the exponential regime of acceleration attain a Larmor radius comparable to the size of the acceleration region of  $\sim 4L$ , which is of the order of the diameter of the perturbed wiggled jet. This regime of particle acceleration is very similar in all these evolved snapshots and lasts for

several hundred hours until the saturation energy.

- We have quantitatively identified the sites of reconnection over the entire jet (?) and we could correlate them with the accelerated particles (Figures 3.9 and 3.10). The results show a clear association with the regions of maximum current density and fast reconnection sites, indicating that particles are being accelerated by magnetic reconnection, as detected in previous studies (e.g., Kowal et al., 2011, 2012; del Valle et al., 2016). The exponential acceleration in these sites is suggestive of a Fermi stochastic process (e.g., de Gouveia Dal Pino and Lazarian, 2005; de Gouveia Dal Pino and Kowal, 2015; Matthews et al., 2020). Furthermore, during the exponential regime, we have found a predominance of acceleration of the parallel component of the particles velocity to the local magnetic field, which is characteristic of acceleration in reconnection domains.
- In the early stages of the development of the non-linear growth of the CDKI, before this achieves the plateau and the magnetic field lines start disruption, the jet spine oscillates with growing amplitude. We find that during this early stage (jet snapshot  $t = 25 L/c$ ), there are no sites of fast reconnection, but the test particles are efficiently accelerated by magnetic curvature drift, with a dominance of acceleration of the perpendicular component of the particles velocity to the local magnetic field, similarly as detected in the PIC simulations of Alves et al. (2018). However, in order to the particles to get accelerated by this process, they had to be injected with an initial energy much larger than that required for the particles to accelerate in the reconnection sites of the jet, in later snapshots. While in the more evolved snapshots particles can be injected with energies  $10^{-3} m_p c^2$  or less, in this early snapshot they have to be injected at least with  $10 m_p c^2$  to be accelerated (four orders of magnitude larger). This suggests that this mechanism requires pre-accelerated particles in order to work efficiently. This was confirmed by another test where we injected test particles in a later jet snapshot,  $t = 30 L/c$ , where the wiggling amplitude of the magnetic field in the jet spine was still coherent, but a few sites of fast reconnection had already developed and, in such background conditions we find that the particles undergo an efficient acceleration starting with an injection energy of only  $10^{-3} m_p c^2$ . This occurs because in this case, particles are being accelerated from the beginning in the reconnection sites, and then further accelerated in the wiggling spine by curvature drift (Figures 3.13 and 3.15).
- The acceleration time due to magnetic reconnection indicates a weak power law dependence with the particle energy given by  $t_A \propto E^\alpha$ , with  $\alpha \sim 0.1$ , obtained from all test particle models.
- The energy spectrum of the accelerated particles develops a high energy tail that

can be fitted by a power law index  $p \sim -1.2$  in the beginning of the reconnection acceleration, which does not depend on the initial energy of the injected particles, at least in the cases of the acceleration by magnetic reconnection.

- Particles injected in the background jet, assuming periodic conditions in all boundaries, or periodic boundaries only in the  $z$  direction (along the jet axis) and outflow boundaries in the transverse direction, produce similar results. The only remarkable difference is that the adoption of periodic boundaries in all directions allows for particles to re-enter the system more frequently thus increasing the number of accelerated particles.

Our results are comparable to those obtained from test particles injected in single non-relativistic current sheets in which forced turbulence was introduced to make reconnection fast (e.g., Kowal et al., 2011, 2012; del Valle et al., 2016). del Valle et al. (2016), for instance, have obtained an acceleration time with a similar weak energy dependence, with a power law index  $\alpha \sim 0.2 - 0.6$  for a vast range of reconnection velocities. The slightly smaller values of  $\alpha$  we obtained in this work are consistent with the fact that the jet has relativistic Alfvén velocities and thus intrinsically higher reconnection speeds  $V_{rec} \simeq 0.05V_A$  that naturally make the process slightly more efficient. In del Valle et al. (2016), the particle spectrum power-law indices derived in the beginning of the acceleration process, are also compatible with our results. Moreover, our power-law indices are remarkably similar to those obtained from PIC simulations of single current sheets, in the kinetic scales of the plasma (e.g., Zenitani and Hoshino, 2001; Drake et al., 2013; Sironi and Spitkovsky, 2014; Guo et al., 2014, 2015; Li et al., 2015; Werner et al., 2018).

These results are also consistent with the theoretical models of the Fermi acceleration process in reconnection sites (e.g., de Gouveia Dal Pino and Lazarian, 2005; Drury, 2012; de Gouveia Dal Pino and Kowal, 2015), which predict an acceleration time similar to that of stochastic shock acceleration and approximately independent of the reconnection velocity. Similarly as in these earlier studies, particles achieve the maximum energy when their Larmor radius becomes comparable to the size of the acceleration zone.

Other recent studies have also explored numerically acceleration by reconnection in relativistic jets, but considering PIC simulations (e.g., Christie et al., 2019; Nishikawa et al., 2020; Davelaar et al., 2020). Christie et al. (2019) scaled the results of 2D PIC simulations of current sheets with the formation of plasmoids (or magnetic islands) of different sizes to the scales of relativistic jets. Coupling these plasmoid simulations with a radiative transfer code, they reproduced light curves of blazar sources, showing the efficiency of reconnection acceleration to explain multi-scale variability in blazars across the entire electromagnetic spectrum. Nishikawa et al. (2020), on the other hand, performed 3D PIC simulations of a magnetically dominated relativistic jet of electron-proton

pairs, accounting for several mechanisms driving turbulence inside the jet and also found that magnetic reconnection should be the dominant acceleration process. Davelaar et al. (2020) achieved the same conclusion. However, none of these studies involving global jet simulations have derived the properties of the reconnection sites and their correlation with the accelerated particles, as in this work. Moreover, neither of them obtained the general properties of particle acceleration, like the acceleration rate, the size of the acceleration region and the saturation energy achieved by the particles. With regard to the spectrum, Davelaar et al. (2020) obtained a much steeper power-law index than in this work, probably due to the higher magnetization of their jet model, and Nishikawa et al. (2020) study did not obtain any power-law index due to the limited resolution.

It is remarkable that in our work, though we have considered a mild magnetization parameter ( $\sim 1$  in the evolved jet), the results are very consistent even with PIC studies with much higher magnetization (e.g. Comisso and Sironi, 2018, 2019). For instance, the hardness of the power spectrum of the particles in our simulations, in spite of the intrinsic limitations of the test particle method, is similar to these studies. In contrast, as remarked above, Davelaar et al. (2020) obtained much steeper power spectrum (the larger the magnetization parameter the steeper the slope), which they interpreted as due to an inhibition of the acceleration by the strong guide field of the plasma. Comisso and Sironi (2018, 2019), on the other hand, have interpreted their very hard spectrum (which improves with increasing magnetization) as due to the high amplitude of the turbulent fluctuations that are accelerating the particles (though turbulence is decaying in their simulations) and in this way the underlying magnetic field is not sufficient to kill the stochastic process. Therefore, it is possible that one may obtain similar results when considering MHD relativistic jets with higher magnetization, as long as the amplitude of the magnetic fluctuations of the driving turbulence is maintained large enough (i.e.  $\delta B/B \sim 1$ , as e.g. in Comisso and Sironi, 2018, 2019). This obviously requires further investigation since a critical difference of our study and that of Comisso and Sironi (2018, 2019) is the absence in their case of an underlying strong large scale magnetic field, as we have in the jet.

As mentioned before, another recent study also explored particle acceleration in relativistic jets subject to the CDKI by means of 3D PIC simulations of electron-positron pairs (Alves et al., 2018). These authors examined the early non-linear development of this instability and identified an acceleration of the particles due to curvature drift in the wiggling magnetic field structure of growing amplitude along the jet spine. According to their results, a maximum energy growth rate for the electrons  $(\Delta E/\Delta t)/(m_e c^2) \sim 12 c/R$  is achieved at the maximum energy to which the particles are accelerated,  $\sim 125 m_e c^2$ , where  $R$  is the jet radius and the energy is normalized by the electron rest mass energy (see Figure 3(d) in (Alves et al., 2018)). This implies an acceleration time for the electrons,

$t_{acc,e} \simeq 10.4 R/c$ . Considering our test particle model in the earlier jet snapshot where we also identified curvature drift acceleration, i.e.,  $t = 25 L/c$  (model *ut25*), the (Figure 3.18 (bottom diagram) gives for this model a maximum energy growth rate for the protons  $(\Delta E/\Delta t)/(m_p c^2) \sim 10^5 \text{ hr}^{-1}$ , which is achieved at the saturation energy  $\sim 5 \times 10^6 m_p c^2$ . This implies an acceleration time for the protons  $t_{acc,p} \simeq 50 \text{ hr}$ . In order to compare both rates, we need to estimate what would be the acceleration time for the electrons in our simulation. In the relativistic regime, the acceleration time for electrons is approximately given by  $t_{acc,e} \simeq t_{acc,p}(m_e/m_p)$  (e.g., Khiali et al., 2015). Thus, from our results we might expect an electron acceleration time up to the saturation energy due to curvature drift of the order of  $t_{acc,e} \simeq 100 \text{ s}$ , which is comparable to the one obtained in Alves et al. (2018) if one considers a jet radius  $R \sim 10^{-7} \text{ pc}$  in their PIC simulation. However, this is only a rough estimate, since the scales implied in the two simulations are rather distinct. Moreover, in order to improve our estimate for electrons we should perform also numerical simulations for them. However, the numerical integration of the electron trajectories is much longer than for protons in MHD domains and computationally expensive.

The results found in this work have important implications for particle acceleration and the associated non-thermal emission in relativistic jets, specially in their magnetically dominated regions. Though we have not taken into account particle losses, such as non-thermal radiation, electron-positron pair production, particle back reaction into the jet plasma, or particle diffusion, the energies achieved by the particles,  $\sim 10^{16} \text{ eV}$  or  $\sim 10^{18} \text{ eV}$  (and even larger if we take into account the further acceleration by drift up to energy values 100 times larger), depending on the strength of the background magnetic fields  $\sim 0.1 \text{ G}$  or  $\sim 10 \text{ G}$ , are more than sufficient to explain energetic particles and even ultra-high-energy-cosmic-rays (UHECRs) in these sources. Protons with these energies could explain observed very high energy (VHE) emission, as well as the production of neutrinos, out of interactions with the ambient photon and density fields in relativistic jets. This could be the case, for instance, of blazars like TXS 0506+056 (Aartsen et al., 2018), for which for the first time it has been observed simultaneous TeV gamma-rays and neutrino emission. Although there might be other possibilities (see e.g., Cerruti, 2020), this process should be explored in detail elsewhere.

In (?), to probe the robustness of the methods employed here in the investigation of magnetic reconnection in the relativistic jet, we have applied our results to the blazar Mrk 421 (Kushwaha et al., 2017). Building a synthetic light curve from the integrated power of the magnetic reconnection events in the jet, we evaluated the time-variability from a power spectral density analysis, obtaining a good agreement with the observations in the GeV band. This suggests that turbulent fast magnetic reconnection driven by kink instability can be a possible process behind the high energy emission variability phenomena observed in blazars (see details in ?).

## 4.1 Future Prospects

Finally, we should emphasize that *in situ* particle acceleration examined directly in real systems, like the 3D relativistic jets we considered here, is a very promising approach because it allows for testing the process under more realistic environmental conditions, with turbulence and reconnection driven by natural physical processes, and allowing for direct applications to observed systems, and even including time dependence effects. The comparisons with former studies in single current sheets have further validated the process, confirming its ubiquitous nature. The similarity of our results with these earlier works which are based on local (higher resolution) simulations of current sheets (both in PIC and MHD+test particle simulations) have served not only to benchmark and validate our results, but also to highlight the stochastic and universal nature of the process across the scales. Furthermore, this method of injecting particles directly in the collisional MHD simulation of the relativistic jet, have allowed the acceleration of the particles up to the real physical scales where they are accelerated, up to the observed ultra-high-energy (UHE) values, without the need to extrapolate the much smaller energies that are achieved in the kinetic scales, to the large scales, as it is required in PIC simulations.

In forthcoming work we intend to include the radiative losses of the particles by incorporating radiative transfer effects to our jet model and then, apply to observed systems like TXS 0506+056 blazar, for instance. Moreover, since our MHD collisional approach has limitations as only injected particles with Larmor radius close to the MHD scales can be effectively accelerated, and they allow only for modest values of the magnetization parameter, future studies involving hybrid simulations combining PIC and MHD approaches, like those performed for single current sheets (e.g., Bai et al., 2015), should be applied also to real systems, probing both the kinetic and the macroscopic scales of the process, and also accounting for the particles feedback in the system.

# Appendix A

## Godunov Method

For the numerical integration of the SRMHD equations (2.2 to 2.8, Chapter 2), with the RAISHIN code, we employ a Godunov type scheme to solve the Riemann problem at each cell interface. The Riemann problem describes the discontinuity of the fluid between every pair of adjacent cells. The solution of this problem in each cell pair allows to compute numerically the flux ( $\mathbf{F}$ ) of the conserved variables  $\mathbf{U}$  through the cell interface.

Highly accurate Riemann solver, shock-capturing schemes, can be applied to the SRMHD equations. Conservative schemes evolve  $\mathbf{U}$  with equation (2.1) at each time step. These schemes must recover  $\mathbf{P}$  by numerically solving the system of equations. The vector of state  $\mathbf{U}$ , carries the conserved quantities defined in the center of the cells in the domain. For simplicity, we will consider the one-dimensional case, the generalization to three dimensions is straightforward. Therefore equation (2.2) reduces to

$$\frac{\partial U}{\partial t} + \frac{\partial F}{\partial x} = 0 . \quad (\text{A.1})$$

The primitive average variable in a cell " $i$ " is denoted by  $\mathbf{P}_i$ , and its values at the left and right of the grid cell interface, e.g., " $i + 1/2$ " are  $\mathbf{P}_{L,i+1/2}$  and  $\mathbf{P}_{R,i+1/2}$  respectively. The left face, consider the interactions between  $\mathbf{U}_{i-1}$  and  $\mathbf{U}_i$ , while, the right face, the interactions between  $\mathbf{U}_i$  and  $\mathbf{U}_{i+1}$ . From them, we calculate the conserved variables  $\mathbf{U}_R = \mathbf{U}(\mathbf{P}_R)$  and  $\mathbf{U}_L = \mathbf{U}(\mathbf{P}_L)$ , and, the fluxes  $\mathbf{F}_R = \mathbf{F}(\mathbf{U}_R)$  and  $\mathbf{F}_L = \mathbf{F}(\mathbf{U}_L)$ , for a specific cell interface. Around each cell equation (A.1) is

$$\frac{\partial U_i}{\partial t} = \frac{F_{i-1/2} - F_{i+1/2}}{\Delta x} , \quad (\text{A.2})$$

$\Delta x$  is the size of the cell. Integrating in time, with  $t^n$  being the initial time and  $t^{n+1}$  the next step of time,

$$U_i^{n+1} = U_i^n + \frac{\Delta t}{\Delta x} [F_{i-1/2}^n - F_{i+1/2}^n] , \quad (\text{A.3})$$

where  $F_{i\pm 1/2}^n$  are the averaged fluxes in each cell interface. Also we demand that the

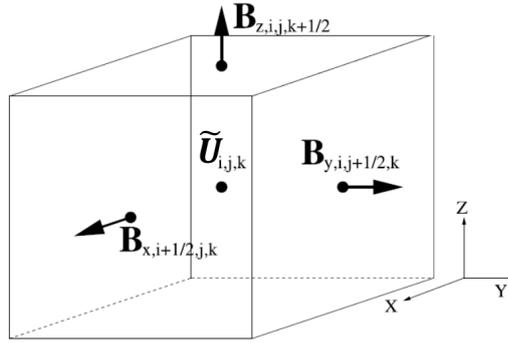


Figure A.1: Schematic representation of a 3D cell, where the volume-averaged conserved variables  $\tilde{\mathbf{U}}$  is in the center of the box, and  $i$ ,  $j$  and  $k$  represent the three directions of the box. The magnetic field  $\mathbf{B}$  is calculated at the edge of the cells.

solution (A.3), be unique. This implies that (e.g. Toro, 1997)

$$S_{max}\Delta t \leq \frac{1}{2}\Delta x, \quad (\text{A.4})$$

where  $S_{max}$  is the maximum velocity of the waves propagating into the cell.

To calculate the fluxes at the interface of the cells we need to interpolate the central flux which is known. We calculated the numerical flux across the cell using the HLLE (Harten, Lax, and van Leer-Einfeldt) approximate Riemann solver Einfeldt (1988), a scheme based on HLL (Harten, Lax, and van Leer Harten et al., 1983). To calculate the HLLE fluxes, one only needs to know a left-going wave speed  $S_L$  and a right-going wave speed  $S_R$  at both sides (right and left) of the grid cell interface, perturbing the initial data states  $U_L$  and  $U_R$ , respectively. Defining  $S_R^+ \equiv \max[0, S_R]$  and  $S_L^- \equiv \min[0, S_L]$ . The HLL flux is given by

$$F_{i+1/2}^{hll} = \frac{S_R^+ F_{L,i+1/2} - S_L^- F_{R,i+1/2} + S_R^+ S_L^- (U_{R,i+1/2} - U_{L,i+1/2})}{S_R^+ + S_L^-}. \quad (\text{A.5})$$

To satisfy the entropy and the positivity conditions, Einfeldt (1988) suggested adequate bounds by making use of the Roe-averaged eigenvalues,  $\lambda_p = (\mathbf{u}, \mathbf{u} + \mathbf{a}, \mathbf{u} - \mathbf{a}, \mathbf{u})$ , where  $\mathbf{u}$  is the fluid velocity and  $\mathbf{a}$  is the speed of sound at the cell interface, and  $p$  varies from 1 to 4. With these consideration

$$S_R = \max[\lambda_2, u_R + a_R], \quad (\text{A.6})$$

and

$$S_L = \min[\lambda_3, u_L - a_L], \quad (\text{A.7})$$

with these wavespeed estimatives (equations A.6 and A.7), the HLL flux (A.5) is also called HLLE one (for more details, see Einfeldt, 1988; Park et al., 2006).

# Appendix B

## Flux-interpolated Constrained Transport Scheme

In a numerical solution the absence of magnetic monopoles is not satisfied because of the numerical errors (due discretization errors and machine precision), and the divergence of the magnetic field is not trivial. In order to maintain divergence-free magnetic fields in the RAISHIN code, it is used flux-interpolated constrained transport (CT) scheme (Tóth, 2000).

The CT places the electric field ( $\Omega = \mathbf{E} = -\mathbf{v} \times \mathbf{B}$ ) at the cell corners and the magnetic field components on cell interface. The induction equation in 2D is discretized by

$$B_{i+1/2,j}^{x,n+1} = B_{i+1/2,j}^{x,n} - \Delta t \frac{\Omega_{i+1/2,j+1/2} - \Omega_{i+1/2,j-1/2}}{\Delta y}, \quad (\text{B.1})$$

$$B_{i,j+1/2}^{y,n+1} = B_{i,j+1/2}^{y,n} - \Delta t \frac{\Omega_{i+1/2,j+1/2} - \Omega_{i-1/2,j+1/2}}{\Delta x}, \quad (\text{B.2})$$

where the indices  $x$  and  $y$  represent the component of the magnetic field. Then,  $\nabla \cdot B^{n+1} = 0$  if  $\nabla \cdot B^n = 0$  where,

$$(\nabla \cdot B)_{i,j} = \frac{B_{i+1/2,j}^x - B_{i-1/2,j}^x}{\Delta x} + \frac{B_{i,j+1/2}^y - B_{i,j-1/2}^y}{\Delta y} \quad (\text{B.3})$$

The flux-interpolated CT scheme interpolates the cell-interface centered fluxes into the electric field at the cell corners (see Figure B.1),

$$\Omega_{i+1/2,j+1/2} = \frac{1}{4}(-F_{i+1/2,j}^x - F_{i+1/2,j+1}^x + F_{i,j+1/2}^y + F_{i+1,j+1/2}^y) \quad (\text{B.4})$$

This electric field can be used to calculate B.3. This scheme conserves  $\nabla \cdot B = 0$  at each grid cell. For more details see Toro (1997), Tóth (2000) and Bodenheimer et al. (2006).

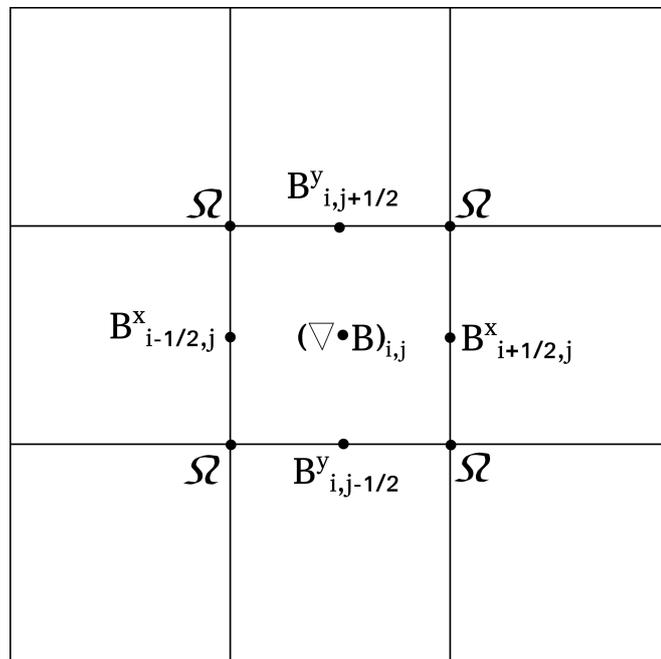


Figure B.1: Sketch sample of a 2D grid centered at the cell position  $(i,j)$ . The electric field  $\Omega$  is located at the cell corners with the purpose to calculate  $\nabla \cdot B$  at the center of the cell.

# Bibliography

Aartsen, M., Ackermann, M., Adams, J., Aguilar, J. A., Ahlers, M., and Ahrens (2018). Neutrino emission from the direction of the blazar txs 0506+056 prior to the icecube-170922a alert. *Science*, 361(6398):147–151.

Abramowicz, M. A. and Fragile, P. C. (2013). Foundations of Black Hole Accretion Disk Theory. *Living Reviews in Relativity*, 16(1):1.

Ackermann, M., Anantua, R., Asano, K., Baldini, L., Barbiellini, G., Bastieri, D., Becerra Gonzalez, J., Bellazzini, R., Bissaldi, E., Blandford, R. D., Bloom, E. D., Bonino, R., Bottacini, E., Bruel, P., Buehler, R., Caliandro, G. A., Cameron, R. A., Caragiulo, M., Caraveo, P. A., Cavazzuti, E., Cecchi, C., Cheung, C. C., Chiang, J., Chiaro, G., Ciprini, S., Cohen-Tanugi, J., Costanza, F., Cutini, S., D’Ammando, F., de Palma, F., Desiante, R., Digel, S. W., Di Lalla, N., Di Mauro, M., Di Venere, L., Drell, P. S., Favuzzi, C., Fegan, S. J., Ferrara, E. C., Fukazawa, Y., Funk, S., Fusco, P., Gargano, F., Gasparrini, D., Giglietto, N., Giordano, F., Giroletti, M., Grenier, I. A., Guillemot, L., Guiriec, S., Hayashida, M., Hays, E., Horan, D., Jóhannesson, G., Kensei, S., Kocevski, D., Kuss, M., La Mura, G., Larsson, S., Latronico, L., Li, J., Longo, F., Loparco, F., Lott, B., Lovellette, M. N., Lubrano, P., Madejski, G. M., Magill, J. D., Maldera, S., Manfreda, A., Mayer, M., Mazziotta, M. N., Michelson, P. F., Mirabal, N., Mizuno, T., Monzani, M. E., Morselli, A., Moskalenko, I. V., Nalewajko, K., Negro, M., Nuss, E., Ohsugi, T., Orlando, E., Paneque, D., Perkins, J. S., Pesce-Rollins, M., Piron, F., Pivato, G., Porter, T. A., Principe, G., Rando, R., Razzano, M., Razzaque, S., Reimer, A., Scargle, J. D., Sgrò, C., Sikora, M., Simone, D., Siskind, E. J., Spada, F., Spinelli, P., Stawarz, L., Thayer, J. B., Thompson, D. J., Torres, D. F., Troja, E., Uchiyama, Y., Yuan, Y., and Zimmer, S. (2016). Minute-timescale  $>100$  MeV  $\gamma$ -Ray Variability during the Giant Outburst of Quasar 3C 279 Observed by Fermi-LAT in 2015 June. *ApJL*, 824(2):L20.

Aharonian, F., Akhperjanian, A. G., Bazer-Bachi, A. R., Behera, B., Beilicke, M., Benbow, W., Berge, D., Bernlöhr, K., Boisson, C., Bolz, O., Borrel, V., Boutelier, T., Braun, I., Brion, E., Brown, A. M., Bühler, R., Büsching, I., Bulik, T., Carrigan, S., Chadwick, P. M., Clapson, A. C., Chounet, L. M., Coignet, G., Cornils, R., Costa-

- mante, L., Degrange, B., Dickinson, H. J., Djannati-Ataï, A., Domainko, W., Drury, L. O., Dubus, G., Dyks, J., Egberts, K., Emmanoulopoulos, D., Espigat, P., Farnier, C., Feinstein, F., Fiasson, A., Förster, A., Fontaine, G., Funk, S., Funk, S., Füßling, M., Gallant, Y. A., Giebels, B., Glicenstein, J. F., Glück, B., Goret, P., Hadjichristidis, C., Hauser, D., Hauser, M., Heinzlmann, G., Henri, G., Hermann, G., Hinton, J. A., Hoffmann, A., Hofmann, W., Holleran, M., Hoppe, S., Horns, D., Jacholkowska, A., de Jager, O. C., Kendziorra, E., Kerschhaggl, M., Khélifi, B., Komin, N., Kosack, K., Lamanna, G., Latham, I. J., Le Gallou, R., Lemièrre, A., Lemoine-Goumard, M., Lenain, J. P., Lohse, T., Martin, J. M., Martineau-Huynh, O., Marcowith, A., Masterson, C., Maurin, G., McComb, T. J. L., Moderski, R., Moulin, E., de Naurois, M., Nedbal, D., Nolan, S. J., Olive, J. P., Orford, K. J., Osborne, J. L., Ostrowski, M., Panter, M., Pedalletti, G., Pelletier, G., Petrucci, P. O., Pita, S., Pühlhofer, G., Punch, M., Ranchon, S., Raubenheimer, B. C., Raue, M., Rayner, S. M., Renaud, M., Ripken, J., Rob, L., Rolland, L., Rosier-Lees, S., Rowell, G., Rudak, B., Ruppel, J., Sahakian, V., Santangelo, A., Saugé, L., Schlenker, S., Schlickeiser, R., Schröder, R., Schwanke, U., Schwarzburg, S., Schwemmer, S., Shalchi, A., Sol, H., Spangler, D., Stawarz, Ł., Steenkamp, R., Stegmann, C., Superina, G., Tam, P. H., Tavernet, J. P., Terrier, R., van Eldik, C., Vasileiadis, G., Venter, C., Vialle, J. P., Vincent, P., Vivier, M., Völk, H. J., Volpe, F., Wagner, S. J., Ward, M., and Zdziarski, A. A. (2007). An Exceptional Very High Energy Gamma-Ray Flare of PKS 2155-304. *ApJL*, 664(2):L71–L74.
- Albert, J., Aliu, E., Anderhub, H., Antoranz, P., and et al. (2007). Very High Energy Gamma-Ray Radiation from the Stellar Mass Black Hole Binary Cygnus X-1. *ApJL*, 665:L51–L54.
- Alves, E. P., Zrake, J., and Fiuza, F. (2018). Efficient Nonthermal Particle Acceleration by the Kink Instability in Relativistic Jets. *PhRvL*, 121(24):245101.
- Antonucci, R. (1993). Unified models for active galactic nuclei and quasars. *ARA&A*, 31:473–521.
- Bai, X.-N., Caprioli, D., Sironi, L., and Spitkovsky, A. (2015). Magnetohydrodynamic-particle-in-cell Method for Coupling Cosmic Rays with a Thermal Plasma: Application to Non-relativistic Shocks. *ApJ*, 809(1):55.
- Barniol Duran, R., Tchekhovskoy, A., and Giannios, D. (2017). Simulations of AGN jets: magnetic kink instability versus conical shocks. *MNRAS*, 469(4):4957–4978.
- Bateman, G. (1978). *MHD instabilities*.
- Beckmann, V. and Shrader, C. (2012). The AGN phenomenon: open issues. In *Proceedings of “An INTEGRAL view of the high-energy sky (the first 10 years)” - 9th INTEGRAL*

- Workshop and celebration of the 10th anniversary of the launch (INTEGRAL 2012). 15-19 October 2012. Bibliotheque Nationale de France, page 69.*
- Begelman, M. C. (1998). Instability of Toroidal Magnetic Field in Jets and Plerions. *ApJ*, 493(1):291–300.
- Begelman, M. C., Fabian, A. C., and Rees, M. J. (2008). Implications of very rapid TeV variability in blazars. *MNRAS*, 384(1):L19–L23.
- Bell, A. R. (1978). The acceleration of cosmic rays in shock fronts - I. *MNRAS*, 182:147–156.
- Bell, A. R., Araudo, A. T., Matthews, J. H., and Blundell, K. M. (2018). Cosmic-ray acceleration by relativistic shocks: limits and estimates. *MNRAS*, 473(2):2364–2371.
- Bellan, P. M., You, S., and Hsu, S. C. (2005). *Simulating Astrophysical Jets in Laboratory Experiments*, page 203.
- Beresnyak, A. and Li, H. (2016). First-Order Particle Acceleration in Magnetically-driven Flows. *ApJ*, 819(2):90.
- Bittencourt, J. A. (2004). *Fundamentals of Plasma Physics*. Fundamentals of Plasma Physics, Third Edition by J.A. Bittencourt. Published by Springer-Verlag, New York, Inc.; 2004. ISBN 0-387-20975-1., third edition.
- Blandford, R. and Eichler, D. (1987). Particle acceleration at astrophysical shocks: A theory of cosmic ray origin. *PhR*, 154(1):1–75.
- Blandford, R., Meier, D., and Readhead, A. (2019). Relativistic Jets from Active Galactic Nuclei. *ARA&A*, 57:467–509.
- Blandford, R. D. and Payne, D. G. (1982). Hydromagnetic flows from accretion discs and the production of radio jets. *MNRAS*, 199:883–903.
- Blandford, R. D. and Znajek, R. L. (1977). Electromagnetic extraction of energy from Kerr black holes. *MNRAS*, 179:433–456.
- Boccardi, B., Krichbaum, T., Bach, U., Ros, E., and Zensus, J. A. (2015). High resolution mm-VLBI imaging of Cygnus A. *arXiv e-prints*, page arXiv:1504.01272.
- Bodenheimer, P., Laughlin, G., Rozyczka, M., Plewa, T., Yorke, H., and Yorke, H. (2006). *Numerical Methods in Astrophysics: An Introduction*. Series in Astronomy and Astrophysics. Taylor & Francis.
- Braithwaite, J. (2006). The stability of toroidal fields in stars. *A&A*, 453:687–698.

- Britto, R. J., Bottacini, E., Lott, B., Razzaque, S., and Buson, S. (2016). Fermi-LAT Observations of the 2014 May-July Outburst from 3C 454.3. *ApJ*, 830(2):162.
- Bromberg, O., Singh, C. B., Davelaar, J., and Philippov, A. A. (2019). Kink Instability: Evolution and Energy Dissipation in Relativistic Force-free Nonrotating Jets. *ApJ*, 884(1):39.
- Bromberg, O. and Tchekhovskoy, A. (2016). Relativistic MHD simulations of core-collapse GRB jets: 3D instabilities and magnetic dissipation. *MNRAS*, 456(2):1739–1760.
- Brunetti, G. and Lazarian, A. (2011). Acceleration of primary and secondary particles in galaxy clusters by compressible MHD turbulence: from radio haloes to gamma-rays. *MNRAS*, 410(1):127–142.
- Brunetti, G. and Vazza, F. (2020). Second-order Fermi Reacceleration Mechanisms and Large-Scale Synchrotron Radio Emission in Intracluster Bridges. *PhRvL*, 124(5):051101.
- Büchner, J., Dum, C., and Scholer, M. (2003). *Space Plasma Simulation*, volume 615.
- Cabral, B. and Leedom, L. C. (1993). Imaging vector fields using line integral convolution. In *Proceedings of the 20th Annual Conference on Computer Graphics and Interactive Techniques*, SIGGRAPH '93, pages 263–270, New York, NY, USA. Association for Computing Machinery.
- Cerruti, M. (2020). Neutrinos from blazars. In *Journal of Physics Conference Series*, volume 1468 of *Journal of Physics Conference Series*, page 012094.
- Cerutti, B., Uzdensky, D. A., and Begelman, M. C. (2012). Extreme Particle Acceleration in Magnetic Reconnection Layers: Application to the Gamma-Ray Flares in the Crab Nebula. *ApJ*, 746(2):148.
- Cerutti, B., Werner, G. R., Uzdensky, D. A., and Begelman, M. C. (2014). Gamma-ray flares in the Crab Nebula: A case of relativistic reconnection? a). *Physics of Plasmas*, 21(5):056501.
- Christie, I. M., Petropoulou, M., Sironi, L., and Giannios, D. (2019). Radiative signatures of plasmoid-dominated reconnection in blazar jets. *MNRAS*, 482(1):65–82.
- Clausen-Brown, E. and Lyutikov, M. (2012). Crab nebula gamma-ray flares as relativistic reconnection minijets. *MNRAS*, 426(2):1374–1384.
- Comisso, L. and Sironi, L. (2018). Particle Acceleration in Relativistic Plasma Turbulence. *PhRvL*, 121(25):255101.

- Comisso, L. and Sironi, L. (2019). The Interplay of Magnetically Dominated Turbulence and Magnetic Reconnection in Producing Nonthermal Particles. *ApJ*, 886(2):122.
- Das, T. K. (1999). Modelling the Origin of Astrophysical Jets from Galactic and Extragalactic Sources. *arXiv e-prints*, pages astro-ph/9906113.
- Das, U. and Begelman, M. C. (2019). Internal instabilities in magnetized jets. *MNRAS*, 482(2):2107–2131.
- Davelaar, J., Philippov, A. A., Bromberg, O., and Singh, C. B. (2020). Particle Acceleration in Kink-unstable Jets. *ApJL*, 896(2):L31.
- de Gouveia Dal Pino, E., Batista, R. A., Kadowaki, L. H. S., Kowal, G., Medina-Torrejón, T. E., and Ramirez-Rodriguez, J. C. (2018). Magnetic reconnection, Cosmic Ray Acceleration and Gamma-Ray emission around Black Holes and Relativistic Jets. In *International Conference on Black Holes as Cosmic Batteries: UHECRs and Multimessenger Astronomy. 12-15 September 2018. Foz do Iguacu*, page 8.
- de Gouveia Dal Pino, E. M. (2005). Astrophysical jets and outflows. *Advances in Space Research*, 35(5):908–924.
- de Gouveia Dal Pino, E. M. and Kowal, G. (2015). *Particle Acceleration by Magnetic Reconnection*, volume 407 of *Astrophysics and Space Science Library*, page 373. Springer Berlin Heidelberg.
- de Gouveia Dal Pino, E. M., Kowal, G., Kadowaki, L., Medina-Torrejón, T. E., Mizuno, Y., and Singh, C. (2020). Particle acceleration and the origin of the very high energy emission around black holes and relativistic jets. In Asada, K., de Gouveia Dal Pino, E., Giroletti, M., Nagai, H., and Nemmen, R., editors, *IAU Symposium*, volume 342 of *IAU Symposium*, pages 13–18.
- de Gouveia Dal Pino, E. M., Kowal, G., Kadowaki, L. H. S., Piovezan, P., and Lazarian, A. (2010a). Magnetic Field Effects Near the Launching Region of Astrophysical Jets. *International Journal of Modern Physics D*, 19(6):729–739.
- de Gouveia Dal Pino, E. M. and Lazarian, A. (2005). Production of the large scale superluminal ejections of the microquasar GRS 1915+105 by violent magnetic reconnection. *A&A*, 441(3):845–853.
- de Gouveia Dal Pino, E. M., Piovezan, P. P., and Kadowaki, L. H. S. (2010b). The role of magnetic reconnection on jet/accretion disk systems. *A&A*, 518:A5.
- del Valle, M. V., de Gouveia Dal Pino, E. M., and Kowal, G. (2016). Properties of the first-order Fermi acceleration in fast magnetic reconnection driven by turbulence in collisional magnetohydrodynamical flows. *MNRAS*, 463:4331–4343.

- Del Zanna, L., Zanotti, O., Bucciantini, N., and Londrillo, P. (2007). ECHO: a Eulerian conservative high-order scheme for general relativistic magnetohydrodynamics and magnetodynamics. *A&A*, 473(1):11–30.
- Doeleman, S. S., Fish, V. L., Schenck, D. E., Beaudoin, C., Blundell, R., Bower, G. C., Broderick, A. E., Chamberlin, R., Freund, R., Friberg, P., Gurwell, M. A., Ho, P. T. P., Honma, M., Inoue, M., Krichbaum, T. P., Lamb, J., Loeb, A., Lonsdale, C., Marrone, D. P., Moran, J. M., Oyama, T., Plambeck, R., Primiani, R. A., Rogers, A. E. E., Smythe, D. L., SooHoo, J., Strittmatter, P., Tilanus, R. P. J., Titus, M., Weintroub, J., Wright, M., Young, K. H., and Ziurys, L. M. (2012). Jet-Launching Structure Resolved Near the Supermassive Black Hole in M87. *Science*, 338(6105):355.
- Drake, J. F., Opher, M., Swisdak, M., and Chamoun, J. N. (2010). A Magnetic Reconnection Mechanism for the Generation of Anomalous Cosmic Rays. *ApJ*, 709(2):963–974.
- Drake, J. F., Swisdak, M., Che, H., and Shay, M. A. (2006). Electron acceleration from contracting magnetic islands during reconnection. *Nature*, 443(7111):553–556.
- Drake, J. F., Swisdak, M., and Fermo, R. (2013). The Power-law Spectra of Energetic Particles during Multi-island Magnetic Reconnection. *ApJL*, 763(1):L5.
- Drenkhahn, G. and Spruit, H. C. (2002). Efficient acceleration and radiation in Poynting flux powered GRB outflows. *A&A*, 391:1141–1153.
- Drury, L. O. (2012). First-order Fermi acceleration driven by magnetic reconnection. *MNRAS*, 422(3):2474–2476.
- Einfeldt, B. (1988). On Godunov-Type Methods for Gas Dynamics. *SIAM Journal on Numerical Analysis*, 25(2):294–318.
- Eyink, G. L., Lazarian, A., and Vishniac, E. T. (2011). Fast Magnetic Reconnection and Spontaneous Stochasticity. *ApJ*, 743(1):51.
- Fowler, T. K., Li, H., and Anantua, R. (2019). A Quasi-static Hyper-resistive Model of Ultra-high-energy Cosmic-ray Acceleration by Magnetically Collimated Jets Created by Active Galactic Nuclei. *ApJ*, 885(1):4.
- Furth, H. P., Killeen, J., and Rosenbluth, M. N. (1963). Finite-resistivity instabilities of a sheet pinch. *The Physics of Fluids*, 6(4):459–484.
- Giannios, D. (2008). Prompt GRB emission from gradual energy dissipation. *A&A*, 480(2):305–312.
- Giannios, D. (2010). UHECRs from magnetic reconnection in relativistic jets. *MNRAS*, 408(1):L46–L50.

- Giannios, D. (2013). Reconnection-driven plasmoids in blazars: fast flares on a slow envelope. *MNRAS*, 431(1):355–363.
- Giannios, D. and Spruit, H. C. (2006). The role of kink instability in Poynting-flux dominated jets. *A&A*, 450(3):887–898.
- Giannios, D. and Spruit, H. C. (2007). Spectral and timing properties of a dissipative  $\gamma$ -ray burst photosphere. *A&A*, 469(1):1–9.
- Giannios, D. and Uzdensky, D. A. (2019). GRB and blazar jets shining through their stripes. *MNRAS*, 484(1):1378–1389.
- Giannios, D., Uzdensky, D. A., and Begelman, M. C. (2009). Fast TeV variability in blazars: jets in a jet. *MNRAS*, 395(1):L29–L33.
- Gill, R., Granot, J., and Lyubarsky, Y. (2018). 2D Relativistic MHD simulations of the Kruskal-Schwarzschild instability in a relativistic striped wind. *MNRAS*, 474(3):3535–3546.
- Giroletti, M., Giovannini, G., Feretti, L., Cotton, W. D., Edwards, P. G., Lara, L., Marscher, A. P., Mattox, J. R., Piner, B. G., and Venturi, T. (2004). Parsec-Scale Properties of Markarian 501. *ApJ*, 600(1):127–140.
- Guan, X., Li, H., and Li, S. (2014). Relativistic MHD Simulations of Poynting Flux-driven Jets. *ApJ*, 781(1):48.
- Guo, F., Li, H., Daughton, W., Li, X., and Liu, Y.-H. (2016). Particle acceleration during magnetic reconnection in a low-beta pair plasma. *Physics of Plasmas*, 23(5):055708.
- Guo, F., Li, H., Daughton, W., and Liu, Y.-H. (2014). Formation of Hard Power Laws in the Energetic Particle Spectra Resulting from Relativistic Magnetic Reconnection. *PhRvL*, 113(15):155005.
- Guo, F., Liu, Y.-H., Daughton, W., and Li, H. (2015). Particle Acceleration and Plasma Dynamics during Magnetic Reconnection in the Magnetically Dominated Regime. *ApJ*, 806(2):167.
- Hardee, P., Mizuno, Y., and Nishikawa, K.-I. (2007). GRMHD/RMHD simulations & stability of magnetized spine-sheath relativistic jets. *Ap&SS*, 311(1-3):281–286.
- Hardee, P. E. (2004). The Stability Properties of Astrophysical Jets. *Ap&SS*, 293(1):117–129.
- Harris, D. E., Biretta, J. A., Junor, W., Perlman, E. S., Sparks, W. B., and Wilson, A. S. (2003). Flaring X-Ray Emission from HST-1, a Knot in the M87 Jet. *ApJL*, 586(1):L41–L44.

- Harten, A., Lax, P. D., and Leer, B. (1983). On Upstream Differencing and Godunov-Type Schemes for Hyperbolic Conservation Laws. *SIAM Rev.*, 25:35–61.
- Hovatta, T. and Lindfors, E. (2019). Relativistic Jets of Blazars. *NewAR*, 87:101541.
- Hsu, S. C. and Bellan, P. M. (2002). A laboratory plasma experiment for studying magnetic dynamics of accretion discs and jets. *MNRAS*, 334:257–261.
- Istomin, Y. N. and Pariev, V. I. (1994). Stability of a relativistic rotating electron-positron jet. *MNRAS*, 267:629–636.
- Jorstad, S. G., Marscher, A. P., Morozova, D. A., Troitsky, I. S., Agudo, I., Casadio, C., Foord, A., Gómez, J. L., MacDonald, N. R., Molina, S. N., Lähteenmäki, A., Tammi, J., and Tornikoski, M. (2017). Kinematics of Parsec-scale Jets of Gamma-Ray Blazars at 43 GHz within the VLBA-BU-BLAZAR Program. *ApJ*, 846(2):98.
- Kadowaki, L. H. S., de Gouveia Dal Pino, E., and Medina-Torrejón, T. E. (2018a). A statistical study of fast magnetic reconnection in turbulent accretion disks and jets. In *International Conference on Black Holes as Cosmic Batteries: UHECRs and Multimessenger Astronomy. 12-15 September 2018. Foz do Iguaçu*, page 16.
- Kadowaki, L. H. S., de Gouveia Dal Pino, E. M., Medina Torrejón, T. E., Mizuno, Y., and Kushwaha, P. (2021). Fast magnetic reconnection structures in Poynting-flux dominated jets. *in press*, page arXiv:2011.03634.
- Kadowaki, L. H. S., de Gouveia Dal Pino, E. M., and Singh, C. B. (2015). The Role of Fast Magnetic Reconnection on the Radio and Gamma-ray Emission from the Nuclear Regions of Microquasars and Low Luminosity AGNs. *ApJ*, 802:113.
- Kadowaki, L. H. S., de Gouveia Dal Pino, E. M., and Stone, J. M. (2018b). MHD Instabilities in Accretion Disks and Their Implications in Driving Fast Magnetic Reconnection. *ApJ*, 864(1):52.
- Kellermann, K. I., Kovalev, Y. Y., Lister, M. L., Homan, D. C., Kadler, M., Cohen, M. H., Ros, E., Zensus, J. A., Vermeulen, R. C., Aller, M. F., and Aller, H. D. (2007). Doppler boosting, superluminal motion, and the kinematics of AGN jets. *Ap&SS*, 311(1-3):231–239.
- Khiali, B., de Gouveia Dal Pino, E. M., and del Valle, M. V. (2015). A magnetic reconnection model for explaining the multiwavelength emission of the microquasars Cyg X-1 and Cyg X-3. *MNRAS*, 449:34–48.
- Komissarov, S. S. (1999). A Godunov-type scheme for relativistic magnetohydrodynamics. *MNRAS*, 303:343–366.

- Kovalev, Y. Y., Lister, M. L., Homan, D. C., and Kellermann, K. I. (2007). The Inner Jet of the Radio Galaxy M87. *ApJL*, 668(1):L27–L30.
- Kowal, G., de Gouveia Dal Pino, E. M., and Lazarian, A. (2011). Magnetohydrodynamic Simulations of Reconnection and Particle Acceleration: Three-dimensional Effects. *ApJ*, 735(2):102.
- Kowal, G., de Gouveia Dal Pino, E. M., and Lazarian, A. (2012). Particle Acceleration in Turbulence and Weakly Stochastic Reconnection. *PhRvL*, 108(24):241102.
- Kowal, G., Lazarian, A., Vishniac, E. T., and Otmianowska-Mazur, K. (2009). *Numerical Tests of Fast Reconnection in Weakly Stochastic Magnetic Fields*. *ApJ*, 700:63.
- Kushwaha, P., Sinha, A., Misra, R., Singh, K. P., and de Gouveia Dal Pino, E. M. (2017). Gamma-Ray Flux Distribution and Nonlinear Behavior of Four LAT Bright AGNs. *ApJ*, 849(2):138.
- Laurent, P., Rodriguez, J., Wilms, J., Cadolle Bel, M., Pottschmidt, K., and Grinberg, V. (2011). Polarized Gamma-Ray Emission from the Galactic Black Hole Cygnus X-1. *Science*, 332(6028):438.
- Lazarian, A., Eyink, G. L., Jafari, A., Kowal, G., Li, H., Xu, S., and Vishniac, E. T. (2020). 3D turbulent reconnection: Theory, tests, and astrophysical implications. *Physics of Plasmas*, 27(1):012305.
- Lazarian, A. and Vishniac, E. T. (1999). Reconnection in a Weakly Stochastic Field. *ApJ*, 517:700–718.
- Lazarian, A., Vlahos, L., Kowal, G., Yan, H., Beresnyak, A., and de Gouveia Dal Pino, E. M. (2012). Turbulence, Magnetic Reconnection in Turbulent Fluids and Energetic Particle Acceleration. *Space Sci. Rev.*, 173(1-4):557–622.
- Li, X., Guo, F., Li, H., and Li, G. (2015). Nonthermally Dominated Electron Acceleration during Magnetic Reconnection in a Low- $\beta$  Plasma. *ApJL*, 811(2):L24.
- Lobanov, A. P. and Zensus, J. A. (2001). A Cosmic Double Helix in the Archetypical Quasar 3C273. *Science*, 294(5540):128–131.
- Lyubarskii, Y. E. (1999). Kink instability of relativistic force-free jets. *MNRAS*, 308:1006–1010.
- Lyubarsky, Y. and Kirk, J. G. (2001). Reconnection in a Striped Pulsar Wind. *ApJ*, 547(1):437–448.

- Lyubarsky, Y. and Liverts, M. (2008). Particle Acceleration in the Driven Relativistic Reconnection. *ApJ*, 682(2):1436–1442.
- Lyutikov, M., Sironi, L., Komissarov, S. S., and Porth, O. (2017). Particle acceleration in relativistic magnetic flux-merging events. *Journal of Plasma Physics*, 83(6):635830602.
- Martí-Vidal, I., Muller, S., Vlemmings, W., Horellou, C., and Aalto, S. (2015). A strong magnetic field in the jet base of a supermassive black hole. *Science*, 348(6232):311–314.
- Matthews, J., Bell, A., and Blundell, K. (2020). Particle acceleration in astrophysical jets. *arXiv e-prints*, page arXiv:2003.06587.
- McKinney, J. C. (2006). General relativistic magnetohydrodynamic simulations of the jet formation and large-scale propagation from black hole accretion systems. *MNRAS*, 368(4):1561–1582.
- McKinney, J. C. and Uzdensky, D. A. (2012). A reconnection switch to trigger gamma-ray burst jet dissipation. *MNRAS*, 419(1):573–607.
- Medina-Torrejón, T. E., de Gouveia Dal Pino, E. M., Kadowaki, L. H. S., Kowal, G., Singh, C. B., and Mizuno, Y. (2021). Particle Acceleration by Relativistic Magnetic Reconnection Driven by Kink Instability Turbulence in Poynting Flux-Dominated Jets. *ApJ*, 908(2):193.
- Mizuno, Y., Gómez, J. L., Nishikawa, K.-I., Meli, A., Hardee, P. E., and Rezzolla, L. (2015). Recollimation Shocks in Magnetized Relativistic Jets. *ApJ*, 809(1):38.
- Mizuno, Y., Hardee, P. E., and Nishikawa, K.-I. (2011). Three-dimensional Relativistic Magnetohydrodynamic Simulations of Current-driven Instability with a Sub-Alfvénic Jet: Temporal Properties. *ApJ*, 734(1):19.
- Mizuno, Y., Hardee, P. E., and Nishikawa, K.-I. (2014). Spatial Growth of the Current-driven Instability in Relativistic Jets. *ApJ*, 784(2):167.
- Mizuno, Y., Lyubarsky, Y., Nishikawa, K.-I., and Hardee, P. E. (2009). Three-Dimensional Relativistic Magnetohydrodynamic Simulations of Current-Driven Instability. I. Instability of a Static Column. *ApJ*, 700(1):684–693.
- Mizuno, Y., Lyubarsky, Y., Nishikawa, K.-I., and Hardee, P. E. (2012). Three-dimensional Relativistic Magnetohydrodynamic Simulations of Current-driven Instability. III. Rotating Relativistic Jets. *ApJ*, 757(1):16.
- Mizuno, Y., Nishikawa, K.-I., Koide, S., Hardee, P., and Fishman, G. J. (2006). RAISHIN: A High-Resolution Three-Dimensional General Relativistic Magnetohydrodynamics Code. *arXiv e-prints*, pages astro-ph/0609004.

- Moser, A. L. and Bellan, P. M. (2012). Magnetic reconnection from a multiscale instability cascade. *Nature*, 482:379–381.
- Nagai, H., Haga, T., Giovannini, G., Doi, A., Orienti, M., D’Ammando, F., Kino, M., Nakamura, M., Asada, K., Hada, K., and Giroletti, M. (2014). Limb-brightened Jet of 3C 84 Revealed by the 43 GHz Very-Long-Baseline-Array Observation. *ApJ*, 785(1):53.
- Narayan, R., Li, J., and Tchekhovskoy, A. (2009). Stability of Relativistic Force-free Jets. *ApJ*, 697(2):1681–1694.
- Nathanail, A., Fromm, C. M., Porth, O., Olivares, H., Younsi, Z., Mizuno, Y., and Rezzolla, L. (2020). Plasmoid formation in global GRMHD simulations and AGN flares. *MNRAS*, 495(2):1549–1565.
- Nishikawa, K., Mizuno, Y., Gómez, J. L., Duĝan, I., Niemiec, J., Kobzar, O., MacDonald, N., Meli, A., Pohl, M., and Hirovani, K. (2020). Rapid particle acceleration due to recollimation shocks and turbulent magnetic fields in injected jets with helical magnetic fields. *MNRAS*, 493(2):2652–2658.
- Park, S. H., Lee, J. E., and Kwon, J. H. (2006). Preconditioned HLLE Method for Flows at All Mach Numbers. *AIAA Journal*, 44(11):2645–2653.
- Parker, E. N. (1957). Sweet’s Mechanism for Merging Magnetic Fields in Conducting Fluids. *J. Geophys. Res.*, 62(4):509–520.
- Parnell, C. E., Maclean, R. C., Haynes, A. L., and Galsgaard, K. (2010). 3d magnetic reconnection. *Proceedings of the International Astronomical Union*, 6(S271):227–238.
- Pontin, D. I., Wilmot-Smith, A. L., Hornig, G., and Galsgaard, K. (2011). Dynamics of braided coronal loops. II. Cascade to multiple small-scale reconnection events. *A&A*, 525:A57.
- Porth, O. and Komissarov, S. S. (2015). Causality and stability of cosmic jets. *MNRAS*, 452(2):1089–1104.
- Priest, E. R., Hornig, G., and Pontin, D. I. (2003). On the nature of three-dimensional magnetic reconnection. *Journal of Geophysical Research (Space Physics)*, 108(A7):1285.
- Rodriguez-Ramirez, J. C., de Gouveia Dal Pino, E. M., and Alves Batista, R. (2019). Very-high-energy Emission from Magnetic Reconnection in the Radiative-inefficient Accretion Flow of SgrA\*. *ApJ*, 879(1):6.
- Roth, J. R. (1997). *Ball Lightning*, pages 459–473. Springer US, Boston, MA.

- Rybicki, G. and Lightman, A. (1991). *Radiative Processes in Astrophysics*. A Wiley-Interscience publication. Wiley.
- Sambruna, R. M. (1997). Soft X-Ray Properties of Flat-Spectrum Radio Quasars. *ApJ*, 487(2):536–554.
- Santos-Lima, R., Guerrero, G., de Gouveia Dal Pino, E. M., and Lazarian, A. (2020). Diffusion of large-scale magnetic fields by reconnection in MHD turbulence. *arXiv e-prints*, page arXiv:2005.07775.
- Santos-Lima, R., Lazarian, A., de Gouveia Dal Pino, E. M., and Cho, J. (2010). Diffusion of Magnetic Field and Removal of Magnetic Flux from Clouds Via Turbulent Reconnection. *ApJ*, 714(1):442–461.
- Singh, C. B., de Gouveia Dal Pino, E. M., and Kadowaki, L. H. S. (2015). On the Role of Fast Magnetic Reconnection in Accreting Black Hole Sources. *ApJL*, 799:L20.
- Singh, C. B., Mizuno, Y., and de Gouveia Dal Pino, E. M. (2016). Spatial Growth of Current-driven Instability in Relativistic Rotating Jets and the Search for Magnetic Reconnection. *ApJ*, 824:48.
- Sironi, L., Petropoulou, M., and Giannios, D. (2015). Relativistic jets shine through shocks or magnetic reconnection? *MNRAS*, 450(1):183–191.
- Sironi, L. and Spitkovsky, A. (2014). Relativistic Reconnection: An Efficient Source of Non-thermal Particles. *ApJL*, 783(1):L21.
- Sironi, L., Spitkovsky, A., and Arons, J. (2013). The Maximum Energy of Accelerated Particles in Relativistic Collisionless Shocks. *ApJ*, 771(1):54.
- Spruit, H. C., Daigne, F., and Drenkhahn, G. (2001). Large scale magnetic fields and their dissipation in GRB fireballs. *A&A*, 369:694–705.
- Stenson, E. V., Horn-Stanja, J., Stoneking, M. R., and Pedersen, T. S. (2017). Debye length and plasma skin depth: two length scales of interest in the creation and diagnosis of laboratory pair plasmas. *Journal of Plasma Physics*, 83(1):595830106.
- Striani, E., Mignone, A., Vaidya, B., Bodo, G., and Ferrari, A. (2016). MHD simulations of three-dimensional resistive reconnection in a cylindrical plasma column. *MNRAS*, 462(3):2970–2979.
- Takamoto, M., Inoue, T., and Lazarian, A. (2015). Turbulent Reconnection in Relativistic Plasmas and Effects of Compressibility. *ApJ*, 815(1):16.

- Tchekhovskoy, A. and Bromberg, O. (2016). Three-dimensional relativistic MHD simulations of active galactic nuclei jets: magnetic kink instability and Fanaroff-Riley dichotomy. *MNRAS*, 461(1):L46–L50.
- Tenerani, A., Rappazzo, A. F., Velli, M., and Pucci, F. (2015). The Tearing Mode Instability of Thin Current Sheets: the Transition to Fast Reconnection in the Presence of Viscosity. *ApJ*, 801(2):145.
- Toro, E. F. (1997). *The HLL and HLLC Riemann Solvers*, pages 293–311. Springer Berlin Heidelberg, Berlin, Heidelberg.
- Tóth, G. (2000). The  $\nabla \cdot \mathbf{b} = 0$  constraint in shock-capturing magnetohydrodynamics codes. *Journal of Computational Physics*, 161(2):605–652.
- Tskhakaya, D. (2008). *The Particle-in-Cell Method*, pages 161–189. Springer Berlin Heidelberg, Berlin, Heidelberg.
- Urry, C. M. and Padovani, P. (1995). Unified Schemes for Radio-Loud Active Galactic Nuclei. *Publications of the ASP*, 107:803.
- Werner, G. R., Philippov, A. A., and Uzdensky, D. A. (2019). Particle acceleration in relativistic magnetic reconnection with strong inverse-Compton cooling in pair plasmas. *MNRAS*, 482(1):L60–L64.
- Werner, G. R., Uzdensky, D. A., Begelman, M. C., Cerutti, B., and Nalewajko, K. (2018). Non-thermal particle acceleration in collisionless relativistic electron-proton reconnection. *MNRAS*, 473(4):4840–4861.
- Wilson, A. S. and Colbert, E. J. M. (1995). The Difference between Radio-loud and Radio-quiet Active Galaxies. *ApJ*, 438:62.
- Yamada, M., Kulsrud, R., and Ji, H. (2010). Magnetic reconnection. *Reviews of Modern Physics*, 82:603–664.
- Yamada, M., Yoo, J., and Zenitani, S. (2016). *Energy Conversion and Inventory of a Prototypical Magnetic Reconnection layer*, volume 427, page 143.
- Yuan, F. and Narayan, R. (2014). Hot Accretion Flows Around Black Holes. *ARA&A*, 52:529–588.
- Zenitani, S. and Hoshino, M. (2001). The Generation of Nonthermal Particles in the Relativistic Magnetic Reconnection of Pair Plasmas. *Apjl*, 562:L63–L66.
- Zenitani, S. and Hoshino, M. (2007). Particle Acceleration and Magnetic Dissipation in Relativistic Current Sheet of Pair Plasmas. *ApJ*, 670(1):702–726.

- Zenitani, S. and Hoshino, M. (2008). The Role of the Guide Field in Relativistic Pair Plasma Reconnection. *ApJ*, 677(1):530–544.
- Zhang, B. and Yan, H. (2011). The Internal-collision-induced Magnetic Reconnection and Turbulence (ICMART) Model of Gamma-ray Bursts. *ApJ*, 726:90.
- Zhdankin, V., Uzdensky, D. A., Perez, J. C., and Boldyrev, S. (2013). Statistical Analysis of Current Sheets in Three-dimensional Magnetohydrodynamic Turbulence. *ApJ*, 771(2):124.
- Zweibel, E. G. and Yamada, M. (2009). Magnetic Reconnection in Astrophysical and Laboratory Plasmas. *ARA&A*, 47(1):291–332.